Cardiff University

School of Engineering

A Thesis submitted for the Degree of Doctor of Philosophy

Improved Motion-Correction for MRI with Markerless Face-Tracking

PhD candidate
Elisa Marchetto

Supervisors
Dr. Daniel Gallichan
Prof. Kevin Murphy

Academic year 2022-2023

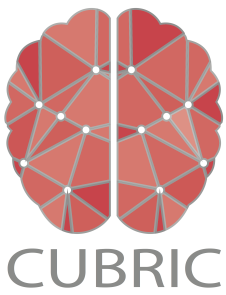

"Why are you sabotaging my research?"

"I am literally you"

Thesis summary

Motion artifacts are a well-known problem in MRI. They can extensively reduce image sharpness and resolution, as well as obscure pathologic conditions, which will make the images not suitable for clinical or research purposes. Over the years, multiple motion correction methods have been proposed to compensate for motion artifacts in different MRI applications. In this thesis, we investigate methods to maximize the image quality of brain MR images at different motion regimes, with the goal of obtaining high-quality images in the case of large and continuous motion profiles as might be expected in some children or patients with movement disorders.

We describe a new autofocusing algorithm to correct for in-plane translations and rotations without any previous information coming from motion tracking sources. Preliminary results show good motion compensation for 2D translations. However, we show how rotations cannot be accurately estimated at the present stage, which should be investigated in future studies. We analyse the extent of the motion parameters estimation accuracy of a navigator-based motion correction method using simulated data. The navigator relies on GRAPPA reconstruction of the highly accelerated navigator fat-volumes to estimate the motion parameters. Our results suggest that the fat-navigator is capable of compensating for large range of motion, as well as for fast and slow changes in the head position. Better correction is expected if GRAPPA weights are updated throughout the entire duration of the scan. The fat-navigator is then compared with another tracking technique based on structured light to track the subject's head movements. We present the results obtained from different motion types as well as a method to improve the motion estimation accuracy of the navigator-based technique in the presence of extensive pitch-wise motion using a skull masking approach.

Finally, we introduce a method to quickly develop and test motion-robust pulse sequences using an open-source framework to acquire MR images producing low acoustic noise levels, which make them suitable for paediatric/infant age group, where research scans are typically conducted while the subject is sleeping.

Contents

List of abbreviations

MRI	Magnetic Resonance Imaging
RF	Radiofrequency
CSF	Cerebrospinal fluid
FID	Free Induction Decay
TR	Repetition Time
TE	Echo Time
iFFT	inverse Fast Fourier Transform
EPI	Echo Planar Imaging
CNR	Contrast to Noise Ratio
PPI	Partial Parallel Imaging
SENSE	SENSitivity Encoding
SMASH	SiMultaneous Acquisition of Spatial Harmonics
ACS	Autocalibration signal
GRAPPA	Generalized Autocalibrating Partially Parallel Acquisitions
SE	Spin Echo
RARE	Rapid Acquisition with Relaxation Enhancement
FSE	Fast Spin Echo
TSE	Turbo Spin Echo
ETL	Echo Train Length
GRE	Gradient Echo
FA	Flip Angle
IR	Inversion Recovery
MPRAGE	Magnetization Prepared RApid Gradient Echo
DOF	Degrees of Freedom
NUFFT	Non-uniform Fast Fourier Transform

FOV	Field of View
fMRI	Functional Magnetic Resonance Imaging
SPM	Statistical Parametric Mapping
MPT	Moiré Phase Tracking
PET	Positron Emission Tomography
MSE	Mean Squared Error
GE	Gradient Entropy
TA	Acquisition Time
TI	Inversion Time
RMS	Root-Mean Square
GUI	Graphical User Interface
BIC	Bayesian Information Criterion
FD	Framewise Displacement
BW	Bandwidth
XPACE	eXternal Prospective Acquisition CorrEction
MRS	Magnetic Resonance Spectroscopy
DCS	Device Coordinate System
CNN	Convolutional Neural Networks
FSIM	Feature Similarity Index
NGS	Normalized Gradient Squared
PC	Phase Congruency
SSIM	Structural Similarity Index

Research outputs

Journal articles

Elisa Marchetto, Kevin Murphy, Stefan Glimberg, Daniel Gallichan, *Robust retrospective motion correction of head motion using navigator-based and markerless motion tracking techniques*, (in final preparation).

Conference abstracts

1. **Elisa Marchetto**, Maxim Zaitsev, Daniel Gallichan, *Rapid prototyping of a motion-robust 2D Radial GRE sequence with reduced acoustic noise generation using Pulseq*, ISMRM 30th Annual Meeting, 2022.
2. **Elisa Marchetto**, Kevin Murphy, Daniel Gallichan, *Comparison of two retrospective tracking techniques in presence of fast and slow motion*, ISMRM 30th Annual Meeting, 2022.
3. **Elisa Marchetto**, Kevin Murphy, Daniel Gallichan, *Comparing retrospectively corrected motion with two tracking techniques*, Motion Detection and Correction: GatherTown Poster Session, 2021.
4. **Elisa Marchetto**, Kevin Murphy, Daniel Gallichan, *Comprehensive Analysis of FatNav Motion Parameters Estimation Accuracy in 3D Brain Images Acquired at 3T*, ISMRM 29th Annual Meeting, 2021.
5. **Elisa Marchetto**, Kevin Murphy, Daniel Gallichan, *Analysis of FatNav Motion Parameters Estimation Accuracy in 3D Brain Image*, Post Graduate Virtual Meeting 2021, 2021.

Acknowledgment

I would like to start by thanking Cardiff University and TracInnovations for providing the funding for this research. TracInnovations has been an amazing group to work with, showing great passion for their job every day.
I would like to thank my supervisors Dan and Kevin for all the knowledge and support they provided me with during my PhD. In particular, I would like to thank Dan for also being a wonderful person, and "transmitting" all of his enthusiasm for research and science to me.
CUBRIC has been an amazing, welcoming, and dynamic work place, and I am deeply grateful to all the people that I met there and that helped me throughout this journey.
A huge thanks to my bouldering, plants, hikes, and Christmas biscuits lovers for the all of the amazing adventures.
To my marvellous Italian Sunday gang: for all the lunches, dinners and coffee breaks, but mostly for always being there when I needed support or a good laugh.
My deepest gratitude (and apologies) to all the people who voluntarily (or involuntary) proof-read bits and pieces of this thesis.
I cannot be grateful enough to all the people from CUTri, for making it a great place to start or finish my day. Special thanks to my dear friends W. and J.: for swimming, cycling and running with me in calm or rough waters, with tailwind or headwind, and in sunny or rainy weather.
I would like to thank my beloved and enduring trio E., C. and L. because we always find a way to share each others' adventures, despite the km between us.
To my family: for their daily love and support, as well as their astonishing patience with my moods.
And finally to A.: for pushing me to pursue this journey in the first place.

"I think I am quite ready for another adventure"
Bilbo Baggins

Thesis outline

This thesis explores methods to improve the quality of MR images of the brain to continue achieving high resolution images in presence of motion artifacts. The chapters are organized as follows:

- **Chapter 1** gives an introduction to the basic principles of MRI acquisition and reconstruction methods. Motion artifacts are then presented, followed by a description of some motion detection and correction techniques.
- **Chapter 2** shows the implementation and testing of an autofocusing motion correction method to compensate for in-plane rotational and translational motion in brain MRI.
- **Chapter 3** examines the motion parameters estimation accuracy of a fat navigator-based motion correction method using simulated data.
- **Chapter 4** investigates the artifacts arising from different types of head motion during brain structural MR imaging and how well these artifacts can be compensated for using retrospective correction based on fat navigator and markerless-based motion tracking techniques.
- **Chapter 5** uses an open-source framework to design and test different configurations of motion-robust and acoustically optimized MR pulse sequences for infants and paediatric brain MRI.
- **Chapter 6** highlights the main conclusions and outputs of this thesis as well as recommendations for future work.

CHAPTER 1

General Introduction

1.1 Introduction to Magnetic Resonance Imaging

1.1.1 Perturbation of the equilibrium

Magnetic Resonance Imaging (MRI) is a non-invasive imaging modality that uses magnetic properties of hydrogen protons to acquire detailed images of living tissue. In the proximity of an MR scanner, hydrogen atoms present in the body are affected by a strong magnetic field B_0, creating a net degree of alignment between the spins and the magnetic field over time. The hydrogen protons will contrast the alignment induced by the magnetic field perturbation and start rotating around the direction of the applied field. This action is called *precession* and the frequency at which the protons rotate is directly proportional to the strength of the magnetic field B_0, as defined by the *Larmor frequency* [1]:

$$f = \gamma B_0 \tag{1.1}$$

where $\gamma = 42.58\,\mathrm{MHz/T}$ is the *gyromagnetic ratio* for a hydrogen proton.

The interaction between protons and the magnetic field is represented by the net magnetization vector M_0, which is parallel to the magnetic field (pointing along the z-axis by convention). To rotate the net magnetization away from its equilibrium and obtain an MR signal, a *Radiofrequency (RF)* pulse is applied perpendicular to the B_0 field. The RF pulse, also referred to as B_1 field, causes the net magnetization M to tip away from the z-axis by an angle (called *flip-angle*) dependent on the strength and duration of B_1 [2]. As the RF pulse is switched off, the net magnetization vector M will again experience only the B_0 field. The signal coming from the hydrogen protons precessing at the Larmor frequency around the B_0 vector can be detected by placing an RF coil near the region of interest.

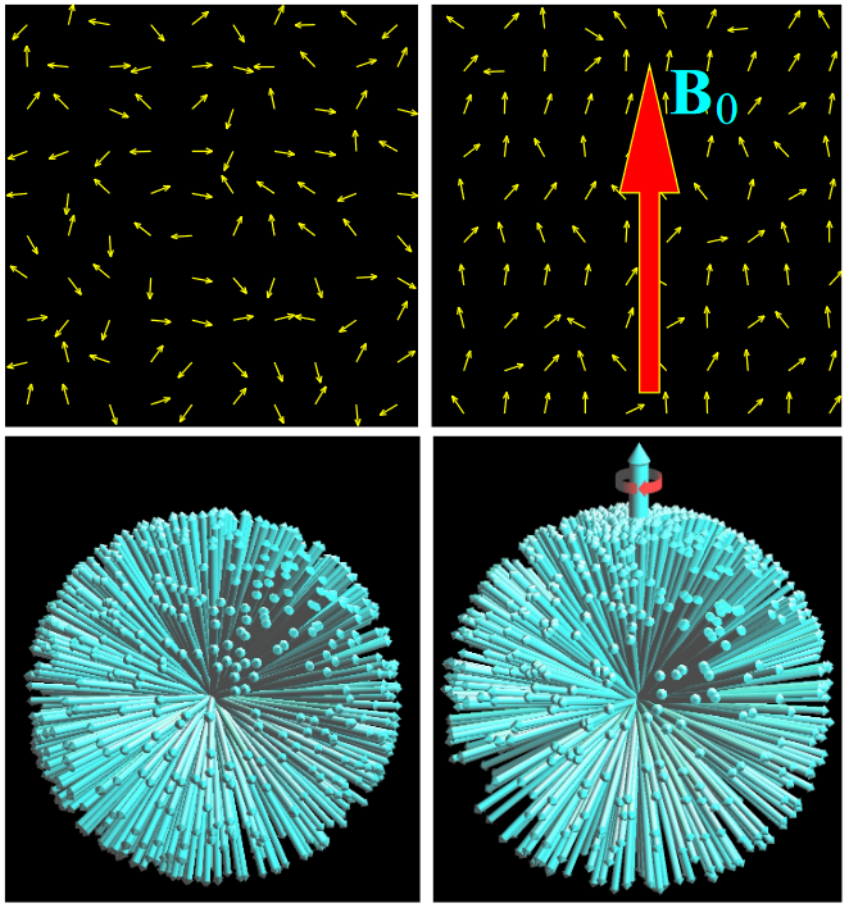

Figure 1.1.1: Left side figures show the behaviour of the spins when no magnetic field is present (no precession). As soon as a strong magnetic field is applied (figures on the right side), the hydrogen spins gradually align in the direction of the B_0 vector, precessing at the Larmor frequency. The interaction between the protons and the magnetic field forms the net magnetization vector M_0 (thick blue arrow), measured in parts per million. Figure from [1].

1.1.2 Timing factors in MRI

As soon as the RF pulse is switched off, the time needed by the net magnetisation to switch back to the equilibrium is generally described by two characteristic times: T1 and T2, also known as the *spin-lattice relaxation* time (or *longitudinal relaxation* time) and *spin-spin relaxation* time (or *transverse relaxation* time) respectively. T1 is defined as the time required by the longitudinal component (M_z) of the magnetization to return to 63% of its initial state, or as the time needed for 63% of the hydrogen protons to switch back to the equilibrium. On the other hand, T2 is the time for the transverse component (M_{xy}) of the magnetization to return to 37% of its initial state, or for the signal to decay of 37% after the excitation.

T1 and T2 are tissue dependent: at 1.5T, the approximate T1 values are 4000 ms, 900 ms and 600 ms for Cerebrospinal fluid (CSF), grey and white matter respectively, while T2 is usually much shorter, with values around 2000 ms, 100 ms and 80 ms [3]. Changes in the magnetic

field strength influence the T1 values [4], with the longitudinal relaxation time increasing up to approximately 1445 ms and 791 ms, for grey and white matter respectively, at 3T [5]. On the other hand, T2 values are similar for 1.5T and 3T [6]. However, the T2 times can vary due to magnetic field inhomogeneities. This originates from susceptibility artifacts, with magnetic field distortions appearing at boundaries of tissues with different magnetic field susceptibility such as air and fat tissue, or around metallic and ferromagnetic objects within the body [7]. These inhomogeneities also affect the spin dephasing or *free induction decay* (FID), causing the signal to decay faster compared to standard T2. The new time constant is called *apparent spin-spin relaxation* or T2*.

If a second RF pulse is applied some time after the first excitation RF pulse, dephased spins can be refocused and a stronger signal can be acquired via RF coils. This second RF pulse is called *refocusing*. The time between the excitation RF pulse and the peak of the RF coil's induced signal (also known as *spin echo*) caused by the refocusing is called *echo time* (TE). The time between two consecutive excitation RF pulses is called *repetition time* (TR). TE and TR are two important timing factors in pulse sequence design as, together with T1 and T2, they dictate the type of contrast (and therefore information) of the MR image. Figure 1.1.2A compares the contrast originated by using different TR values while keeping the TE constant at 10 ms: at TRs below 750 ms, the contrast between grey and white matter is enhanced producing T1-weighted images, with bright and dark regions for tissues with short and long T1 respectively, e.g. fat and CSF. Inversely, the contrast between tissue types is very small at TRs above 1500 ms, as there is almost no difference between the two signals. To intensify the contrast between different tissues, the TE parameter can be changed as shown in Figure 1.1.2B: for the same TR value of 1500 ms, the signal coming from the CSF is much stronger compared to other tissue types for long TE values, while grey and white matter signals are almost identical [8].

1.1.3 The k-space and encoding gradients

MRI data are acquired in the frequency domain, more commonly known as *k-space* or *Fourier-space*. The k-space is where the frequency spectrum of the MR image is saved during the acquisition. It could take the form of a two- or three-dimensional matrix, depending on the type of acquisition. Each point in the k-space contains specific frequency and phase information related to all pixels (or voxels) of the final image. The frequency information is collected during the MR acquisition by applying a specific gradient magnetic field during signal sampling called *frequency-encoding* gradient, which varies along one (or more) dimension causing a change in the magnetic field strength in that direction. The precession frequency is now additionally dependent on the gradient magnitude they are experiencing. In this way, the signal coming from each point is localized in space, with the frequency information enclosed among one dimension of the k-space. To obtain phase information, it is necessary to apply

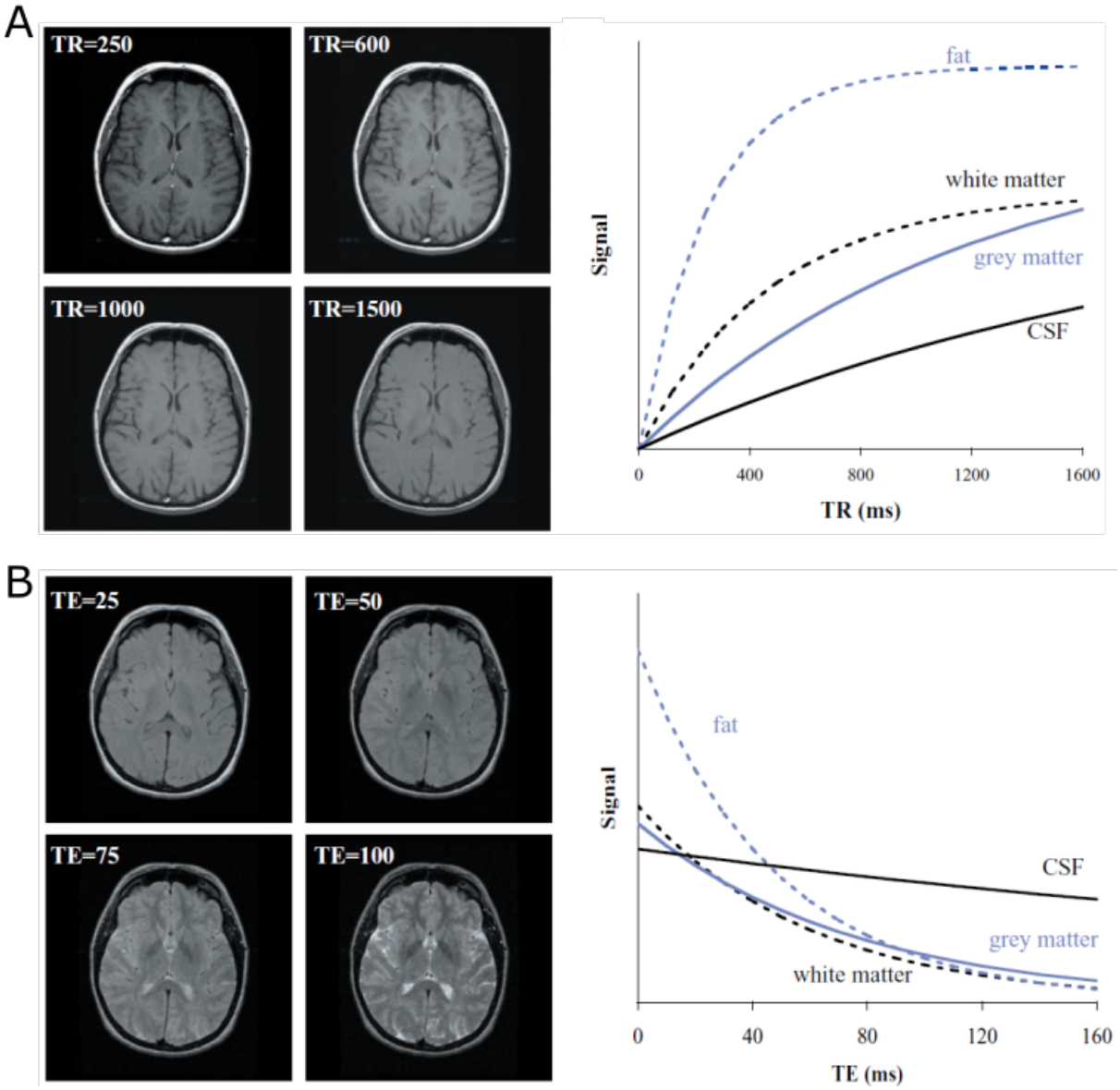

Figure 1.1.2: (A) Images show brain MR data acquired at TE = 10 ms and various TR values. Plots show changes in the signal intensity based on the TR for different tissues. (B) Images show brain MR images acquired at TR = 1500 ms and various TE values. Plots show changes in the signal intensity based on the TE for different tissues. Figure from [8].

a second gradient magnetic field, referred to as the *phase-encoding* gradient, along another dimension in space. This will influence the spins precession frequency, based on the gradient they are experiencing, causing a certain amount of dephasing between spins which will remain after the phase encoding gradient is turned off. This is how the difference in phase is encoded along another dimension of k-space. In order to localize each point in space with specific phase and frequency, multiple phase encoding gradients are applied: for each one, the same frequency encoding gradient is carried out while sampling the signal. RF pulses and gradients can be arranged into a pulse sequence, which is then used to acquire the MR images.

1.1.4 K-space sampling and reconstruction

The MR signal is encoded in the k-space using different trajectories, which dictate the image acquisition and reconstruction strategies. Most commonly, the k-space data is acquired on a rectilinear grid, with each line in the k-space corresponding to the frequency encoding readout for each phase encoding gradient value. This approach is known as Cartesian sampling and it allows to reconstruct the final image by simply applying an *inverse Fast Fourier Transform (iFFT)* to the data. On the other hand, this strategy requires a long acquisition time, due to the fact that single RF pulses are necessary to acquire each line [9]. Figure 1.1.3 shows an example of T1-weighted image in the k-space acquired with Cartesian sampling and reconstructed using the iFFT. Instead of acquiring parallel lines in k-space, it is possible to

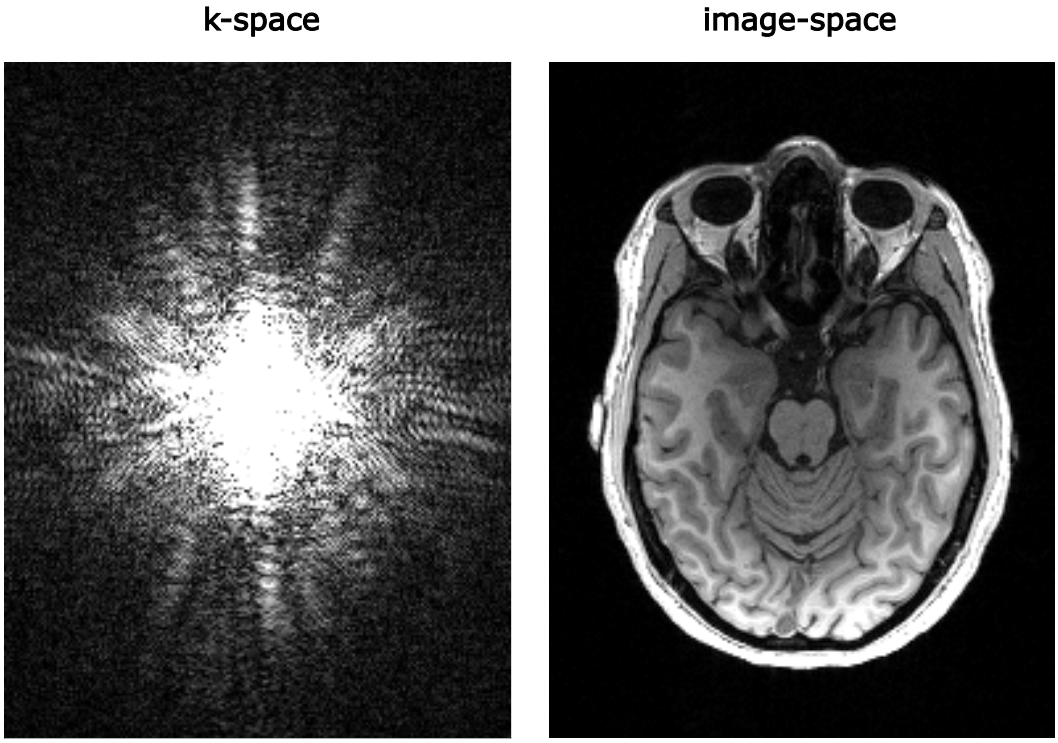

Figure 1.1.3: T1-weighted image acquired with Cartesian sampling before (k-space) and after (image-space) applying the iFFT.

sample it along lines going through the k-space centre, using the so called *radial trajectory*. The main advantage of this technique is its lower sensitivity to motion artifacts than the Cartesian method: as the k-space is acquired at multiple frequencies and phase directions, phase inconsistencies due to motion are spread out in all directions rather than propagate along the phase encoding direction [10]. Moreover, oversampling of the k-space centre can be employed to smooth out motion artifacts due to intrinsic averaging of the subject's gross features [10] or for further motion correction in post-processing [11]. However, the data requires a *regridding* step to fit inside a rectilinear grid before applying the iFFT.

In single-pulse *Echo Planar Imaging (EPI)*, the full 2D k-space is acquired using a single or few RF pulses called *shots*, which further decreases the acquisition time. This technique is particularly prone to ghosting artifacts [9], since the acquisition direction of k-space lines is alternated. Spiral trajectories are also adopted to decrease the scanning time, where the MR signal is acquired starting from the centre of the k-space going outward. The acquired signal is therefore very strong at the beginning of the acquisition, improving the Contrast to Noise Ratio (CNR). This trajectory is often used with small *Field of View (FOV)*, to obtain more signal from the k-space centre region and minimize blurring artifacts caused by off-resonance spins. Figure 1.1.4 graphically shows the k-space trajectories just described. To further reduce

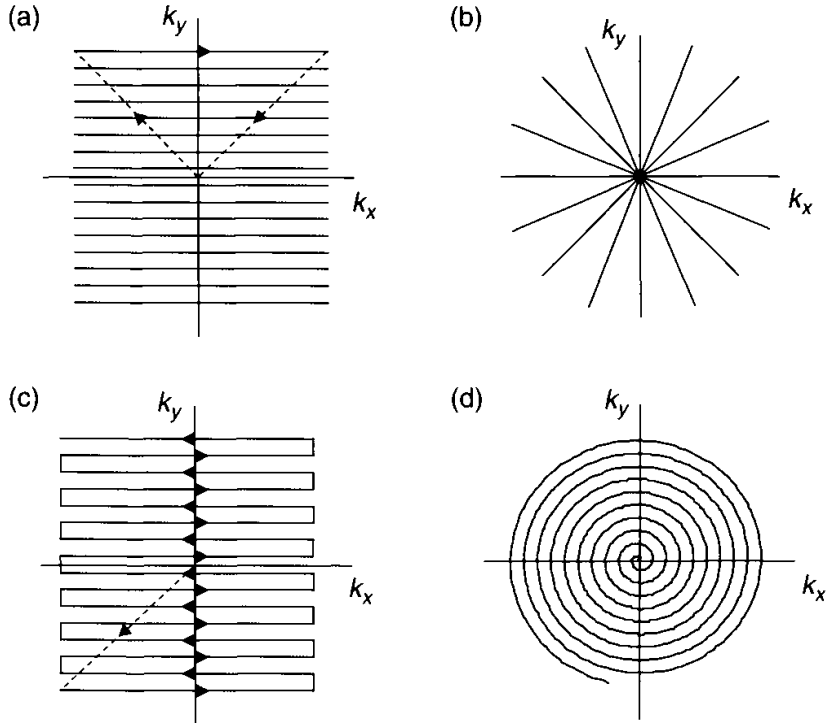

Figure 1.1.4: K-space trajectories for 2D pulse sequences: (a) Cartesian (for non-echo-train sequences), (b) radial, (c) EPI and (d) spiral. Figure from [9].

the acquisition time, *Partial Parallel Imaging (PPI)* methods have been developed to acquire fewer k-space lines and "fill" the missing information using coil sensitivity profiles. One of the main PPI methods is called *SENSitivity Encoding (SENSE)*, developed by Pruessmann *et al.* [12]. The key step in SENSE reconstruction is to calculate the sensitivity maps of individual receiver-coil channel. Each map contains the signal intensity sensitivity, which shows how the signal acquired by each single coil depends on the position of the coil itself and where the signal comes from. Coils' sensitivity maps are used to solve simultaneous equations from the individual aliased images to form the combined final image. SENSE is considered as an "image-space-based" PPI method, as the image reconstruction (via iFFT) is performed before the partial images merging [13]. Another parallel imaging technique that requires coils' sensitivity maps is *SiMultaneous Acquisition of Spatial Harmonics (SMASH)*) [14]. Unlike

SENSE, the data reconstruction is performed prior the iFFT: for this reason, SMASH is considered a "k-space based" parallel imaging technique. An evolution of SMASH is the AUTO-SMASH method [15], which does not require coils' sensitivity maps: the weighting factors are calculated by initially acquiring fully sampled k-space lines called *Autocalibration signal (ACS)*.

The *Generalized Autocalibrating Partially Parallel Acquisitions (GRAPPA)* [16] method is an improved version of the AUTO-SMASH. As the latter, GRAPPA method does not need to use coils' sensitivity maps, which are not always accurately calculated. Instead, fully-sampled ACS lines are acquired from the k-space centre prior or during the undersampled MR sequence. Unlike AUTO-SMASH, the GRAPPA weights are calculated by using multiple acquired k-space data to fit the ACS lines for each individual coil (see Figure 1.1.5). The weights so calculated are then used to reconstruct the unacquired lines of each receiver channel. After reconstructing the missing data, the full dataset can be combined using the sum-of-square function, providing a substantial improvement in the fitting procedure and SNR value compared to SENSE and AUTO-SMASH [16, 17] .

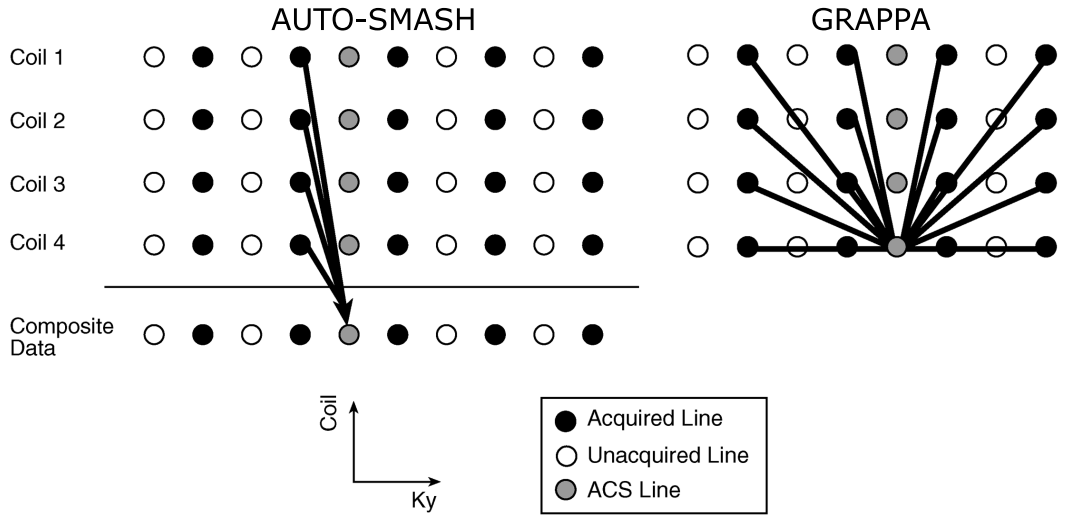

Figure 1.1.5: Comparison between AUTO-SMASH and GRAPPA for $R = 2$. Each circle represents a line in k-space for each coil of the receiver array. In AUTO-SMASH, a single line of acquired data is used to fit an ACS line in the "Composite Data", which is usually the sum of the ACS lines acquired in each coil. On the other hand, GRAPPA uses multiple acquired lines to fit one ACS line from a single coil (Coil 4 in this example). Images taken from [16].

1.1.5 Pulse Sequences

A pulse sequence is a series of events that includes RF pulses, gradients and signal acquisition that allows the generation of the desired MR image. An example is presented in Figure 1.1.6, where the magnetization is initially rotated of 90°, followed by a refocusing 180° pulse. A gradient along the z-axis is applied simultaneously to the RF pulses, creating a *slice-selection* gradient. A so-called *rephaser* gradient is applied straight after the slice-selection gradient but with opposite polarity, to correct for phase dispersion of the transverse magnetization M_{xy}. The magnetization is then dephased by applying a gradient along the x- and y- directions at once, namely the *prephaser* and phase-encoding gradients, to position the k_x and k_y coordinates to the desired k-space location (upper-left side in this case) before applying the *readout* gradient along the x-direction, and start the k-space acquisition. The signal is sampled using an *analog-to-digital* (or ADC) converter. To dephase any remaining transfer magnetization before the subsequent RF pulse (or *excitation* pulse), a *spoiler* gradient can be employed at the end of the sequence. Next sections will briefly introduce pulse sequences relevant for this thesis, to provide sufficient information for the subsequent sections.

1.1.5.1 Spin Echo

Spin Echo (SE) sequences are characterized by a slice selective 90° pulse, followed by a 180° refocusing pulse which generates the echo during which the signal is read [18]. RARE (*Rapid Acquisition with Relaxation Enhancement*) [19] is an adaptation of standard SE techniques used for fast scanning of T2-weighted images. Commercially known as *fast spin echo* (FSE) or *turbo spin echo* (TSE), RARE uses a series of 180° refocusing pulses forming a so called *echo train*: in this way, multiple k-space lines are acquired within the same TR. The number of k-space lines collected during one single TR is called *echo train length* (ETL) or *turbo factor*. Thanks to the 180° refocusing, RARE sequences do not suffer from susceptibility artifacts, which can cause distortions or local signal changes due to local magnetic field inhomogeneities; this makes them favourable to acquire images of the sinuses, skull or areas around metallic objects. However, this can be found disadvantageous when scanning small areas of calcification or haemorrhage [9] because of its insensitivity to magnetic susceptibility effects.

1.1.5.2 Gradient Echo

Gradient Echo (GRE) is an alternative technique to spin-echo sequences. Instead of the 180° refocus pulse, the echo is generated by combining a prephase and a readout gradient of opposite polarity. Moreover, the flip angle used for the excitation pulse is usually less than 90°; in this way, a shorter TR for T1 recovery can be used, allowing faster image acquisition [9].

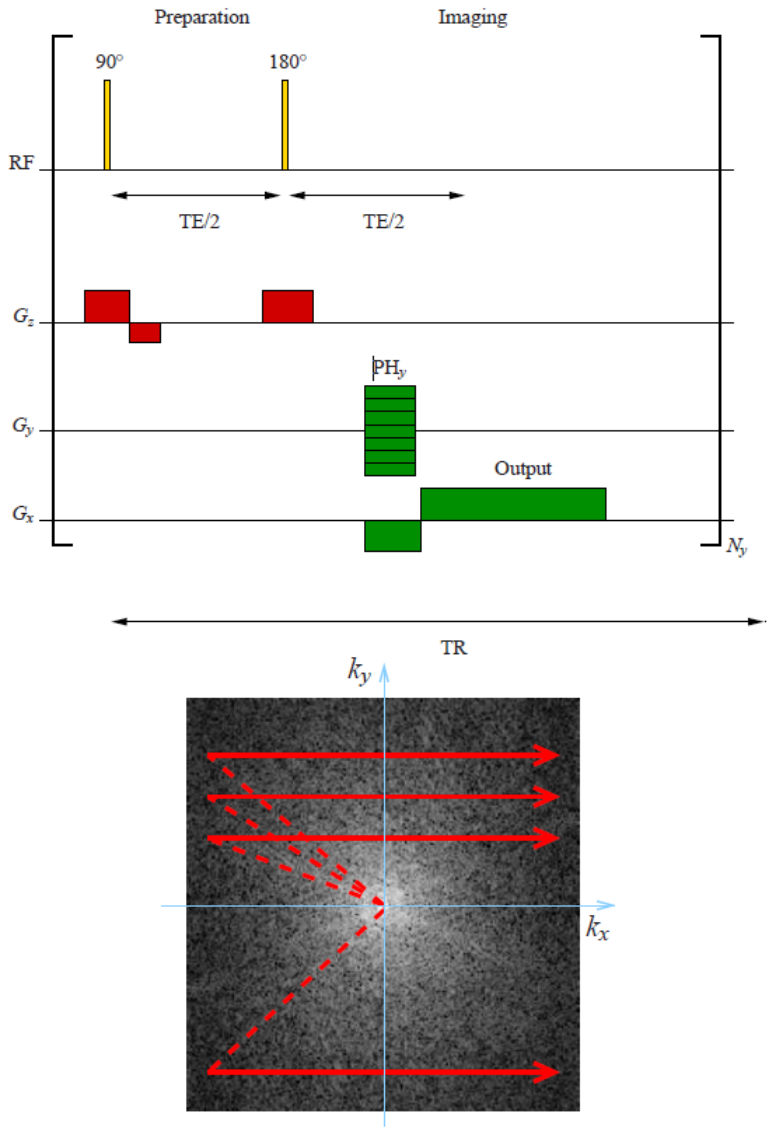

Figure 1.1.6: Schematic representation of a pulse sequence and how gradients are used to sample the k-space. An initial 90° RF pulse is applied, followed by a refocusing 180° RF pulse after a time equal to TE/2. A slice-selection gradient is applied along the z-axis simultaneously to the two RF pulses. A rephaser gradient is applied straight after the first RF pulse to correct for phase dispersion. The magnetization is then dephased by applying the prephaser (G_x) and the phase-encoding (G_y) gradients, moving k_x and k_y from the centre to the upper left corner of the k-space (red dash line). As G_y is switched off and G_x inverted, the readout (output in the figure) of the first k-space line can start. This is repeated for all the k-space lines (N_y), one for each TR. The phase-encoding gradient is changed each step, to read a different k-space line during each TR (PH_y table). Figure from [1].

GRE sequences are more susceptible to magnetic field inhomogeneities compared to RARE sequences, because of the absence of the 180° inversion pulse, making them predominately T2*-weighted. However, this effect can be advantageously used for susceptibility weighted imaging. GRE sequences are also widely used for angiography imaging and to acquire images of haemorrhage, calcification and iron deposition in various tissues and lesions [9].

1.1.5.3 MPRAGE

Inversion recovery (IR) sequences are characterized by a non-selective 180° preparatory pulse (i.e. inversion pulse), followed by standard SE or GRE sequences [9]. The time between the inversion and the excitation pulses is called *Inversion Time (TI)*. This inversion pulse flips all the spins to the opposite direction of the main magnetic field (B_0 field), allowing T1-relaxation during the TI: this way when the next excitation pulse is generated, tissues will be in different magnetization states depending on their T1 times and the TI chosen.

MPRAGE (*Magnetization Prepared RApid Gradient Echo*) is a type of IR sequence, characterized by a preparatory non-selective 180° pulse followed by a "train" of gradient echoes [20]. MPRAGE is most commonly used to acquire 3D T1-weighted images at isotropic resolution, applying short TEs, small flip angles α and long TRs.

1.2 Motion artifacts: detection and correction strategies

MRI images are affected by different artifacts sources [7]:

- *Sequence-related artifacts*: aliasing, partial volume effects, chemical shift artifacts, truncation artifacts, EPI ghosting.
- *Hardware-related artifacts*: spikes, data clipping, zippers, and other artifacts due to external RF sources.
- *Patient-related artifacts*: motion artifacts, susceptibility artifacts.

On a stable MRI system in routine use, motion artifacts are typically the most common source of MRI degradation. Motion can be divided in three categories: *rigid motion* or *bulk motion*, *elastic motion* and *flow* [11]. Rigid motion is a 6 Degrees of Freedom (DOF) kind of motion, described by translations and rotations along the three dimensions (x, y and z). Elastic motion is additionally characterized by scaling and shearing along the three axes, for a total of 12 DOF [11]. Flow motion includes CSF or blood flow and could be one- two- or three-dimensional depending on the complexity of the structure analysed. This thesis focuses on the motion artifacts caused by rigid head motion, therefore other sources and types of motion will not be further described.

Rigid motion affects 2D and 3D imaging differently. When 2D images are being acquired, motion affects only the slice being sampled during that excitation pulse, whereas motion occurring during 3D imaging will affect the entire volume being excited by the RF pulse. However, rigid body motion occurring within slice-selective RF pulses will influence the desired signal, as a different slice might have been excited. This effect is commonly known as spin-history or excitation-history effect [11, 21] and it causes inconsistencies in the k-space being sampled or signal dropout. Incorrect phase accumulation can also cause k-space

inconsistencies, as the spins acquire additional phase due to motion occurring during the application of gradients. The effect of these k-space inconsistencies appears as blurring and ghosting artifacts in the image [11]. Ghosting is a partial or complete replication of object or structure along the phase encoding dimension, while blurring mostly affects edges and sharp contrast areas. These motion artifacts can obscure pathologic conditions and regions of interest [22] or lead to pathology misinterpretation [23], causing the image to be unusable for clinical or research purposes. They can both be caused by involuntary head motion, due to coughing, swallowing, blinking or tremor due to pre-existing neuromotor diseases (e.g. Parkinson), or voluntary motion due to discomfort or distress, which are more likely in less-compliant subject's categories (e.g. paediatric group) [21]. Acoustic noise in MRI has been shown to be another major source of stress and discomfort during MRI acquisitions, together with scan length [24], as well as imposing a health hazard due to the noise level [25].

Motion correction methods have become increasingly important for MRI, due to their ability to estimate the motion occurred and restore quality and resolution of the image, consequentially reducing the scanning time and reacquisition need. Several motion compensation strategies were proposed over the years, which can be summarised in three main categories [21]:

1. *Retrospective motion correction*, consisting of post-acquisition correction using motion information collected during the scan.
2. *Prospective motion correction*, consisting of real-time correction by updating gradients and RF pulses during the acquisition.
3. *Autofocusing*, which is a special type of retrospective motion correction method based on estimating the best motion parameters minimizing a cost function, without any previous knowledge of the motion occurred.

While the latter does not require extra scanning sequences or hardware, retrospective and prospective motion correction methods rely on different strategies to estimate the motion parameters such as MR Navigators [26], [27], [28] or head trackers [29], [30], [31].

The following sections explain the mechanisms behind retrospective, prospective motion correction and autofocusing methods. In particular, a detailed description of a navigator-based and markerless motion tracking approaches is given, which are relevant for the purpose of this thesis. A introduction to acoustic noise in MRI and silent pulse sequences is proposed at last.

1.2.1 Retrospective motion correction

Retrospective motion correction techniques use Fourier properties to correct the MR k-space when affected by motion. If bulk motion occurs during the acquisition, the MR signal is affected by a change in phase and magnitude. According to the Fourier shift theorem, translations can be compensated by a phase correction δ for each point k in k-space [21].

Equation 1.2 represents the transformation from the original corrupted $S(k_x, k_y, k_z)$ k-space data matrix to the corrected $S'(k_x, k_y, k_z)$:

$$S'(k_x, k_y, k_z) = S(k_x, k_y, k_z) \cdot e^{-2\pi i(k_x\delta_x + k_y\delta_y + k_z\delta_z)} \tag{1.2}$$

where k_x,k_y and k_z are the coordinates of each k-space point and δ_x, δ_y and δ_z are the translational motion parameters: if those are known, it is possible to compensate for the displacement occurred along x, y and z.

Based on the property of the Fourier transform, a 2D rotation in the image domain (I), about the centre of the image, is equivalent to a rotation in the Fourier domain (S):

$$I(xcos\theta - ysin\theta, xsin\theta + ycos\theta) \longleftrightarrow S(k_x cos\theta - k_y sin\theta, k_x sin\theta + k_y cos\theta) \tag{1.3}$$

This property is sometimes known as the Fourier rotation theorem [21]; therefore, the effect of a applying a rotation matrix R is noticeable both in the phase and magnitude of the Fourier data, while the translations vector T affect only the phase as shown in Equation 1.4, with k being the k-space sampling trajectories vector (k_x,k_y and k_z) [32].

$$S'(k) = S(R \cdot k) \cdot e^{2i\pi RkT} \tag{1.4}$$

Applying a rotational transformation to the k-space will lead to a k-space sampling that does not fall into a regularly spaced Cartesian grid. This so-called *pie-slice* effect produces regions with lower and higher density points. These low density regions fall below the Nyquist sampling criterion, which violations causes the appearing of striking and ghosting artifacts [11]. Non-uniformly-spaced samples will prohibit the use of the iFFT to convert the image from the Fourier domain to the image domain. The *Non-uniform Fast Fourier Transform (NUFFT)* can be used to compensate for this effect, with the MR signal sampled at unequally spaced frequency. In our work, we used the *Min-Max NUFFT* approach from Jeffrey Fessler (`http://web.eecs.umich.edu/~fessler/code/`) to achieve optimally estimation of the sampling points in k-space [33]. This method estimates the interpolation coefficients that minimizes the maximal approximation error of a non-uniform discrete fast Fourier transform, providing lower approximation errors compared to conventional interpolation strategies (such as Dirichlet, Gaussian bell, and Kaiser-Bessel interpolators) [33].

1.2.2 Prospective motion correction

The idea behind prospective motion correction is to maintain a constant FOV in relation to the moving object. This is performed by sending the tracking data, which represent the head position at that time, to the scanner during the acquisition. This information is then used to adjust RF pulses and gradients to compensate for the rotational and translational motion as

quickly as possible after it has occurred. In particular, the original gradient waveform $g(t)$ is transformed in $g'(t)$ as follows [34]:

$$g'(t) = A(t) \cdot g(t) \tag{1.5}$$

with $A(t)$ representing the affine transformation describing the object movement.

Figure 1.2.1 schematically shows how the phase encoding and slice-selection gradients (here as G_y and G_z respectively) are updated to compensate for a head rotation around the yz-plane: after adjusting the two gradients, the FOV is aligned with the new head position.

Unlike retrospective motion correction, the uncorrected image is not available for comparison, as prospective motion correction is performed in real-time. The motion tracking data can be sent to the scanner for update once "per excitation", "per k-space line", "per slice" or "per volume" depending on the sequence and tracking limits [21]. Latency between the motion parameters estimation and the scanner adjustment must be kept small, to avoid discrepancies between the FOV update and the subject's real head position [34].

The motion parameters can be estimated using different tracking modalities, such as optical tracker [31], navigators [35] or markerless tracking systems [36]. It can be applied to a wide variety of pulse sequences and are generally robust against motion artifacts as they are not affected by Nyquist violations in presence of rotations (i.e. pie-slice effect). They also enable the possibility of an immediate reacquisition of the most corrupted regions of k-space. However, navigator-based prospective motion correction methods are not always compatible with all MR sequences, because of their intrinsic need of extra time to allow the navigator sequence. For example in case of Functional Magnetic Resonance Imaging (fMRI) sequences, re-acquiring lines of the k-space is not always an option due to other tasks involved with the acquisition.

1.2.3 Autofocusing

Autofocusing is a class of motion correction technique that does not rely on motion information from navigators or external tracking systems. The rigid motion occurred is described via a model, where the motion parameters are chosen based on an optimization strategy: a set of motion estimates is applied to lines or groups of k-space lines based on the Fourier shift and rotation theorems; after applying the inverse FFT, the resulting image quality is assessed using a image quality metric as cost function, such as the image entropy [37], [38] and the *Gradient Entropy (GE)* [39]. Autofocusing algorithms assume that the best motion estimates will minimize the cost function value, resulting in a motion corrected image. However, these methods could potentially introduce artifacts if the motion parameters are wrongly estimated and the error propagated through the k-space [40]. Moreover, autofocusing techniques are computationally expensive, although more time-efficient techniques were recently introduced

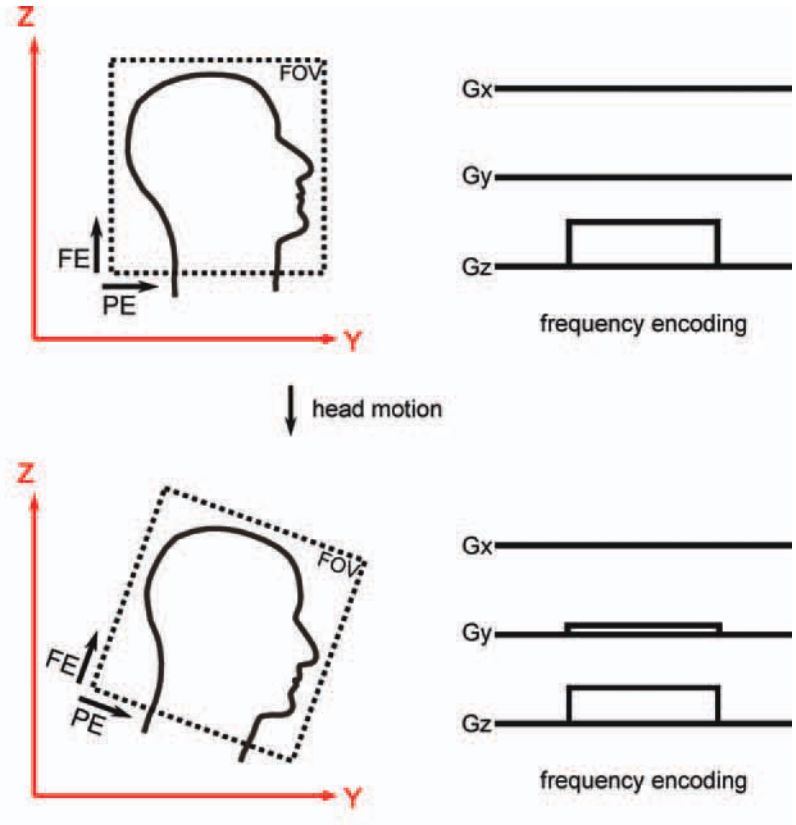

Figure 1.2.1: Schematic representation of gradients update to compensate for head rotations: initially, the frequency-encoding requires only one gradient G_z. To compensate for the head rotation occurred on the yz-plane, both the phase-encoding (G_y) and the frequency-encoding (G_z) gradients are adjusted to align the FOV with the new had pose. Figure taken from [34].

by using prior information from navigators [41] or reference images [42]. Motion tracking techniques could then be complemented by autocorrection approaches to further improve the motion correction especially in case of large changes in the head position, compensating for residual artifacts which might still affect the image [43].

1.2.4 Fat Navigator (FatNav)

A retrospective motion correction technique for brain MRI images has been proposed by Gallichan *et al.* [44] to detect and correct non-deliberate motion in high resolution imaging. The idea consists of apply a 3D GRE sequence combined with a three-pulse fat-selective binomial excitation as the navigator. The natural sparsity of fat-images of the head makes it possible to apply the GRAPPA parallel imaging technique to acquire a 2 mm isotropic resolution FatNav volume in 1152 ms, using a high acceleration rate (R = 16), as shown in Figure 1.2.2 [44]: in this way, small motions can be detected and corrected. The ACS lines used to estimate the GRAPPA weights originate from a fully-sampled FatNav volume acquired at the beginning of the scan. The 3D FatNav volumes acquired are co-registered

during the post-processing pipeline using the *realign* tool from the *Statistical Parametric Mapping (SPM)* to estimate the motion parameters. In [44], image sharpness was restored

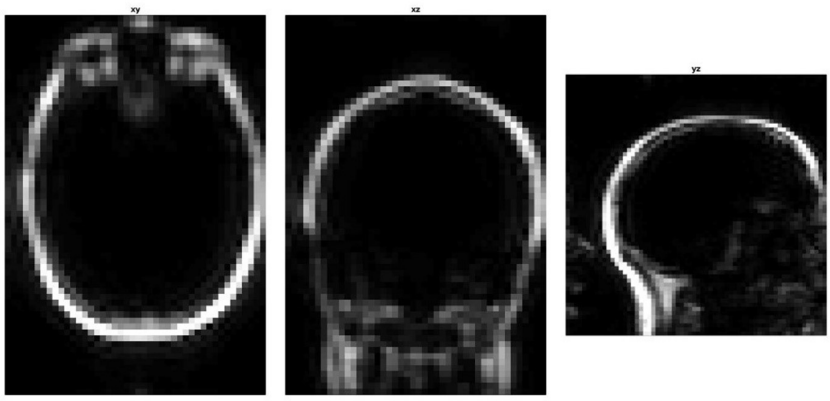

Figure 1.2.2: FatNav volume at 4 mm resolution after GRAPPA reconstruction respectively, from the left, along XY, XZ and YZ axes.

in high resolution images by including the 3D accelerated FatNav's volumes acquisition as part of a MP2RAGE and a TSE protocol without any extra scanning time needed, as shown in Figure 1.2.3. The acquisition of 3D accelerated FatNav volumes can also be incorporated as part of a MPRAGE protocol with only minimal extra scanning time needed (about 2 s for additional GRAPPA calibration for navigators). The use of navigator-based methods

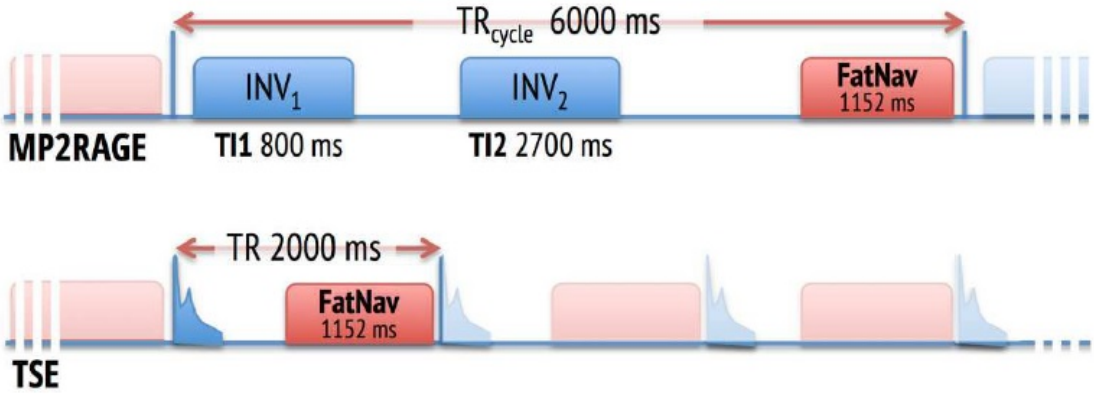

Figure 1.2.3: MP2RAGE and TSE pulse sequences with FatNavs incorporated without any extra scanning time. Figure from [44].

such as 3D FatNavs has the advantage that no extra hardware is required, making it more convenient to use compared to marker-based tracking methods such as the *Moiré Phase Tracking (MPT)* (Metria Innovation, Milwaukee, WI). Unlike FatNav, MPT requires the use of a marker fixed on a mouthpiece extension, which is hold in position by the subject's upper jaw, while a single camera acquires 86 frames/s. The two methods showed comparable results in case of deliberate and non-deliberate motion. Moreover, both techniques could completely

compensate for artifacts caused by slow motion, which may occur in more compliant subjects [45].

FatNavs has also been demonstrated to be a valuable tool for motion correction in clinical brain MRI: in Glessgen *et al.* [46], FatNav was tested in 40 patients with diagnosed or suspected brain tumours on a clinical 3T scanner (MAGNETOM Skyra 3T, Siemens Healthcare, Erlangen, Germany), resulting in visible improvements in image quality after motion correction. Moreover, its negligible additional scanning time and no need for extra hardware makes it suitable for motion correction with less compliant subjects. However, prior work has so far only tested FatNavs in the presence of small non-voluntary motion: it is expected that for large changes in the head position the GRAPPA reconstruction of the FatNavs will be affected and this will reduce the accuracy of the estimation of the motion parameters.

1.2.5 Tracoline (TCL)

Tracoline TCL (v3.01) is a 3D surface tracking system (TracInnovations, Bellarup, Denmark) that allows both prospective and retrospective motion correction of *Positron Emission Tomography (PET)* and MRI brain images, without using external markers: the motion parameters are estimated by acquiring point clouds using a near *Infrared* light system placed on a base unit positioned behind the MR scanner. The light is transferred via a fibre optic cable to a vision probe, creating the point clouds by projecting near-infrared structured light. The vision probe is attached on the MR table, with the support of an MR compatible arm. The probe points towards the subject's face inside the head coil and acquires $\sim$30 point-clouds per minute. These point clouds are then co-registered with a reference point cloud to estimate the motion parameters as shown in Figure 1.2.4. The camera system is connected via a fibre optic cable to a computer in the control room, where the point clouds are visible during the acquisition. The system is provided with a software tool for performing cross-calibration of the reference point cloud with the patient's head from a structural MRI scan. The camera can fit in a Magnetom Prisma scanner (Siemens Healthcare, Erlangen, Germany) using the 20 or 64 channel head coils (Figure 1.2.5). In Frost *et al.* [36], the TCL camera was tested in the presence of voluntary discrete and continuous motion. Discrete motion was performed by changing the head position every minute starting from the centre and then moving left, down, right, up, and returning to the centre. Continuous motion was performed with the subjects rotating their head at 1, 4 or 6 cycles per minute. Prospective motion correction was carried out in two different update modalities:

- *Within-echo-train* (within ET), where the FOV position and orientation were updated every 6 lines of k-space (approximately every 50 ms);
- *Before-echo-train* (before ET), in which the FOV was updated only once per TR.

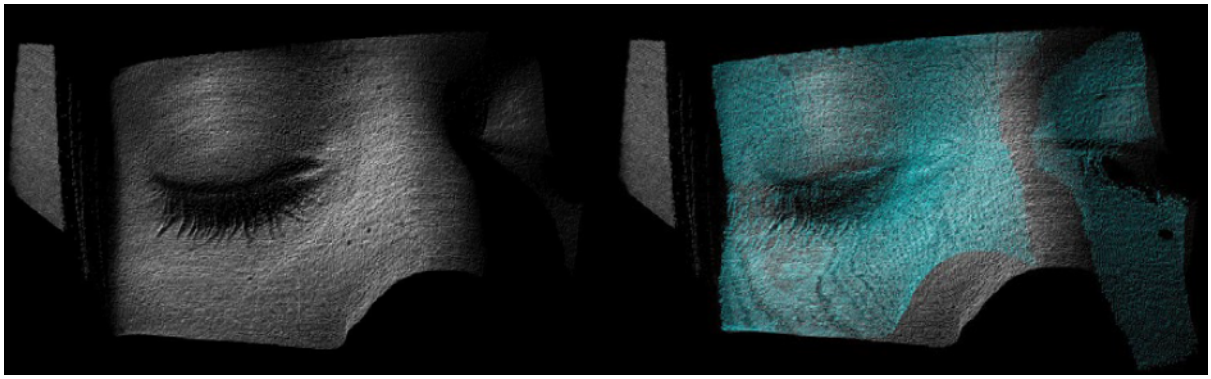

Figure 1.2.4: The reference point clouds (green) are used to register the point clouds (in grey) continuously acquired during the scan. Figure from [36].

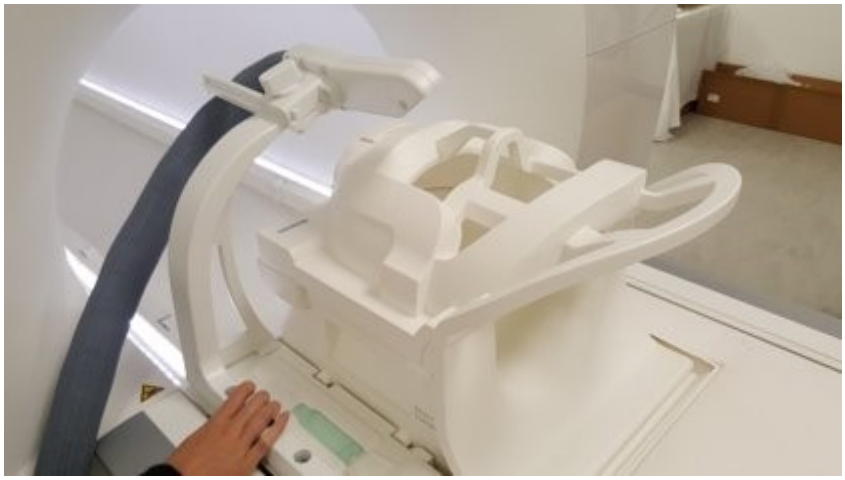

Figure 1.2.5: TCL camera attached to a mock Siemens scanner (ZT) positioned above a 64 channel head coil. Image courtesy of Dr Daniel Gallichan, (CUBRIC) Cardiff University.

With prospective motion correction, the camera first acquires the head movements and turns the information into scanner Device Coordinate System (DCS), before sending them back to the scanner to adjust the gradients based on the tracking data. The results showed that a more frequent update of the FOV reduces the presence of ghosting and signal loss artifacts, in case of continuous motion, due to fewer discrepancies between k-space lines, which can be achieved using the within-ET update. Recently, TCL prospective and retrospective motion correction have been compared in case of discrete and continuous motion [47]. The results suggested that prospective motion correction is generally more robust compared to retrospective in both motion scenarios, thought to be largely because of the reduced effect of localized Nyquist violation.

1.2.6 Acoustic noise in MRI

Acoustic noise in MRI is caused by Lorentz force, an electromagnetic force generated by the electric current flowing through the gradient coils in presence of a large magnetic field. This

force causes the gradient coils to deform and vibrate generating the unwanted MRI acoustic noise. Eq. 1.6 shows that the effect of the Lorentz force vector dF applied to a gradient coil segment dl is directly proportional to the static magnetic field $B0$ and the current vector I [48].

$$dF = dl \cdot (B0 \times I) \tag{1.6}$$

These forces depend on geometry and material properties of the scanner, and its relationship with the resulting noise can be approximated by a linear system [49]:

$$R_i(f) = FT(g_i(t)) \cdot FRF_i(f) \tag{1.7}$$

with $R_i(f)$ being the overall acoustic response of a gradient coil running waveform $g_i(t)$ and the $FRF_i(f)$ representing the frequency response function for each gradient coil $i = x, y, z$.

The acoustic noise generated by the gradient system is particularly pronounced if rapid switching of gradient amplitude is employed [49]. EPI sequences critically rely on fast gradient switching and rise time to acquire a single-shot image within a short time. However, this causes sequences such as EPI to raise an acoustic safety hazard, as the noise level was shown to exceed 130 dB(A) [50].

Reducing the acoustic noise level produced by an MR sequence become necessary to reduce feelings of distress and anxiety which might erase during an MR scan [24]. It would also decrease the risk of adversary events such as hearing impairment or loss, especially on subjects frequently undergoing an MRI scan [25]. Moreover, employing attenuated acoustic noise pulse sequence could be beneficial in clinical or research settings where infants are scanned in natural sleep, and no sedation or anaesthesia are used [51]. Different solutions can be adopted to decrease the noise produced during an MRI scan. *Passive solutions* include ear plugs, sound dumping foams or an acoustic hood placed inside the MR-scanner tunnel [52]. Despite being easy to apply, and not requiring any hardware or sequence modifications, passive systems do not allow uniform protection, as well as having poorer noise attenuation at lower frequencies or against noise transmitted through bone conduction [53]. *Active solutions* include noise cancellation headphones, which have the downside that they will not always fit in the RF head coil. *Quiet MR scanners* can also be adopted as noise control systems, especially with children population. They have been shown to allow a noise reduction of around 20 dB(A) using a non-conductive cryostat inner bore, a low-eddy-current RF coil and non-conductive passive magnetic shims, together with constrained-layer damping and acoustic absorption materials on the outside of the magnet cryostat and the inside of the patient tube [54].

Another approach consists of optimizing the MR pulse sequence to attenuate the acoustic noise produced during the acquisition, which can be performed by adopting different strategies [52, 55]:

- Increase slice width in 2D acquisition.

- Increase RF pulse length, narrowing the bandwidth (BW) or by increasing the FOV without changing the BW.
- Reduce resolution.
- Increase TR.
- Reduce the number of slices or applying parallel imaging techniques.
- Reduce the number of b-values or diffusion directions.
- Minimise gradient switching.

This latter strategy can be achieved using the so-called Ultra-short Echo Time (UTE) or Zero Echo Time (ZTE) pulse sequences. In UTE sequences, the RF excitation pulse is performed right before the gradient ramp-up, with only a negligible delay time. Data acquisition and gradient ramp-up are started simultaneously, which requires sampling of the gradient ramp. However, this often cause image distortions due to gradient hardware delays and eddy currents especially in case of radial sampling schemes, as the k-space centre (and therefore the image contrast) might be impacted [56]. An improved version of UTE sequences is PETRA (Pointwise Encoding Time Reduction with Radial Acquisition) used to acquire T1-weighted 3D image of the brain [57]. PETRA samples the k-space data through two separates acquisition steps. After the first inversion pulse, the centre of k-space is sampled in a Cartesian fashion, while the outer region is collected radially after the second inversion pulse. As the gradient are only changed slightly during each repetition, PETRA achieves outstanding low acoustic noise compared to MPRAGE, from 87.4 dB(A) to 58.2 dB(A), as well as showing [58]. In ZTE, the RF pulse is applied once the gradient has achieved its target magnitude (TE=0). RUFIS (Rotating Ultra Fast Imaging Sequence) is a ZTE sequence for structural imaging, where consecutive readout gradients are ramped straight to the expected value for data sampling, minimising gradient switching [59] and reducing noise level to 55 dB(A) from 90 dB(A) of the conventional sequence [60].

Additionally, it is possible to reduce the acoustic noise by allowing more time to gradually ramping the gradients' amplitude [52]. Noise level reduction can be achieved using the so called *soft gradient waveforms* (e.g. sinusoidal or Gaussian). Unlike the typical trapezoidal shape, soft pulse shapes limit the gradient's frequency range below 200 Hz, allowing to significantly decrease the acoustic frequency response function of the gradient coil. This strategy has been successfully tested in Hennel et al. [61], where three "silent" versions of basic pulse sequences (GRE, SE and RARE) were designed by using sinusoidal gradient slopes, maximising slope durations and minimise the number of slopes. These acoustic optimisations allowed for noise levels as low as 40 dB(A) for GRE and SE and 60 dB(A) for RARE, obtaining a noise reduction of around 40 dB(A) and 22 dB(A) respectively.

CHAPTER 2

GRAPPA-based autofocusing motion correction

2.1 Introduction

Autofocusing is a special case of retrospective motion correction, where the motion information is obtained without using external trackers or navigator sequences: the motion parameters are estimated by iteratively applying the Fourier shift and rotation theorems to the acquired k-space until a cost function is minimized. The cost function, or focus criterion, needs to capture some aspects of how the motion artifacts affect the image quality and should ideally have a global minimum to describe a motion-free image. In the past years, the entropy has been used as focus criterion to iteratively improve sharpness and resolution of MR images affected by 2D translations and a single rotation [37] and in-plane rotations and translations [43].

Loktyushin *et al.* proposed a gradient based motion correction method (*GradMC*) to decrease motion artifacts by using an approach that iteratively searches for the sharpest image measuring the entropy of spatial gradient [39]. This method was successfully used on both real and synthetic data affected by bulk motion, showing major improvements without using any a priori knowledge of the motion parameters.

In recent years, SENSE [12] parallel imaging method has been used for autocorrection of motion artifacts by reducing the data consistency error. This approach has been adopted in Cordero-Grande et al. [62] were SENSE reconstruction was combined with an optimized samples reordering: the incoherent and distributed k-space coverage allowed for an increase motion sensitivity resolved during the image reconstruction. In Haskell et al., Convolutional Neural Networks (CNN) have been combined with a SENSE plus forward model-based reconstruction approach to provide a faster and more accurate motion mitigation strategy [63]. Polak *et al.* [64] proposed a method which uses a rapid 3D scout scan and an optimized sequence reordering to provide accurate motion parameters estimation for each shot: the

image reconstruction is performed only once when the motion parameters are estimated, making this technique computationally fast.

Bydder *et al.* [27] proposed an autofocusing motion correction technique based on the SMASH parallel imaging method [14] to compensate for 2D translational motion in MR images of the shoulder. SMASH uses spatial harmonics to reconstruct missing k-space lines, generated as a linear combination of coil sensitivity profiles acquired prior to the main scan: if one of the acquired k-space lines is considered "motion free", it can be used to predict the data in the consecutive phase-encoding step; differences between the predicted and the "real" (or measured) lines are caused by bulk motion occurring between the two consecutive phase-encoding steps. In Bydder *et al.* [27], the motion parameters were estimated by minimising the difference between the predicted and measured k-space lines using a cost function based on the spatial-harmonics. The motion correction was then propagated along the k-space by comparing consecutive real and predicted lines, restoring the image quality in 2D images of the shoulder affected by 2D translational motion generated by moving the scanner table. This was performed without any previous knowledge of the motion that occurred, and without increasing the scanning time: only one extra acquisition was necessary to calculate coil sensitivity maps. Although the algorithm showed good results both in vivo and on phantom data, its use was limited to 2D translations.

Based on the work of Bydder *et al.*, we developed and tested a new autofocusing motion correction algorithm based on the GRAPPA parallel imaging method [16]. Unlike SMASH, GRAPPA does not require explicit coil sensitivity maps but uses the information encoded in the ACS lines acquired at the beginning or during the scan to calibrate the GRAPPA weights used to reconstruct the missing lines in the k-space. Moreover, GRAPPA works directly on the k-space, allowing to reiterate the optimization algorithm without performing repeated Fourier transformations to the image domain required if SENSE method would be used: the FFT is performed only once to convert the corrected k-space in the image domain.

The algorithm was intended as a robust retrospective motion correction alternative to compensate for in-plane translations and rotations, with the ultimate aim to extend it to correct for 3D bulk motion. The autocorrection method could then be integrated to navigator-based or other motion tracking techniques to compensate for the residual motion artifacts which might still affect the image after the motion correction, as suggested in [43].

2.2 Methods

The next section introduces the models used to describe the motion affecting our brain images, and the mechanism of our autofocusing algorithm for a 2D case. The algorithm works entirely in the Fourier domain: motion parameters are estimated and applied for each phase-encoding

step. The algorithm could be easily extended to 3D, where in-plane slices are acquired during each phase-encoding step.

2.2.1 Motion models

Translational and rotational motion can be described by the Fourier shift and rotation theorem as showed in Section 1.2.1. After compensating for the rotational motion, a regridding (or interpolation) step is required to regrid non-uniformly sampled data into a Cartesian distribution, which is usually performed using the NUFFT methods [33]. However, these methods are usually computationally expensive [65], memory demanding [66] and could introduce errors especially in the image periphery [66], [67].

Toffoli *et al.* [68] introduced the idea of using three consecutive shear transformations to approximate a 2D rotational matrix, as shown in Eq. 2.1: the advantage of using this approximation is that no regridding step is needed, as the data is kept on the Cartesian grid during the shear transformations [69]. Each shear can be implemented as a column- or row-wise translation in the Fourier domain, as described in Eq. 2.2, with F_y representing the Fourier transformation performed along the y-direction. The matrix $S_{y,c}$ displays one shear transformation about the y-axis (Eq. 2.3): the same Fourier transformation carried out about the x-axis and then again about the y-axis, as described in Eq. 2.1, provides a very close approximation to a 2D rotation of an angle α [69].

$$R(\alpha) = S_1 \times S_2 \times S_3 = \begin{bmatrix} 1 & -\tan\frac{\alpha}{2} \\ 0 & 1 \end{bmatrix} \begin{bmatrix} 1 & 0 \\ \sin\alpha & 1 \end{bmatrix} \begin{bmatrix} 1 & -\tan\frac{\alpha}{2} \\ 0 & 1 \end{bmatrix} \tag{2.1}$$

$$M(S_{y,c}k) = F_y\{F_y^{-1}\{M(k)\}e^{i2\pi cyk_x}\} \tag{2.2}$$

$$S_{y,c} = \begin{bmatrix} 1 & -\tan\frac{\alpha}{2} \\ 0 & 1 \end{bmatrix} \tag{2.3}$$

In this study, we tested our autofocusing algorithm in the presence of translational motion, in-plane rotations and translations, and with rotations approximated by shears in the Fourier domain.

2.2.2 GRAPPA-based algorithm

The first phase-encoding line was considered as the initial "motion-free" head position. The GRAPPA algorithm could then use this line to estimate the GRAPPA weights and "predict" the second k-space line, via the GRAPPA reconstruction pipeline available from the *retroMoCoBox* [70]. A GRAPPA kernel of 2x3 (2 phase encoding by three partition encoding steps) was adopted to fit the ACS lines and estimate the GRAPPA weights. The final reconstruction was averaged across the receive-channels. An optimization strategy was adopted to find

the motion parameters that minimized the value of the cost function estimated between the GRAPPA-predicted and the real phase-encoding steps. The motion parameters δ, for translations, and α, for rotations, were initially assigned a value of $\delta = 0$ and $\alpha = 0$ at the start of the optimization algorithm. The parameters were then applied to the real phase-encoding step using the Fourier shift and rotation theorems for translations and rotations respectively, producing an initial corrected version of the second phase-encoding line. The predicted and corrected lines were compared using the *Mean Squared Error (MSE)* as cost function:

$$MSE = \frac{1}{n}\sum_{i=1}^{n}(X_i + X_i')^2 \tag{2.4}$$

with X_i and X_i' the values of each sample i (with $n = 200$)of the predicted and corrected k-space lines respectively. Differences in the two lines (X and X')denoted a change in the head position between the first and second encoding steps, and therefore the presence of motion artifacts.

Different values of δ and α were iteratively applied to the real second phase-encoding line until the MSE value reached its minimum; this process was performed by the MATLAB function *fminunc* (Mathworks, Natick, MA) using the default option's values: the search for the minimum value would stop if a step smaller than the tolerance ($TolX = 1e^{-6}$) was attempted. Once found, the motion parameters that minimized the cost function were applied to the real second phase-encoding line.

Each line corrected this way could then be used by the GRAPPA reconstruction to predict the following k-space line, which would be compared with its corresponding real line during a new optimization cycle. Line by line, the correction can propagate across the entire k-space. A graphical explanation of the algorithm is given in Figure 2.2.1.

2.2.3 Experiments

The algorithm was tested on 2D and 3D MR images of the brain. We used the MNI152 T1-weighted atlas (2 mm isotropic resolution) [71] as 3D volume, with 8 receive-channels simulated using MATLAB, and the 2D image (8-channels RF coil) from the SPIRIT toolbox [72]. The images were artificially corrupted by simulated motion profiles so that the true motion in each case would always be known. The algorithm was initially tested only against translational motion and then extended to in-plane translations and rotations. In particular, the following tests were performed:

- 2D image retrospectively corrupted by 1D translational motion;
- 2D image retrospectively corrupted by 2D translational motion;
- 3D image retrospectively corrupted by 3D translational motion;
- 2D image retrospectively corrupted by in-plane translational and rotational motion;

- 2D image retrospectively corrupted by in-plane translational and rotational motion by shears.

The motion applied was randomly generated within a range of ± 4 mm of translations and $\pm 4°$ of rotations. The rough behavior of the motion parameters was generated using a "value" version (essentially blurred white noise) of the original *Perlin noise* [73, 74]. Translational and rotational motion was applied to 2D data using the Fourier shift and rotation theorems, while the retroMoCoBox was adopted to apply motion in the case of 3D volumes, as it can be used to simulate the effect of motion, as well as for correcting it.

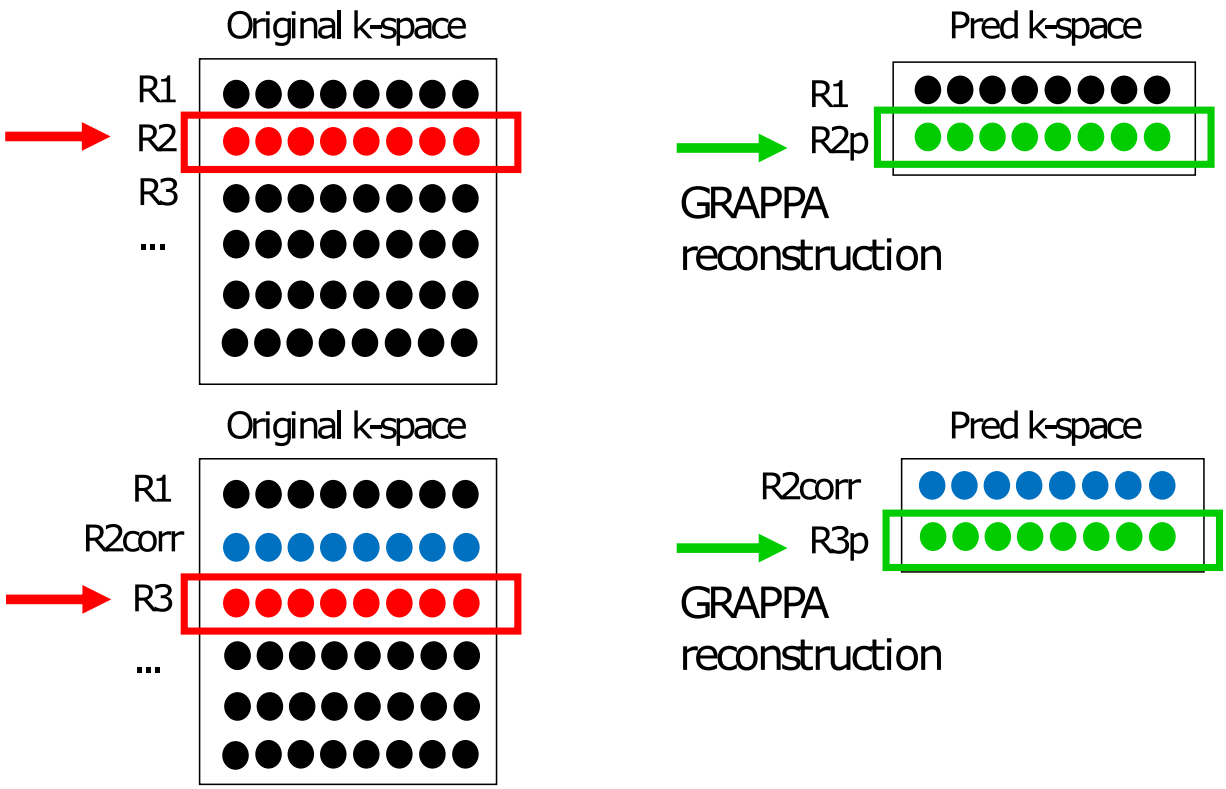

Figure 2.2.1: Schematic representation of the GRAPPA consistency algorithm steps: the first k-space line (R1) is considered as the initial head position (motion-free) and used to predict the second k-space line (R2p). The real second k-space line (R2) is compared with the predicted line (R2p) via a cost function optimization algorithm; the motion parameters, that minimize the cost function, are use to retrospectively correct the real second line (R2corr), which is then used to predict the next line (R3p) in k-space. The correction is propagated to the third line of the k-space (R3) until the entire k-space is covered.

2.3 Results

2.3.1 1D translational motion

Figure 2.3.1 shows that the algorithm correctly compensated for the 1D translational motion applied along the phase-encoding direction of a 2D brain image: the ringing artifact originated by the phase shift applied in the k-space is visibly reduced after the motion correction, despite some residual artifacts still being visible on the frontal brain area. The true and estimated motion parameters are compared in Figure 2.3.2: the algorithm generally performed well, creating a close match of the estimated motion parameters and the true parameters across the majority of k-space. However, the quality of the estimates is notably reduced in the first and last 10 lines or so of k-space. Root-Mean Square (RMS) values are reported on top of Figure 2.3.2.To quantify the effective difference between the images before and after motion correction, the consistency between the original and the corrupted (before correction) image was calculated as difference between the two data in the image domain. This consistency between "original vs corrupted" and "original vs corrected" is shown in 2.3.3. This figure clearly demonstrates how the correction has reduced the ringing effects across the whole image – but the strong differences remaining along the edges suggest it may perform less well on the fat layer in this case.

As the k-space centre contains the information regarding contrast and shape of an MR image [9], we tested whether initiating the algorithm from the central phase-encoding step would improve the motion parameters estimation accuracy. The same set of 1D translations was used, with zero-motion in the centre of the k-space. The algorithm accurately calculated the motion parameters especially towards the centre of the k-space, as shown in Figure 2.3.4. The ringing artifacts caused by the translational motion were nicely reduced after the motion correction, as shown in Figure 2.3.5. However, the accuracy is again shown to decrease towards the beginning and the end of the estimates' curve. Nevertheless, initiating the autofocusing algorithm from the central phase-encoding step resulted in a stronger correlation between the real and the estimated parameters (MATLAB function *corrcoef*, $r(198) = 0.69$, $p = 3.7e^{-30}$) compared to when the first k-space line was used as first prediction step ($r(198) = 0.63$, $p = 2.61e^{-24}$). Therefore, the central phase-encoding step was used as starting point of the autofocusing algorithm in all the following experiments.

2.3.2 2D translational motion

Good improvements were obtained in the case of 2D translational motion as shown in Figure 2.3.7, where the image sharpness is completely restored after applying the autofocusing algorithm. Motion parameters were estimated accurately especially in the centre of the k-space in both the x- and y-dimension, as shown in Figure 2.3.8: differences in the motion magnitude

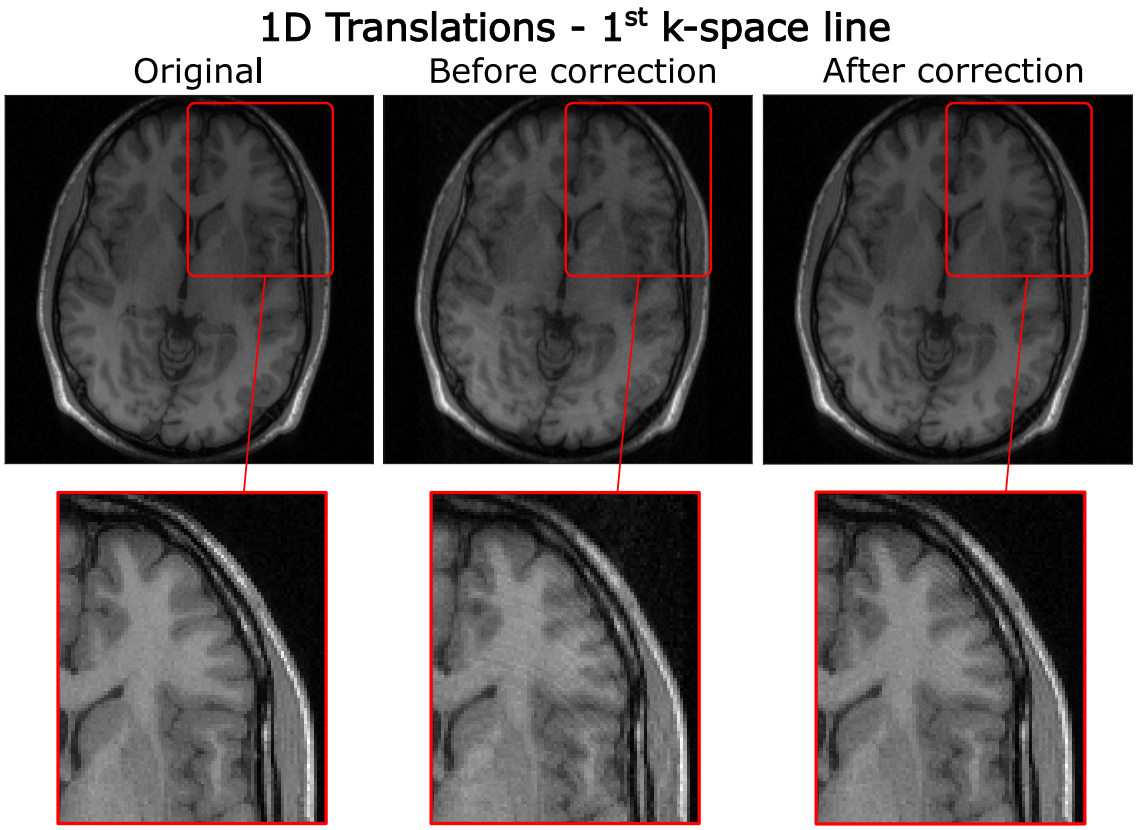

Figure 2.3.1: Comparison between the original (no motion), before and after motion correction images affected by 1D translations. The autofocusing algorithm was initiated from the first phase encoding step (first k-space line). The autocorrection visibly reduced the ringing artifacts compared to the uncorrected image as shown in the magnified sections (red frames).

between the two motion traces arose at the beginning and towards the end of the k-space, which causes the two RMS values to be quite different between real and estimated parameters. The consistency test shown in Figure 2.3.9 confirmed that the motion correction algorithm improved the image quality, with small remaining ghosting artifacts still visible.

2.3.3 3D TRANSLATIONAL MOTION

The algorithm is shown to improve the image sharpness in case of 3D translational motion applied on a 3D volume as shown in Figure 2.3.10. The real and the estimated motion parameters along the three directions have different magnitude values as outlined by the RMS, but they are shown to follow the same motion behaviour in Figure 2.3.11. The consistency test reported in Figure 2.3.12 shows that, despite some small improvements in the image quality, motion artifacts are still visible especially around the skull and in the corpus callosum.

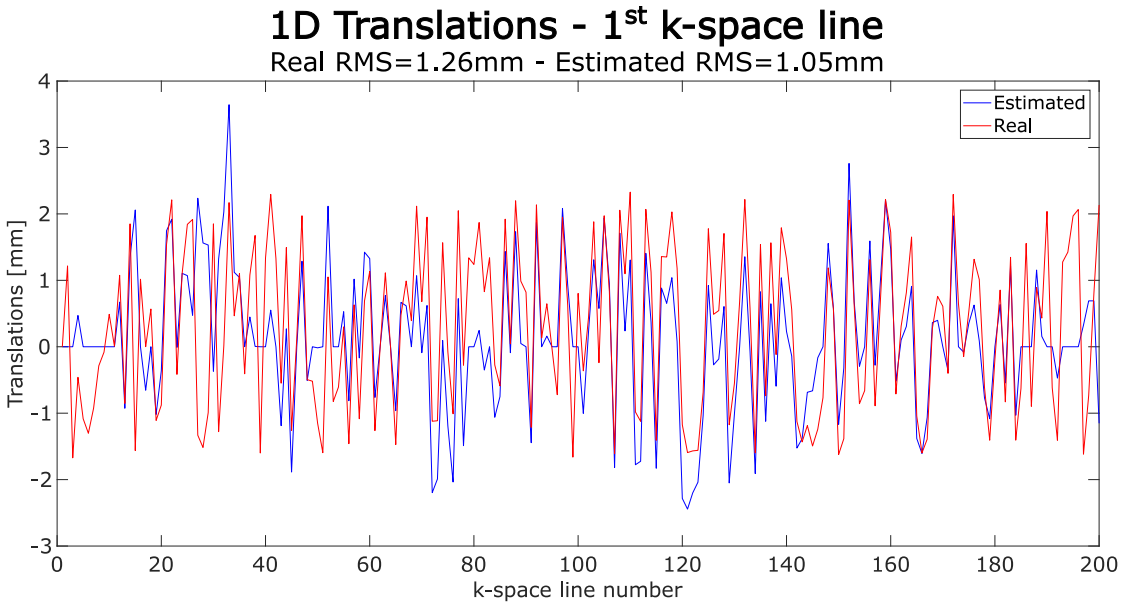

Figure 2.3.2: Comparison between the real 1D translations applied (red line) and ones estimated by the algorithm (blue line). The autofocusing was started from the first phase-encoding step (first k-space line). The RMS values of the real and estimated motion parameters are reported on top of the image. The algorithm worked well across the majority of the k-space, with a reduction in the estimates quality around the first and last 10 k-space lines.

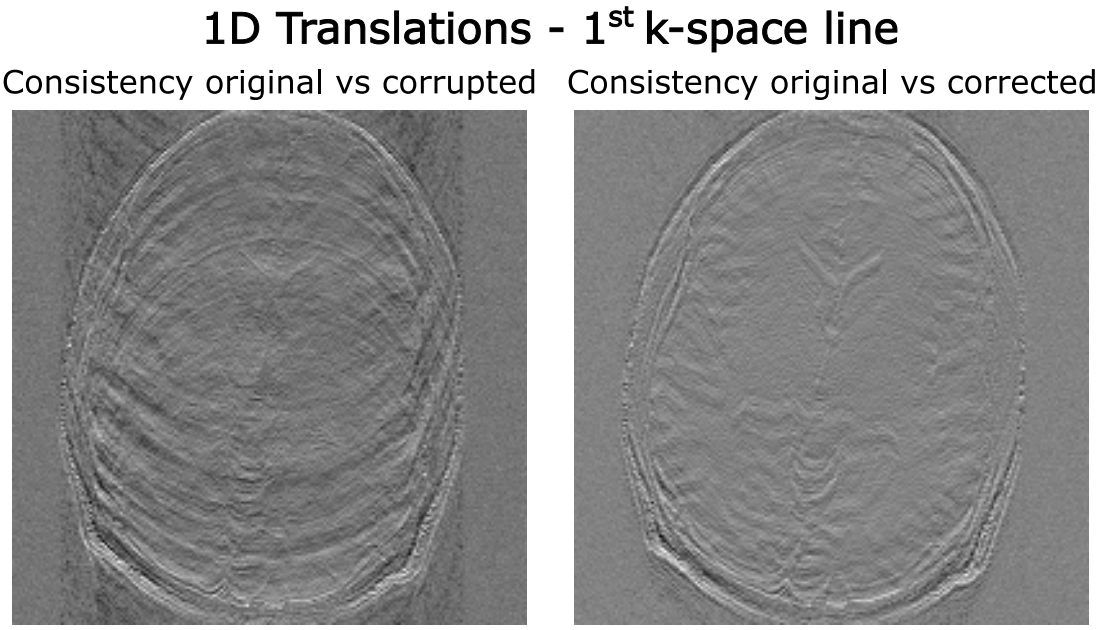

Figure 2.3.3: Comparison between the consistency calculated between the original and the image corrupted by 1D translations ("original vs corrupted") and between the original and the image after applying the autofocusing correction starting from the first k-space line ("original vs corrected"). Artifacts are clearly reduced compared to the original vs corrupted comparison.

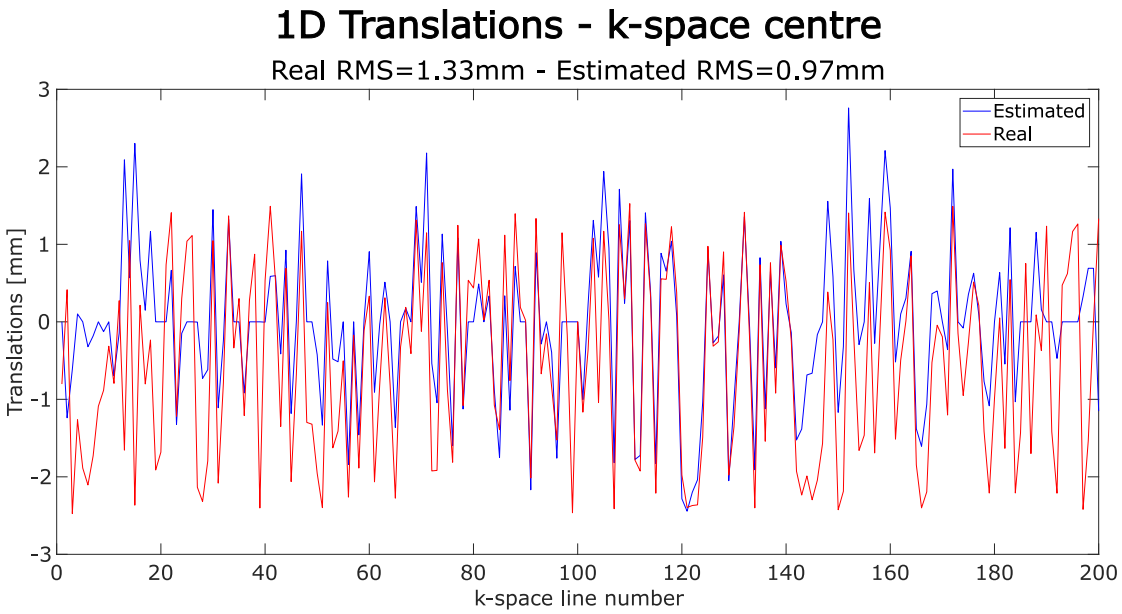

Figure 2.3.4: Comparison between the real 1D translations (red line) and ones estimated by the algorithm when starting from the central phase-encoding step (blue line). The RMS values of the real and estimated translations are reported on top of the image. The motion parameters are well estimated in the majority of the k-space. However the estimation accuracy is shown to decrease towards the beginning and the end of the k-space.

2.3.4 2D TRANSLATIONAL AND ROTATIONAL MOTION

The algorithm was also tested in case of in-plane translational and rotational motion applied on 2D images using the Fourier rotation and shift theorems. Both translations and rotations were not accurately estimated: the correction even seemed to lead to a reduction in the image quality compared to the uncorrected image, as shown in 2.4.1. The motion parameters estimated for translations and rotations are reported in Figure 2.4.2: the motion traces show similar RMS values especially in case of rotational motion, but the estimated parameters are very different from the real ones. The reduced image quality after the motion correction is corroborated by the consistency test, with stronger differences between the original and the corrected images compared to the original and uncorrected ones 2.4.3.

To investigate whether the correction of rotational motion failed because of the necessary regridding step, the *rotations-by-shearing* method was tested, with 2D rotations approximated by three consecutive shear transformations: this way, the interpolation step is not required, as the shears preserve the shape of the Cartesian grid. Unlike the previous motion cases, shear transformations had to be applied to the entire k-space, instead of the single phase encoding step, to obtain the correct approximation: the line of interest could then be considered after "rotating" the entire frequency matrix. The Fourier shift theorem was again used to estimate and correct for the translational motion occurred. Clear improvements were visible in the corrected image compared to the uncorrected one, as shown in Figure 2.4.4. However, the

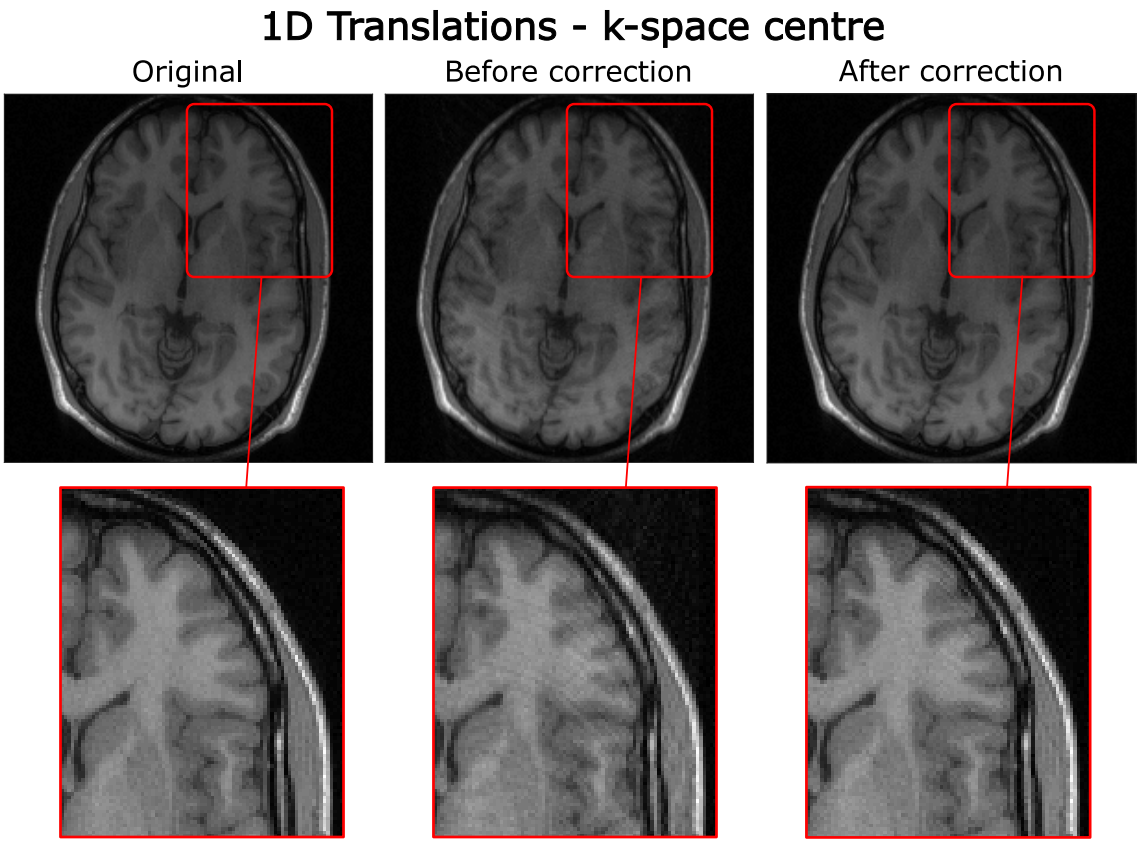

Figure 2.3.5: Comparison between the original (no motion), before and after the correction of a 1D translational motion, when the autocorrection was initiated from the central phase-encoding step (k-space centre). Ringing artifacts are clearly reduced after the motion correction as shown in the magnified sections (red frames).

rotations could not be accurately estimated by the algorithm using the shears approximation. On the other hand, translations were nicely estimated both along X and Y directions, especially around the k-space centre, as shown in Figure 2.4.5.

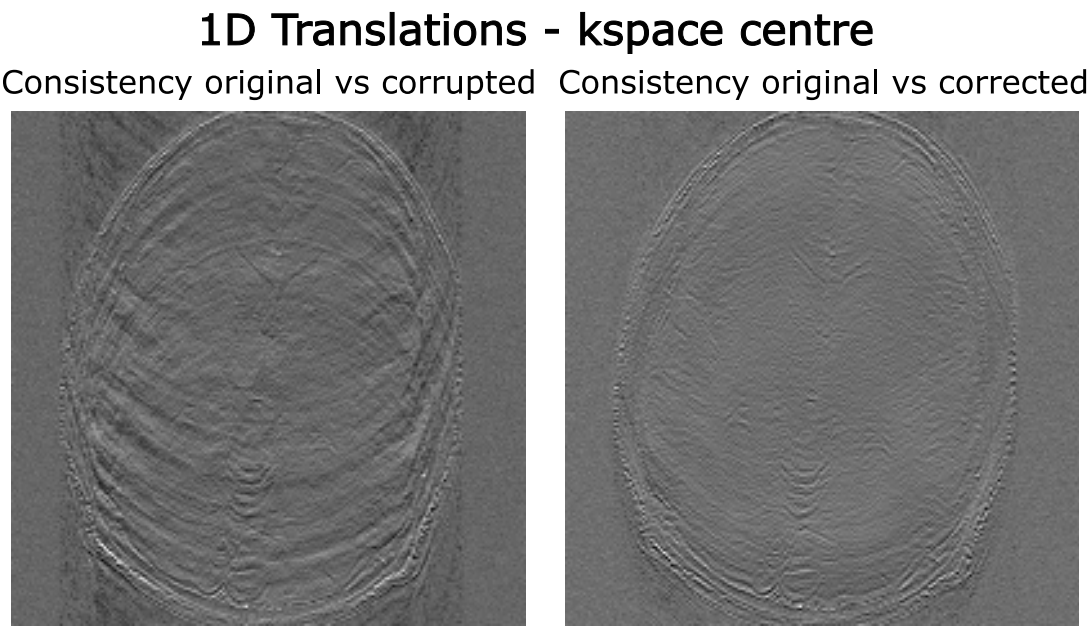

Figure 2.3.6: Comparison between the consistency calculated between the original and the image corrupted by 1D translations ("original vs corrupted") and between the original and the image after applying the autofocusing correction starting from the central k-space line ("original vs corrected"). The correction visibly reduced the ringing artifacts.

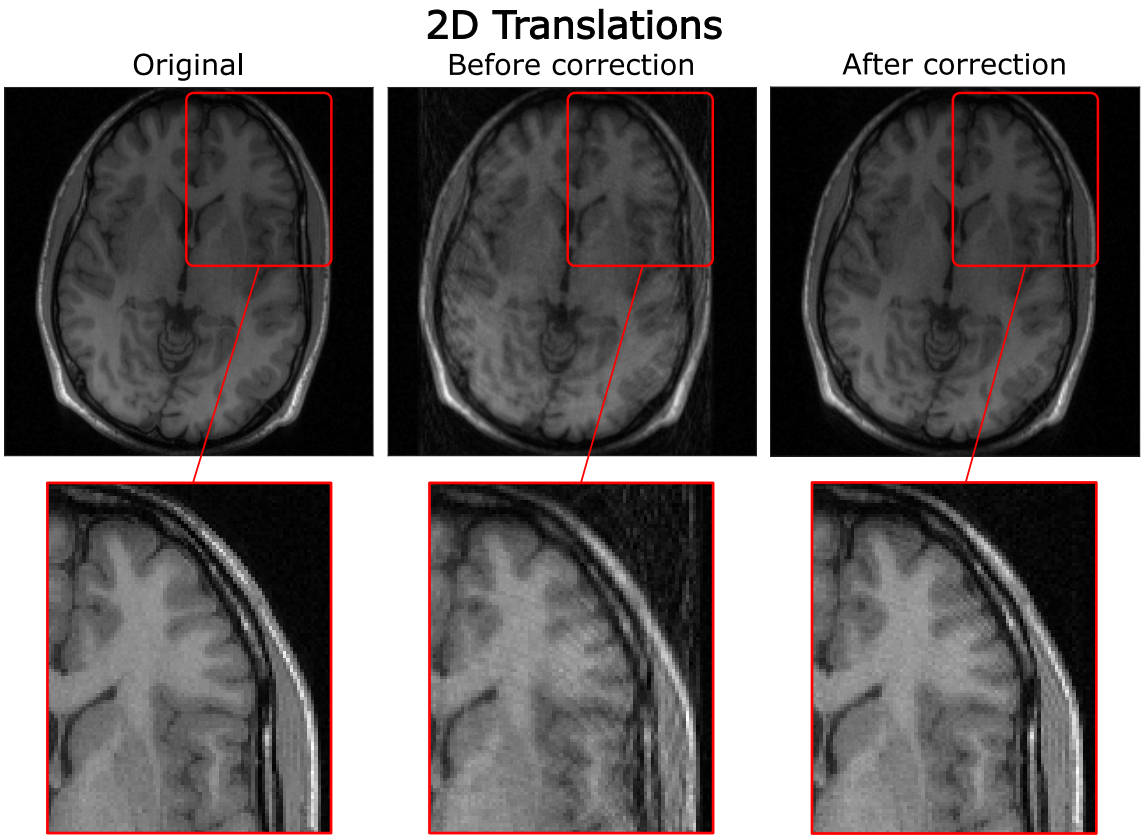

Figure 2.3.7: Comparison between the original (no motion), before and after the correction of 2D translations along the X and Y directions. The motion correction visibly improved the image sharpness compared to the uncorrected one, as displayed in the magnified sections (red frames).

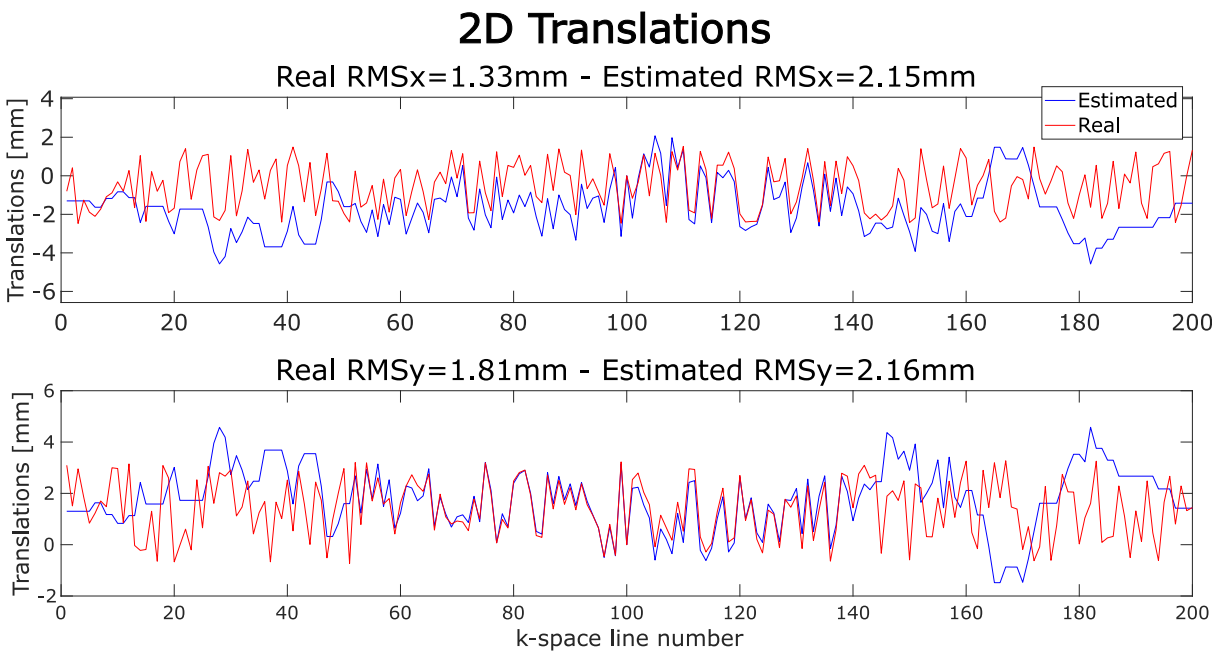

Figure 2.3.8: Comparison between the real 2D translations (red line) and ones estimated by the algorithm (blue line) along the x- and y- dimension. RMS values for real and estimated motion parameters are reported on top of each motion trace. The algorithm estimated the motion parameters more accurately around the centre of the k-space.

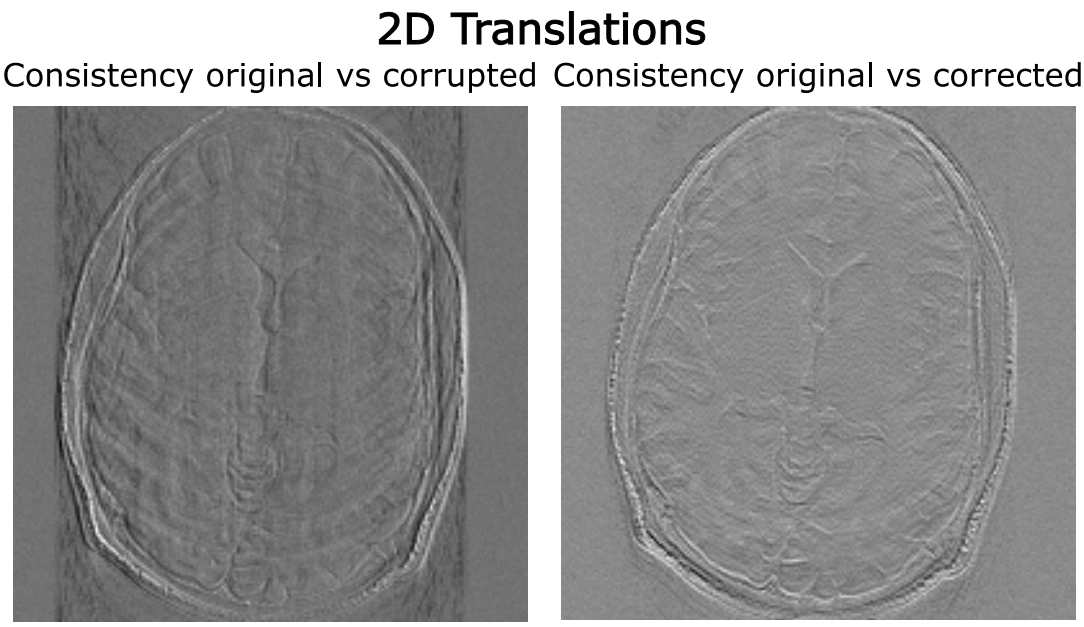

Figure 2.3.9: Comparison between the consistency calculated between the original and the image corrupted by 2D translations ("original vs corrupted") and between the original and the image after applying the autofocusing correction ("original vs corrected"). The latter shows less discrepancies with the original image compared to the original vs corrupted.

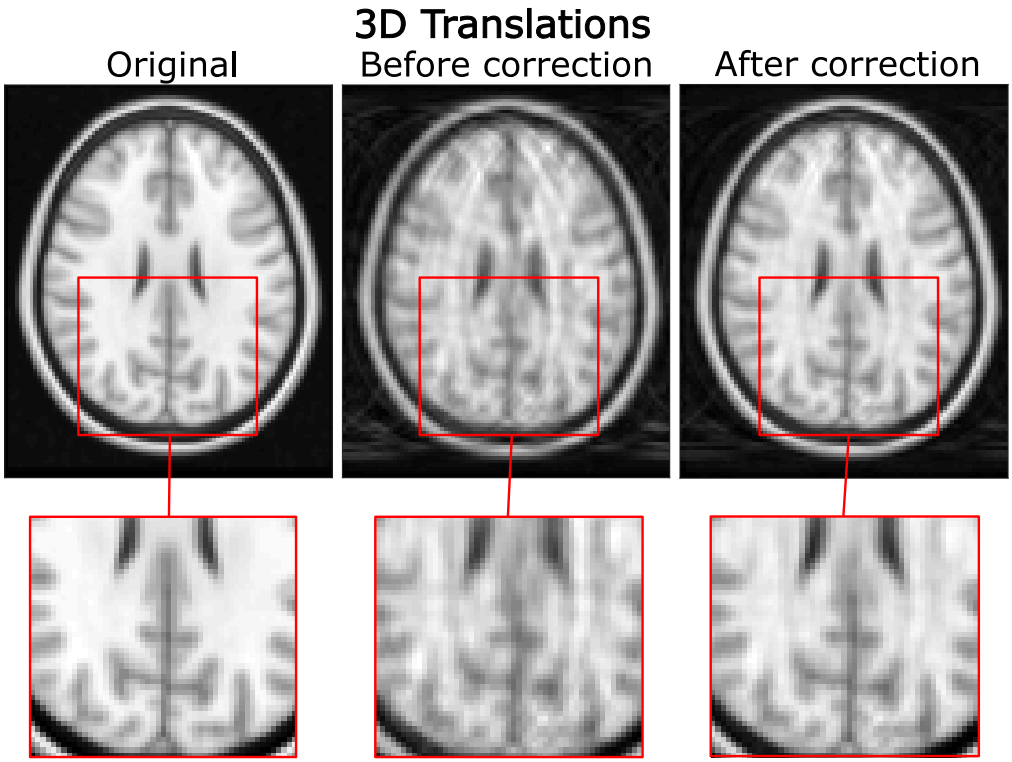

Figure 2.3.10: Comparison between the original (no motion), before and after the correction of a 3D translations: less ringing artifacts were present after the motion correction compared to the uncorrected image.

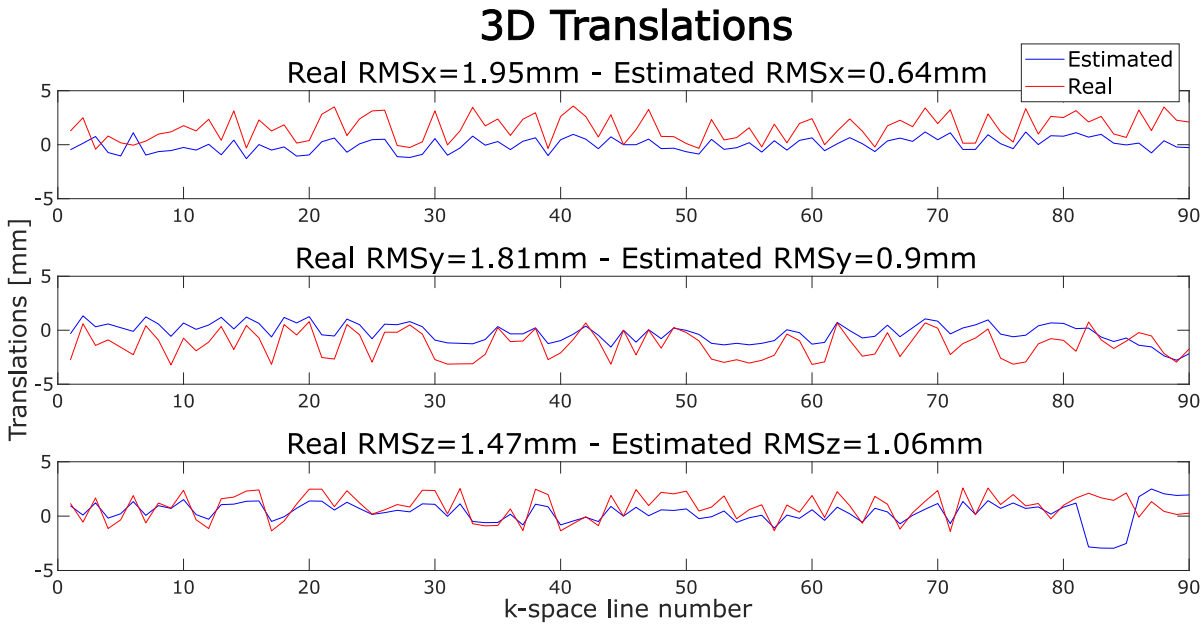

Figure 2.3.11: Comparison between the real 3D translation (red line) and the ones estimated by the algorithm (blue line) along x, y and z. RMS values for the real and estimated motion parameters are reported on top of each motion trace. Despite the difference in magnitude compared to the real parameters, the algorithm seems to have correctly estimated the motion behaviour along the three axis.

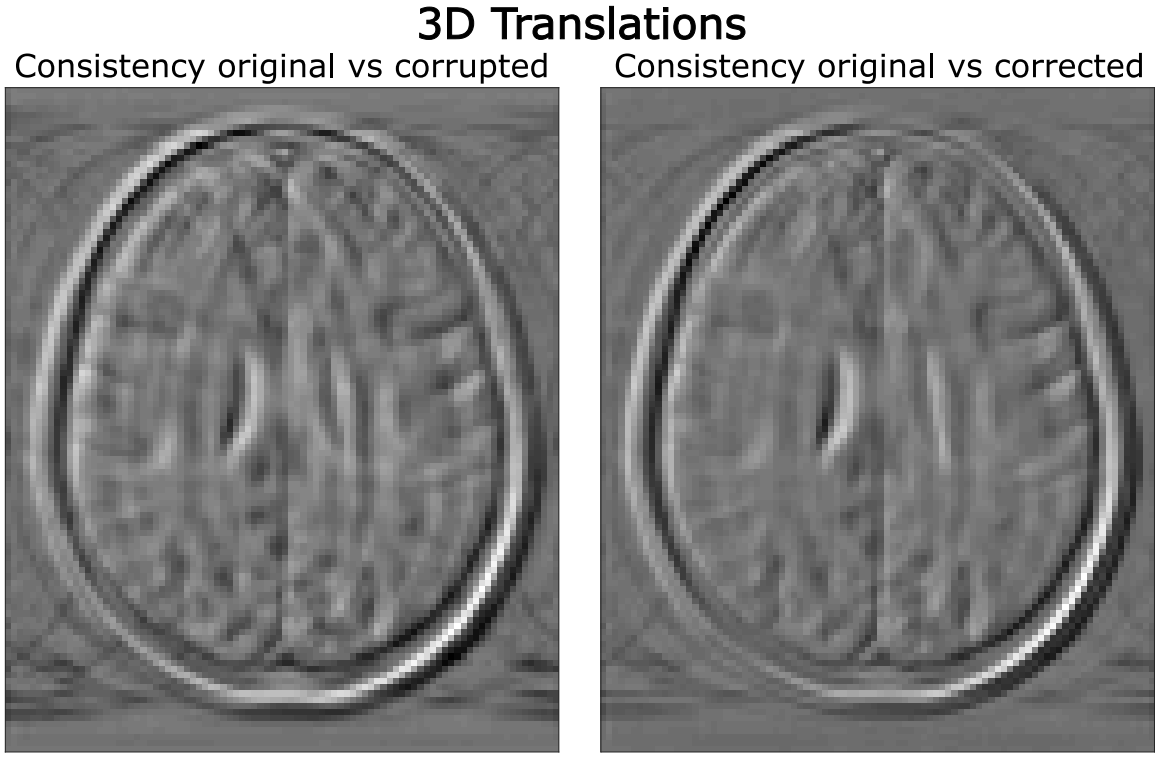

Figure 2.3.12: Comparison between the consistency calculated between the original and the image corrupted by 3D translations ("original vs corrupted") and between the original and the image after applying the autofocusing correction ("original vs corrected"), which shows a clear reduction in motion artifacts compared to the original vs corrupted.

2.4 Discussion

In this study, we developed and tested an autofocusing algorithm to compensate for bulk motion affecting MR images of the brain: the algorithm does not use any previous knowledge coming from navigators or external hardware to estimate the motion that occurred. The motion parameters are estimated via a cost-function minimization strategy, where the cost function describes the quality of the image achieved with that set of motion parameters.

The algorithm was developed based on the SMASH-based autofocusing method proposed by Bydder *et al.* to compensate for 2D translational motion on 2D images of the shoulder generated by moving the scanner table [27]. The SMASH parallel imaging technique is based on the prior acquisition of coil sensitivities, which is influenced by the shape and number of the receiver array as well as motion.

In our study, we adopted the GRAPPA parallel imaging technique as it has the advantage that the coil sensitivities profiles are derived from the ACS lines obtained directly from the acquired data. GRAPPA was used to predict lines in the k-space based on the knowledge of the previous ones, which were considered as motion-free. The choice of the GRAPPA kernel ($2x3$) made possible to estimate the translational and rotational motion only between two consecutive k-space lines: although computationally faster, the estimation accuracy might reduce in presence of large head rotations due to the pie-slice effect affecting multiple k-space lines. The algorithm was firstly tested in case of 1D, 2D and 3D translational motion randomly generated within a 4mm range, and applied using the Fourier shift theorem. The estimated motion parameters approximated well the ground truth values in the case of 1D translations, with clear improvements in the image quality after the applied motion correction. However, the algorithm struggled to estimate the motion parameters accurately around the first and last 10 lines of the k-space. We tested whether initiating our autofocusing algorithm from the central phase-encoding line would remove this effect and increase the correlation between the real and estimated motion parameters. The algorithm was shown to help reducing the strong ringing artifacts originating from 2D translational motion and to increase the correlation with the real motion parameters (from $r(198) = 0.63$ to $r(198) = 0.69$). However, the accuracy is again shown to drop at the beginning and towards the end of the acquisition: this behaviour was expected, as other autofocusing approaches have also found that the edges of k-space, which have lower signal and are dominated by noise, tend to provide less reliable motion estimates [62]. It is also possible that an error compensation parameter will improve the estimation accuracy and reduce the risk of error propagation, which is a known problem for autofocusing algorithms [40]. The results obtained are in line with other autofocusing motion correction methods in the literature, especially compared to Bydder et al. (2003) [27], where the algorithm was successfully tested on 2D translational motion. However, the magnitude of the simulated motion applied to our images has a much higher magnitude compared to [27]. Future studies will try the algorithm in presence of less rough motion parameters, which might

resemble real motion parameters more.

The algorithm struggled to estimate the motion parameters correctly in the case of in-plane rotations and translations. The current implementation tries to estimate the motion parameters by iteratively rotating the measured line until the MSE between the rotated line and the predicted one is minimized. However, points in k-space might not be linearly sampled due to the pie-slice effect caused by the rotational motion. Comparing the two lines is therefore not possible as the rotated line might have points in a different location in k-space. This problem would appear also trying to rotate the predicted line to minimise the cost-function, as it won't be possible to compare it with the measured line. In Cordero-Grande et al. [62], distributed and incoherent sampling improves the motion sensitivity, provided a certain degree of redundancy, during the reconstruction. A similar approach could be tested in our study: one possible solution could be to apply the GRAPPA operator gridding (GROG) [75] to convert non-Cartesian to Cartesian data.

Moreover, it is not as easy to write a simple and efficient cost function for rotations as for translations: while translations can be expressed with a single cost function line, given by the Fourier shift theorem, rotations need much more complicated functions, due to regridding. Translational motion is estimated after interpolating the rotated k-space back into a Cartesian grid: if this latter step is not performed accurately, the translations also will not be estimated correctly, due to strong Nyquist violations.

Eddy *et al.* [69] showed that 2D rotations could be approximated by three consecutive shears, without need for regridding. However, this method did not produce an accurate estimation of rotational motion parameters either: although shears are computationally less expensive than regridding, the current system does not seem to be able to find a global minimum of the cost function value to precisely estimate the true motion parameters. On the other hand, translations were well estimated, presumably as a result of this approach avoiding the interpolation step which we suspect caused the problems in the previous experiment.

It is also possible that a different cost function would provide a better assessment of the image quality throughout the optimization step; the GE metric showed a strong correlation with radiographers' scores when used for the autocorrection of MR images of the shoulder [41] and was successfully adopted to correct for bulk motion affecting brain MR images [39]. However, the GE value is estimated from the entire 2D slice in the image domain, unlike the proposed autofocusing method where the cost function is minimized for each phase encoding step in the Fourier space. To adopt this metric, it might be necessary to update the entire Fourier matrix for each optimization cycle, causing the algorithm to be significantly more computationally demanding.

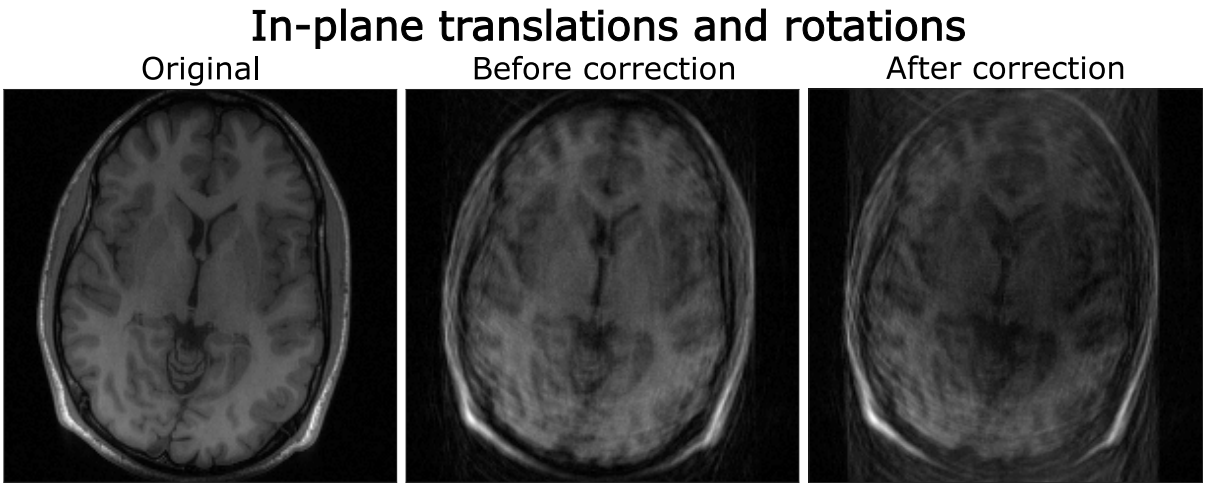

Figure 2.4.1: Comparison between the original (no motion), before and after the correction of a in-plane translations and rotations: the artifacts were not successfully compensated as the autocorrection did not estimate the motion parameters correctly.

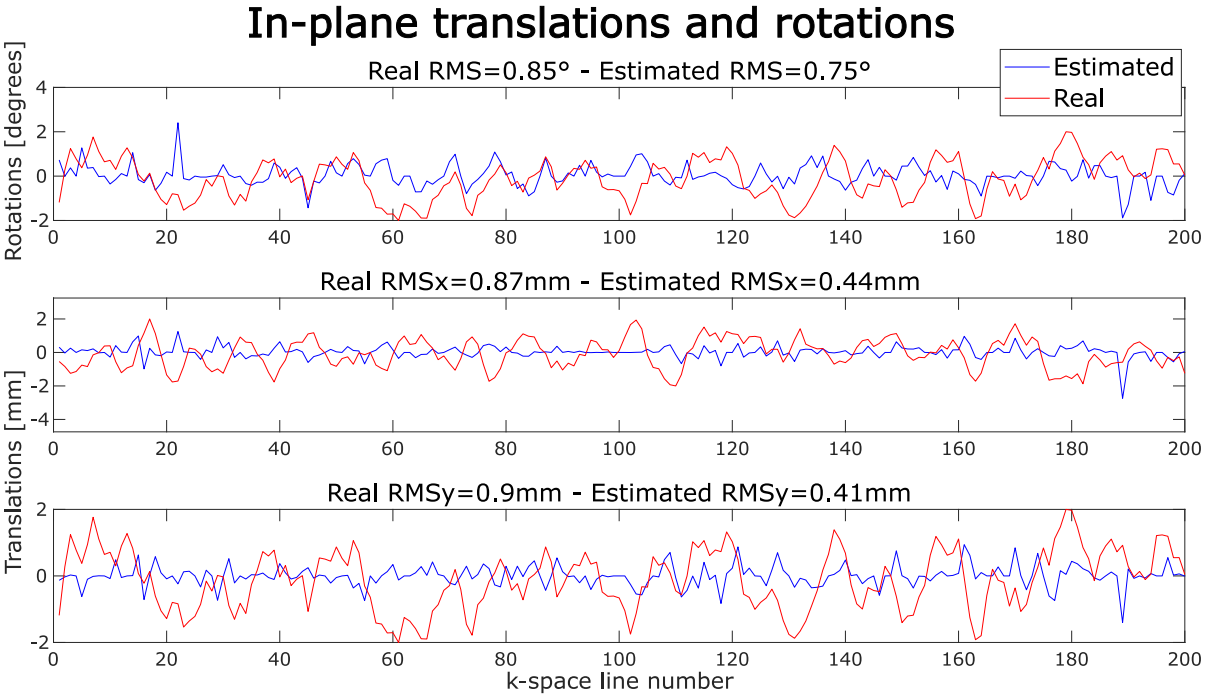

Figure 2.4.2: Comparison between the real rotational and translational motion parameters (red line) and the ones estimated by the algorithm (blue line). RMS values for the real and estimated motion parameters are reported on top of each motion trace. The motion parameters were not correctly estimated by the algorithm both in case of translations and rotations.

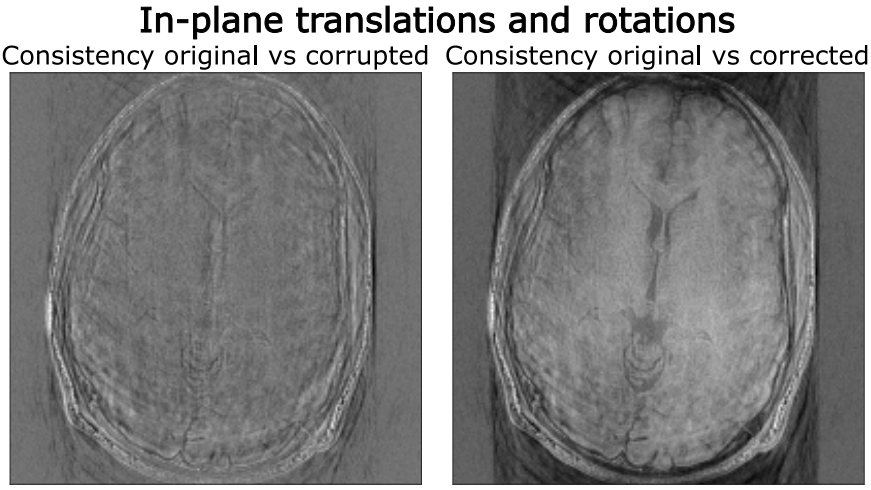

Figure 2.4.3: Comparison between the consistency calculated between the original and the image corrupted by in-plane translations and rotations ("original vs corrupted") and between the original and the image after applying the autofocusing correction ("original vs corrected"). After motion correction, the image shows more discrepancies with the original image than the uncorrected one (original vs corrupted case).

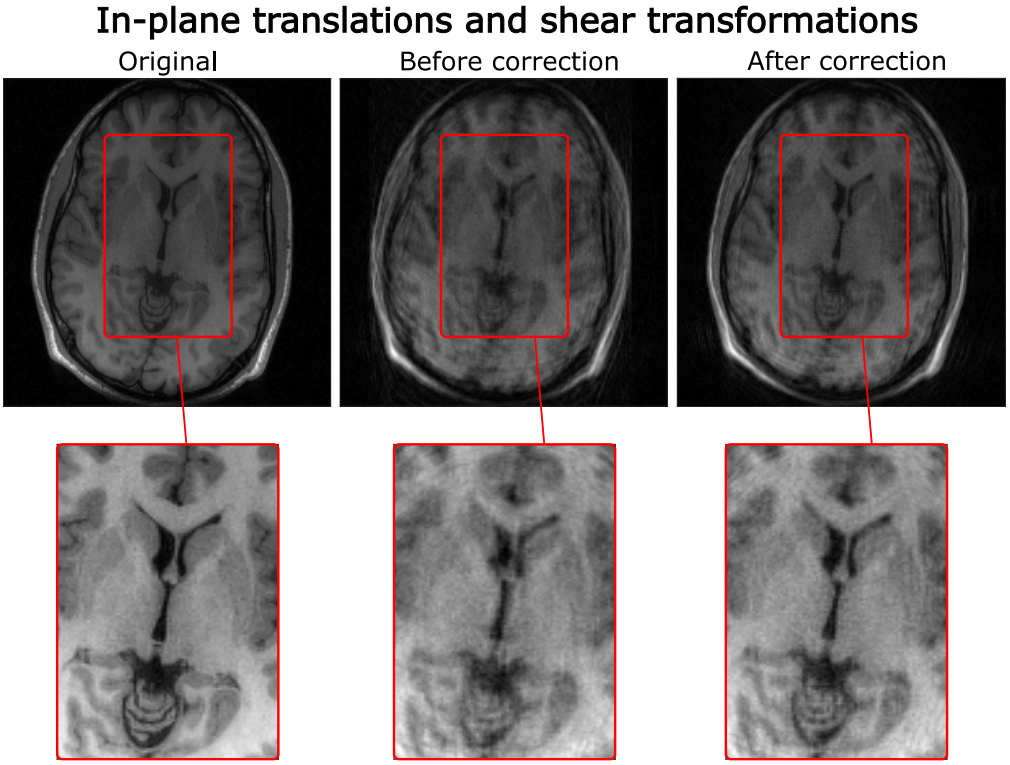

Figure 2.4.4: Comparison between the original (no motion), before and after the correction of a in-plane translations and rotations by shear transformations. The image sharpness improved after the autocorrection, as displayed in the magnified sections (red frames).

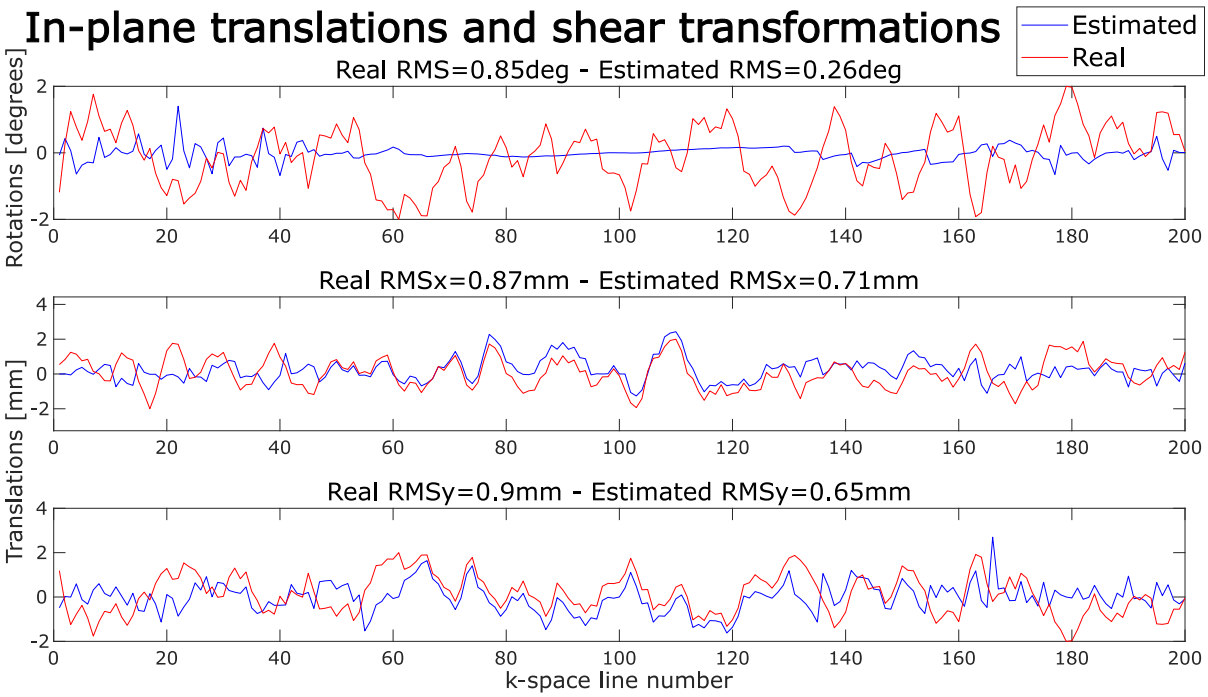

Figure 2.4.5: Comparison between the real 2D translations and rotations by shear transformations (red line) and the ones estimated by the algorithm (blue line). RMS values for the real and estimated motion parameters are reported on top of each motion trace. The algorithm estimated the translational motion correctly around the central k-space lines. However, the rotations were not successfully estimated using shear transformations.

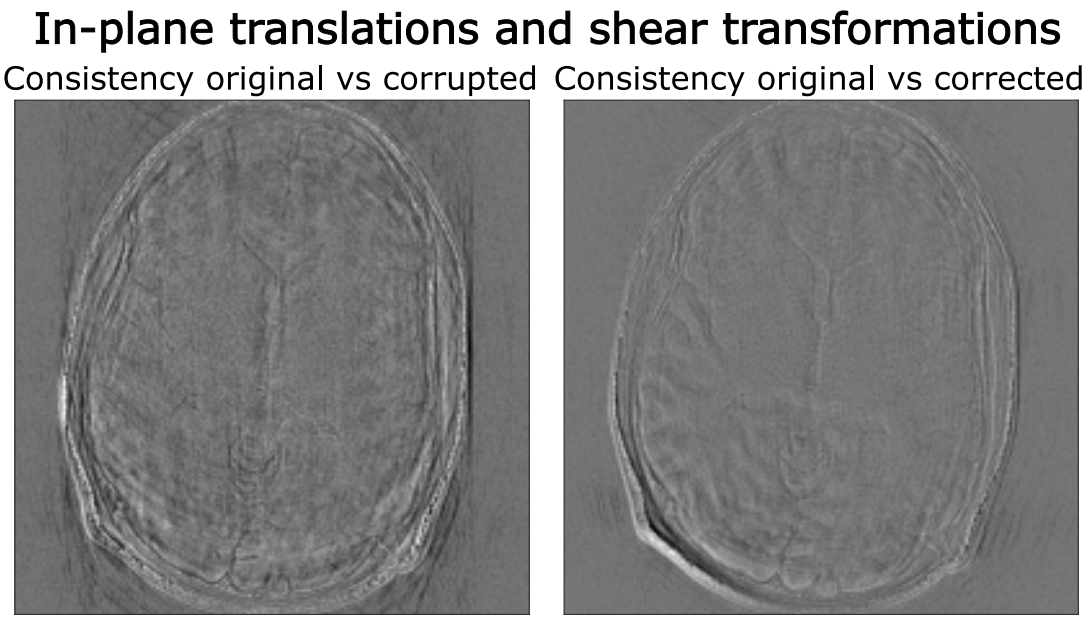

Figure 2.4.6: Comparison between the consistency calculated between the original and the image corrupted by in-plane translations and rotations by shear transformations ("original vs corrupted") and between the original and the image after applying the autofocusing correction ("original vs corrected"). The discrepancy with the original image decreased after the motion correction, compared to the uncorrected image.

2.5 Further comment

This work was performed during the early stage of my PhD. Despite showing some promising results in presence of translational motion, the algorithm was not working as good as hoped for in presence of rotations. Therefore, it was decided to focus on the next experimental steps of my work, with the intention of investigate the problem more in the future.

CHAPTER 3

Analysis of FatNav motion parameters estimation accuracy in 3D brain images acquired at 3T

Based on:

Elisa Marchetto, Kevin Murphy, Daniel Gallichan, *Comprehensive Analysis of FatNav Motion Parameters Estimation Accuracy in 3D Brain Images Acquired at 3T*, ISMRM 29th Annual Meeting, 2021.

Elisa Marchetto, Kevin Murphy, Daniel Gallichan, *Analysis of FatNav Motion Parameters Estimation Accuracy in 3D Brain Image*, Post Graduate Virtual Meeting 2021, 2021.

3.1 Introduction

A retrospective motion correction technique for brain MR images has been proposed by Gallichan *et al.* [44] to detect and correct non-deliberate motion during high resolution imaging. The idea consists of applying a 3D GRE sequence combined with a three-pulse fat-selective binomial excitation as navigator. Because of the natural sparsity of fat images, it is possible to apply the *GRAPPA* [16] parallel imaging technique to acquire exceptionally highly accelerated fat-volumes as navigators (*FatNavs*): in this way small motion can be detected and corrected. The *acceleration factor* (R) defines the amount of k-space data collected during the FatNavs acquisition: the higher the acceleration factor, the faster the acquisition would be. An acceleration of 4x4 (corresponding to R = 16) denotes that one sample in k-space is acquired every 4 lines in the phase and partition encoding directions. To reconstruct the missing lines, GRAPPA uses the ACS lines, which constitute the fully-sampled central region of a FatNav's volume collected prior to or during the main acquisition, with only

a few seconds added to the scan total duration time [44]. An example of a FatNav volume before and after GRAPPA reconstruction (acquired at 4 mm isotropic resolution and $R = 16$) is shown in Figure 3.1.1. The FatNav motion correction technique has been used to improve

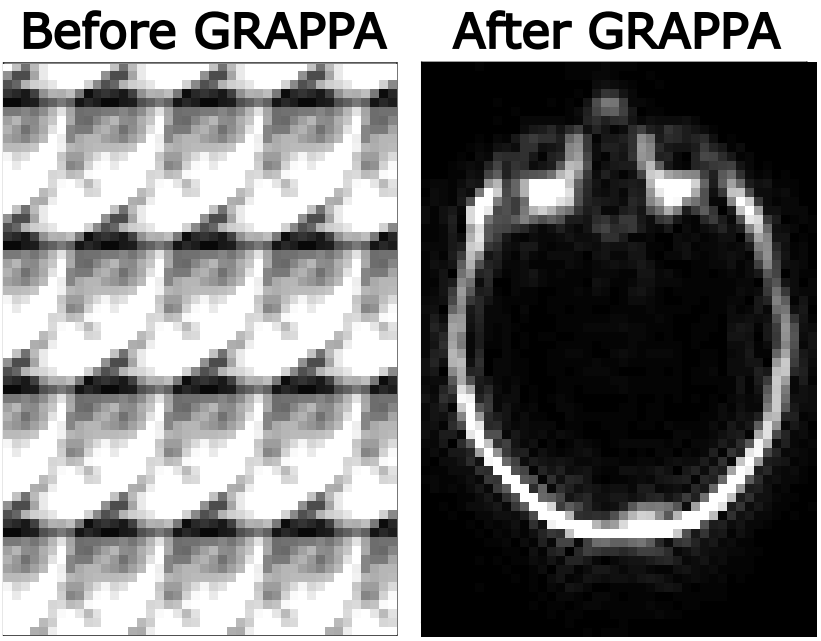

Figure 3.1.1: FatNav volume at 4 mm isotropic resolution acquired with an acceleration factor $R = 16$: before the GRAPPA reconstruction, the image obtained via the iFFT shows extensive aliasing artifacts caused by the missing lines in k-space, which are completely removed after GRAPPA.

the image quality in MR images of the brain affected by non-deliberate motion [44], [46] and by small deliberate motion [45]. However, GRAPPA reconstruction is not expected to perform well on FatNav volumes in the presence of strong head position changes. This is caused by mismatched calibration data acquired once at the start of the scan and the data for each individual FatNav volume being reconstructed: if the head position has changed substantially, then the GRAPPA calibration may be sub-optimal and affect the quality of the image reconstruction. The compromised GRAPPA reconstruction is then expected to lead to motion-parameter misestimation.

This study aims to assess FatNav accuracy in the presence of large changes in the head position, analysing the relationship between the extent of the motion and the expected degradation in image quality. This was performed by simulating a broad range of motion scenarios on FatNav' volumes previously acquired, to analyse the effect on the motion estimation accuracy in relation to the GRAPPA reconstruction. The results were used to derive empirical limits of the motion that FatNav can compensate to produce an artifact-free image.

3.2 Methods

3.2.1 Data acquisition

Five different datasets of MPRAGE brain MR images were acquired on a Prisma scanner (Siemens Healthcare, Erlangen, Germany) at 1 mm isotropic resolution, with TI/TE/TR = 1100/3.03/2410 ms and FA = 8°, using a 64-channel head coil. Two of the five datasets were acquired with deliberate motion, while the other three datasets were acquired without. Following each MPRAGE readout, a 3D FatNav volumes at 4 mm isotropic resolution was acquired as navigator, with TE/TR = 1.43/3.4 ms (TA = 0.37 s), for a total scanning time of 5:38 min.

3.2.2 B_1 maps

A fully-sampled FatNav volume acquired at the beginning of the scan was used to derive the ACS lines necessary for the FatNavs reconstruction. The ACS data was then filtered using an anti-aliasing Tukey window and extended to the entire FOV, using the zero-filling method. A pre-reconstructed FatNav volume was generated by applying the iFFT to the filtered ACS data and then processed using a 3D Hamming window to remove *ringing*, also known as *Gibbs artifacts*. B_1 maps were calculated as the ratio between each coil channel's pre-reconstructed FatNav volume and the sum-of-squares of all channels' volumes. The maps were then smoothed using *smoothn* [76], [77] function to ensure overall smoothness of the coil sensitivity maps (Figure 3.2.1). Figure 3.2.2 summarize all the steps performed to calculate the B_1 maps.

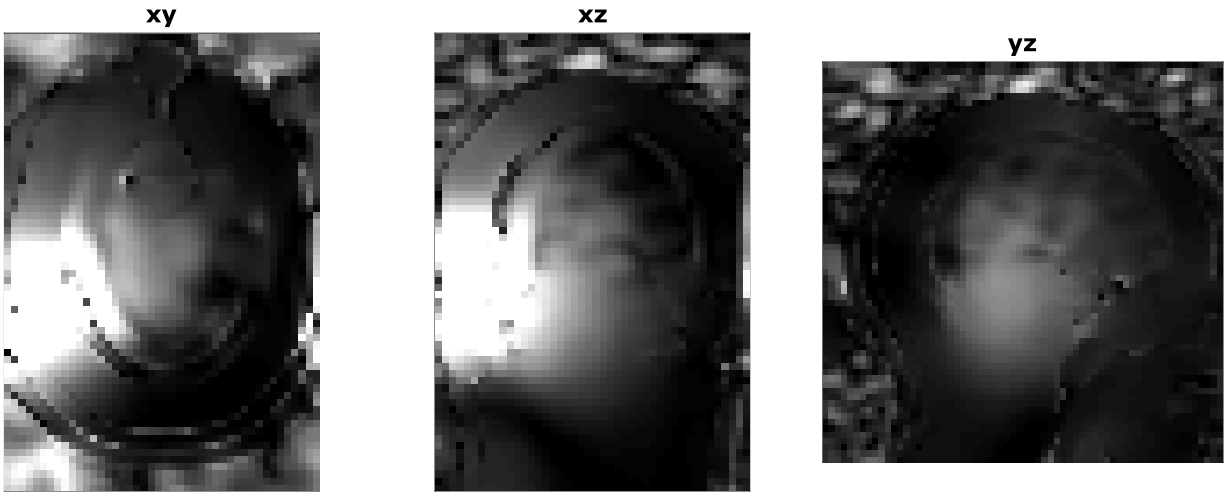

Figure 3.2.1: B_1 field maps of one channel calculated for one dataset. Maps were calculated for each channel of all the five datasets using the correspondent ACS lines acquired prior to the scan.

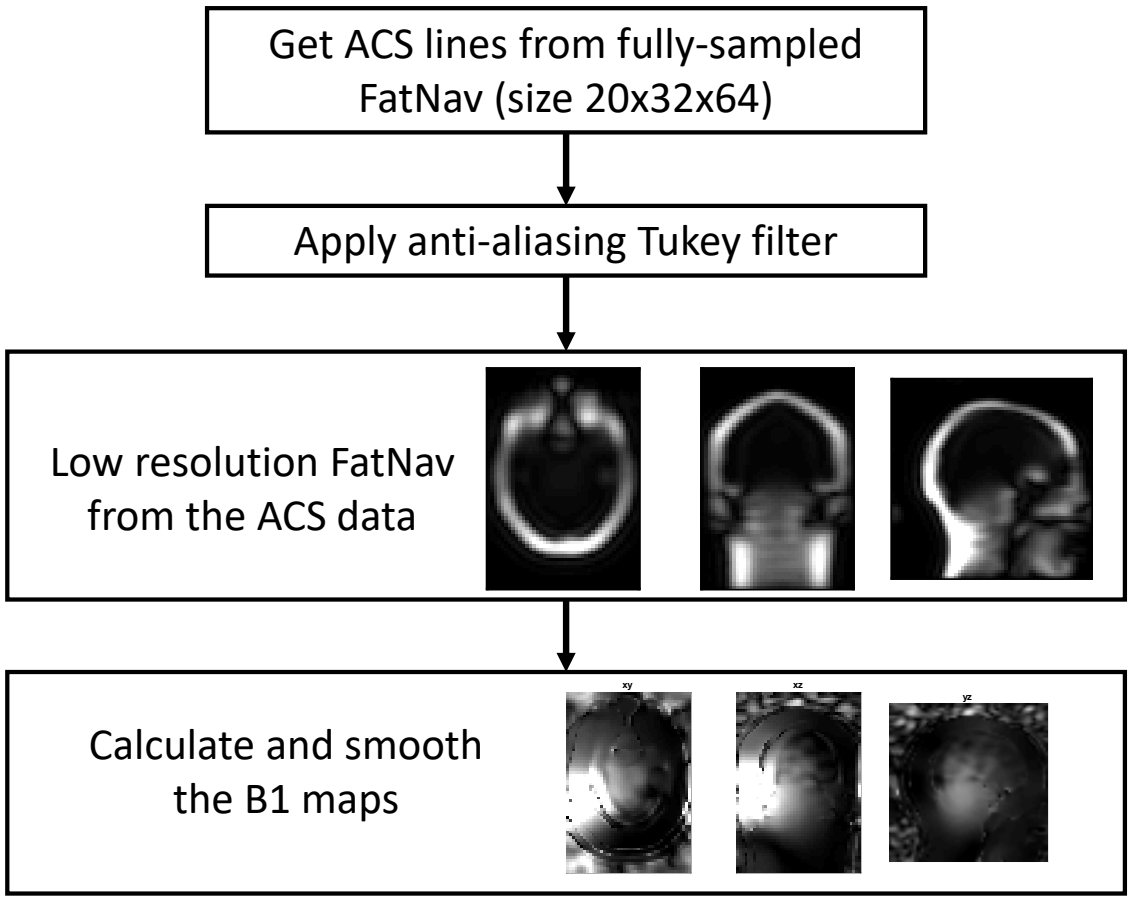

Figure 3.2.2: Schematic summary of the steps performed to estimate the B_1 maps: the ACS lines were obtained from the fully-sampled k-space centre of a FatNav volume acquired prior the scan; after applying an anti-aliasing Tukey filter, a low resolution FatNav volume was obtained from the ACS lines via a iFFT. To calculate the B_1 maps, the low resolution FatNav was divided by the sum-of-squares of all channels' coil volumes.

3.2.3 FatNav tracking accuracy

A high resolution FatNav volume was reconstructed using the GRAPPA parallel imaging technique for each dataset (Figure 3.2.3). Different combinations of motion parameters were applied to the high resolution FatNav volumes in the image domain, using the SPM realign tool [78]. Rotational and translational motion parameters were generated by selecting rotations ranging between 0 to 20° with increments of 5°, while translations were selected from a range up to 40 mm with 10 mm steps. Displacement along the z-direction was also applied in the negative sense (corresponding to movement towards the feet) as realistically the achievable motion along the superior/inferior direction is strongly restricted due to the presence of the head coil. Translations and rotations were considered symmetrical in all the other dimensions. These modified FatNavs were multiplied by the B_1 maps previously calculated and undersampled using an acceleration factor $R = 16$ to simulate the raw data for each coil's channel. Each volume was then re-reconstructed using GRAPPA to simulate the

final corrupted FatNav volume. A comparison between the modified and the corrupted FatNavs was performed to analyse the extent of the GRAPPA corruption. A total of 225 corrupted

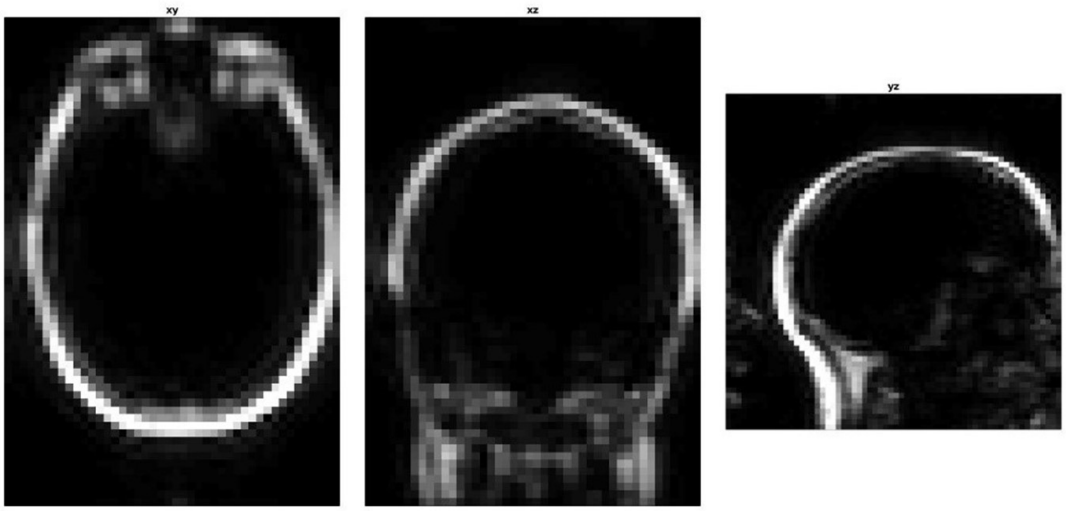

Figure 3.2.3: FatNav volume at 4 mm resolution generated after GRAPPA reconstruction for one dataset.

FatNav volumes were generated for each acquired dataset. Corrupted and reference FatNav's volumes were co-registered using SPM to obtain an estimation of the motion parameters. This was then compared to the real motion applied to find the mis-estimation caused by the GRAPPA inconsistency. The result was averaged between datasets for the full range of parameters considered. The *residual motion* could be therefore estimated from any given *true motion* using linear interpolation on the FatNav tracking accuracy data, where the residual motion represented the apparent head motion after FatNav correction. Figure 3.2.4 shows a schematic representation of the steps to obtain the corrupted FatNav and the residual motion parameters forming the FatNav tracking accuracy.

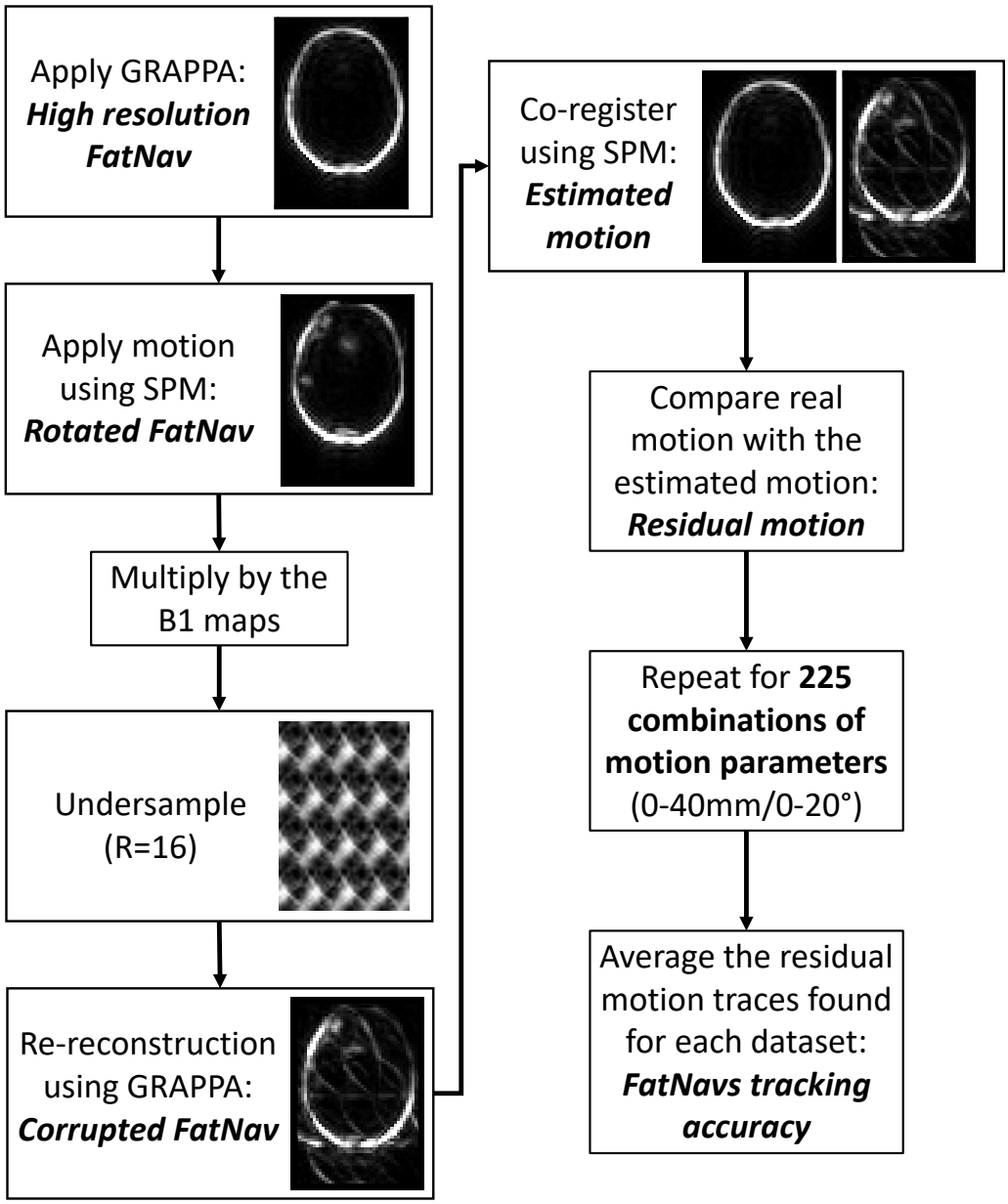

Figure 3.2.4: Schematic representation of the process performed to calculate the FatNav tracking accuracy for 225 different combinations of motion parameters (ranged between 0-40 mm translations and 0-20° rotations). One set of 6 motion parameters were applied to the high resolution FatNav (obtained via GRAPPA reconstruction) using SPM. The rotated FatNav was then multiplied by the B_1 maps to find the rotated volume for each coil. Each volume was then undersampled using an acceleration factor of $R = 16$ (4x4) and re-reconstructed using GRAPPA to simulate the final corrupted FatNav if head motion occurred during the scan. By co-registering the initial high resolution volume and the corrupted FatNav it was possible to find the estimated motion parameters if FatNavs were used. These motion parameters were compared to the real motion parameters applied to find the residual motion (or estimation error). The same steps were repeated for all motion traces for each dataset. The residual motion was then averaged across the three datasets to find the FatNav tracking accuracy, from which it was possible to estimate the residual motion from any new motion trace via linear interpolation.

3.2.4 MPRAGE EXPERIMENT

In this study, different combinations of true motion curves were randomly generated using a "value" noise version of the original *Perlin noise* [73, 74]. The function used is available in the retroMoCobox toolbox [70] and it requires the number of motion parameters to be generated and a weighting factor. The function generates multiple arrays of numbers at different frequency and amplitude using a cubic interpolation function and smoothed using the weighting factor. The function then sums all these randomly generated array to produce the final Perlin noise. In this work, we generated two different types of motion can be generated, which we have chosen to refer to as *smooth* and *rough* motion. Rough motion (weighting factor of 1) is generated by rapid and abrupt changes in head position, occurring for a prolonged period, while smooth motion is characterized by slow changes in the head position. To generate smooth motion, a weighting array of [1 3 9 27 81 243 729 2187 6561] was used, as the function gets iteratively smoothed more as the frequency increases. Examples of motion traces for rough and smooth motion are reported in Figure 3.2.5 and 3.2.6 respectively.

96 different combinations of motion parameters were randomly generated for smooth and rough types of motion with RMS values ranging between 0-20° and 0-40 mm for rotations and translations respectively, generating 192 combinations for each of the three datasets for a total of 576 motion curves. Motion occurring in the centre of the k-space has more

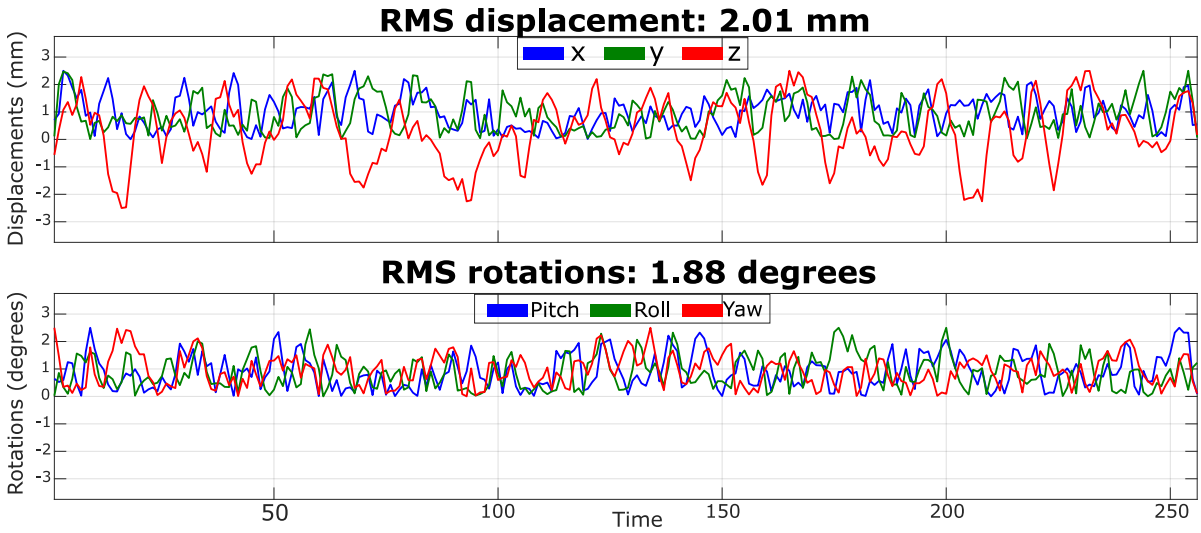

Figure 3.2.5: Example of rough motion parameters randomly generated with RMS = 2.01 mm and RMS = 1.88° for translations and rotations respectively.

impact on the final image than motion occurring at the edges due to the different types of information encoded in the k-space: the k-space's centre contains low frequency information related with the contrast and shape of the image, while edges and details are encoded in the high spatial frequencies' information at the k-space periphery [9]. To take this into account,

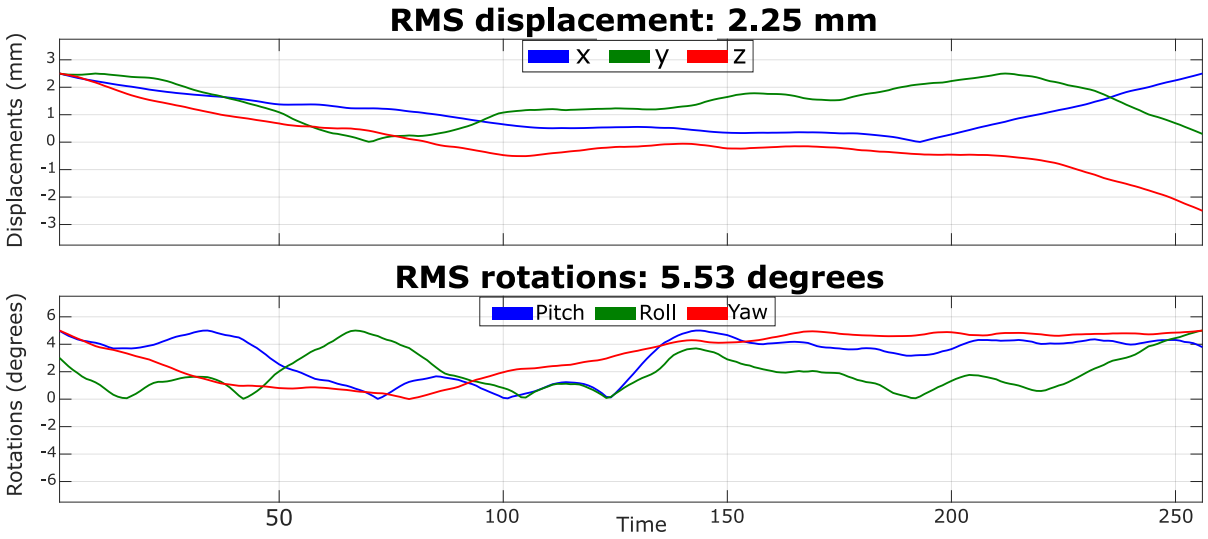

Figure 3.2.6: Example of smooth motion parameters randomly generated with RMS = 2.25 mm and RMS = 5.53° for translations and rotations respectively.

the motion parameters were randomly generated four times for each range of motion: the motion distribution was then expected to vary during each repetition, but with little changes in the RMS value.

The motion parameters previously applied to the FatNav's volumes (Figure 3.2.4) were used as sample points for a linear interpolation function (MATLAB function *griddata*), and the correspondent residual motion as sample values; by feeding the interpolation function with the new motion parameters generated using the Perlin noise, it was possible to estimate the expected residual motion if FatNavs were used for translations and rotations separately. The corresponding residual motion was applied to the original MPRAGE images acquired without voluntary motion using the retroMoCoBox toolbox [70], simulating the predicted residual degradation in image quality that would be expected if FatNavs had been used to correct motion of this type.

3.2.5 Image quality assessment

Image quality evaluation was initially performed using the *GE* metric, which has been found by McGee *et al.* as the best metric for autocorrection of MR images of the shoulder, as the metric closely correlated with observers' evaluations [40]. In this study, the GE was calculated as shown in Eq. 3.1: the gradient magnitude was found as the square root of the sum-of-squares of the gradients along x and y (G_x and G_y), which were estimated using the MATLAB function *imfilter*, while d_x and d_y represent the Prewitt operators used to calculate the two gradients via a convolution (*conv* specification) step. The entropy of the gradient

magnitude was determined using the *entropy* MATLAB function.

$$\begin{aligned} d_x &= \begin{bmatrix} 1 & -1; 1 & -1; 1 & -1 \end{bmatrix} \\ d_y &= d_x' \\ G_x &= imfilter(image, d_x, \text{"}conv\text{"}) \\ G_y &= imfilter(image, d_y, \text{"}conv\text{"}) \\ G &= \sqrt{G_x^2 + G_y^2} \\ H &= entropy(G) \end{aligned} \tag{3.1}$$

Two observers, non-clinicians and with 15- and 3- years' experience in brain MRI, evaluated the 192 MPRAGE images generated for each of the three datasets, acquired without deliberate motion, using a Graphical User Interface (GUI) created in MATLAB: the image was displayed on the screen with no information regarding the GE value or the other observer's evaluation; the observer scored each image with a scale from 4 to 1, with 4 = no visible motion artifacts, 3 = some motion artifacts, 2 = strong motion artifacts and 1 = severe motion artifacts. A graphical scheme of this process (together with an example for a set of smooth motion parameters) is reported in Figure 3.2.7.

3.2.6 Statistical analysis

Next sections briefly describe the statistical tests performed in this study. A summary is reported in Table 3.1, together with the MATLAB functions used.

3.2.6.1 Inter-observer variability

The inter-observer variability was measured using the Krippendorff's Alpha coefficient [79], which is a statistical measure developed to calculate the agreement among observers. The function *kriAlpha* [80] was used in MATLAB to estimate the coefficient.

3.2.6.2 Multinomial logistic regression

A multinomial logistic regression was performed revealing how the probability of falling in an evaluation category (4 to 1) would change based on the GE values [81]: the probability to fall into categories representing good quality images (namely categories 4 and 3) was expected to be inversely proportional to the GE value. The multinomial logistic regression was performed using the *mnrfit* function, followed by a one-way ANOVA test (MATLAB function *anova1*).

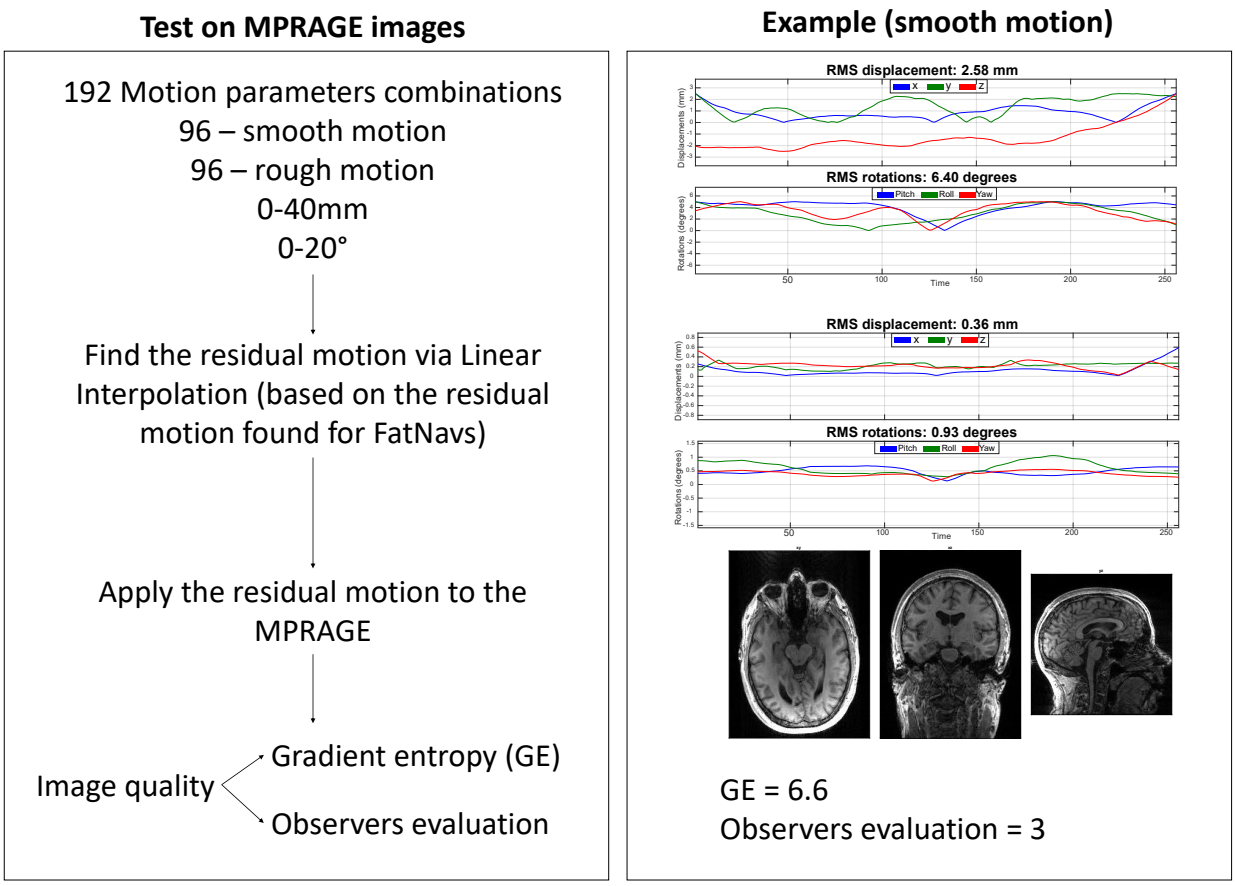

Figure 3.2.7: Summary of the process used to test the FatNav tracking accuracy on MPRAGE images, together with an example for a set of smooth motion parameters. A total of 192 motion traces were generated, 96 for smooth motion and 96 for rough motion, within a range of 0-40 mm translations and 0-20° rotations. For each motion trace, the residual motion was found via linear interpolation of the FatNav motion accuracy previously found (Figure 3.2.4). The residual motion was then applied to the motion-free MPRAGE volume. The image quality assessment was performed using the GE metric and evaluation from an observer using a scale between 1 to 4, with 4 denoting no visible motion artifacts.

3.2.6.3 Linear regression between RMS and GE

The relationship between the motion occurred and the GE was investigated using the linear model shown in Eq. 3.2: the output variable Y represented the GE, while X_1, X_2 described the rotational and translation motion with their respective parameters a and b; an interaction term was also added to the model, to describe the mutual effect that rotations and translations (independent variables) might have on the outcome.

$$Y = 1 + a \cdot X_1 + b \cdot X_2 + c \cdot X_1 \cdot X_2 \tag{3.2}$$

The function *fitlm* was used to produce a linear regression model based on the motion magnitude and the GE values, to find the coefficients fitting the linear model. The *step* function allowed to test whether the presence of the interaction term significantly improved the linear regression model based on the Bayesian Information Criterion (BIC) [82]: the model with lowest BIC value was selected as best fitting model. The motion magnitude was calculated for rotational and translational motion separately as the RMS value along each direction, and averaged across datasets. The model was used to assess at which range of motion the algorithm still worked correctly and find the motion threshold between each evaluation's category. This was performed by selecting the GE values at the interceptions between each category boundary, found via the multinomial logistic regression previously performed. It was possible to estimate the rotational or translational motion corresponding to the entropy value by placing the other to zero. The level of motion corresponding to each category boundary was evaluated twice: once assuming that the simulated motion was the true motion (i.e no FatNav correction applied) and once assuming that the simulated motion was the residual motion following FatNav correction. This allows a comparison of the expected increase in motion that can be tolerated when FatNav correction is used.

3.2.6.4 Linear and non-linear regression between FD and GE

Although the RMS of rotations and translations provides information regarding the magnitude of the motion occurred, it cannot effectively compare the motion estimation accuracy in the case of smooth vs rough motion, as smooth and rough motion profiles with similar RMS values are expected to have quite a different level of impact on the amount of motion-artifacts in the resulting image.

In this study, the *Framewise Displacement (FD)* was adopted as a single-value metric to measure the head motion between consecutive volumes. It was calculated as the sum of the absolute values of the derivatives of the six realign parameters, where rotations were estimated as the displacement occurring on the surface of a sphere of 50 mm radius [83]. The relationship between the mean FD (averaged across the entire acquisition) and the GE was investigated using a linear and a non-linear regression model. For the latter, a logarithmic model was chosen due to the entropy being based on the log-function (Eq. 3.3). The information derived from the two models was then used to estimate the FD values that correspond to the boundaries between the 4 coarse categories from the human evaluation of the images.

$$Y = a + b \cdot log(X) \tag{3.3}$$

Summary of the statistical tests		
Test	**Aim**	**Function (MATLAB)**
Inter-observer variability (*Krippendorff's alpha)*	Measure agreement among observers	*krialpha.m*
Multinomial logistic regression	Analyse relation between GE and the observers' evaluations	*mnrfit.m*
One-way ANOVA	Test the model found by the multinomial logistic regression	*anova1.m*
Linear regression between RMS and GE	Find image quality category boundaries based on RMS	*fitlm.m* *step.m*
Linear regression between FD and GE	Find image quality category boundaries based on FD	*fitlm.m*
Non-linear regression between FD and GE	Find image quality category boundaries based on FD	*fitnlm.m*

Table 3.1: Summary of all statistical tests performed in this study. The aim of each test is reported, as well as the MATLAB function used.

3.3 Results

3.3.1 GRAPPA motion robustness

Figure 3.3.1 compares FatNav volumes before (Pre-GRAPPA) and after GRAPPA (Post-GRAPPA) "re-reconstruction" step for four different levels of motion (low, medium, high and very high) randomly selected from the 225 different combinations of motion parameters applied to the acquired FatNavs. Pre-GRAPPA and Post-GRAPPA images correspond to the **Rotated FatNav** and the **Corrupted FatNav** shown in Figure 3.2.4. Parallel imaging artifacts were found to increase for larger changes in the head position compared to Pre-GRAPPA images, due to a more severe mismatch between the ACS lines for the GRAPPA reconstruction and the rotated FatNavs. To analyse the relation between the estimated (Pre-GRAPPA) and predicted (Post-GRAPPA) motion parameters, the Pearson's correlation coefficient was estimated using the Matlab function *corrcoef*. Figure 3.3.2 shows how the estimated coefficients change based on the rotational motion along the three axis: as expected, the correlation decreases as the motion increases.

3.3.2 Inter-observer variability

The Krippendorff's alpha values calculated between the two observers first evaluations (sample size of 192) were above 0.8 in all three datasets, denoting very high reliability between the

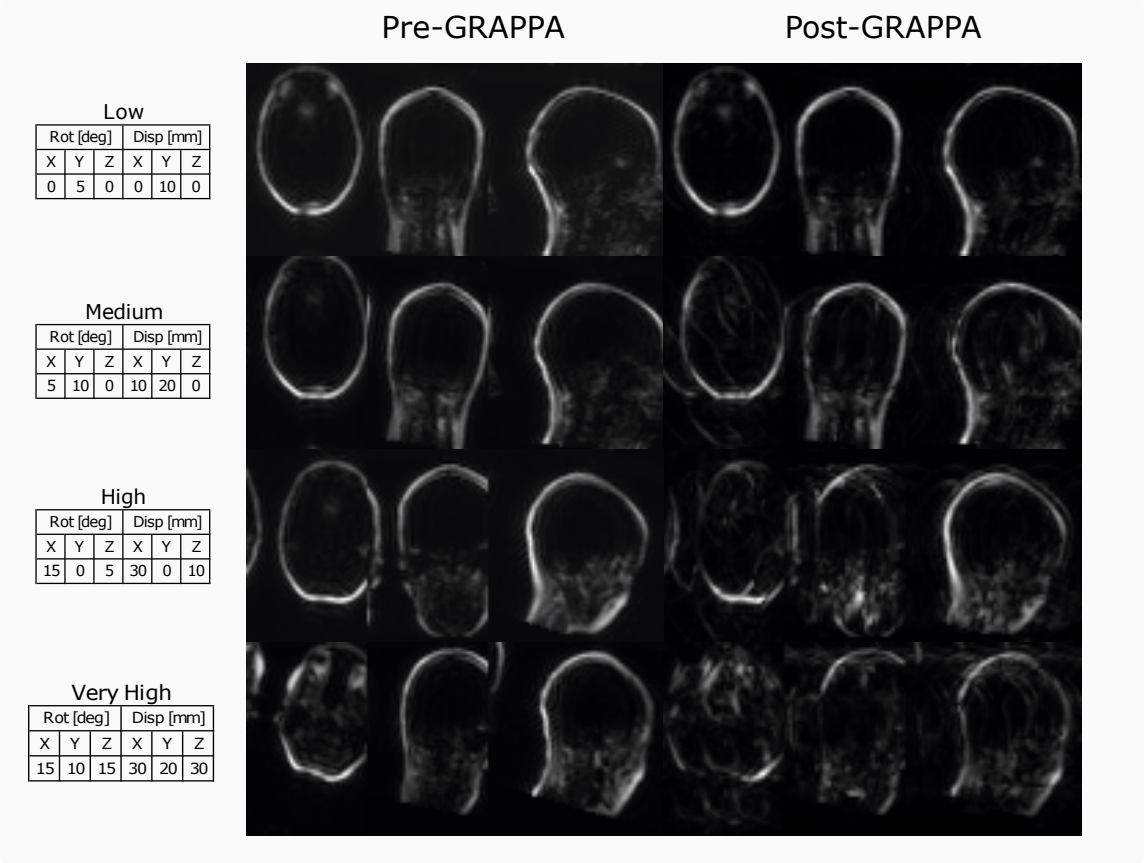

*Figure 3.3.1: Comparison between FatNav volume before and after GRAPPA "re-reconstruction", for four different levels of motion (tables on the left), to show the effect of mismatched ACS data to the FatNavs' volumes: parallel imaging artifacts are shown to increase with the amount of motion. The Pre-GRAPPA image represents the FatNav volume after applying the motion parameters using SPM (the **Rotated FatNav** in Figure 3.2.4). The Pre-GRAPPA image is then multiplied by the B_1 maps and undersampled using an acceleration factor $R = 16$. The Post-GRAPPA image is obtained by reconstructing the undersampled volume (the **Corrupted FatNav** in 3.2.4).*

two observers [79]. Values are reported in Table 3.2.

Krippendorff's alpha	
Dataset	Alpha value
Dataset 1	0.85
Dataset 2	0.87
Dataset 3	0.90

Table 3.2: Krippendorff's Alpha value calculated for the first observers' evaluations: all three values are close to 1, suggesting strong reliability.

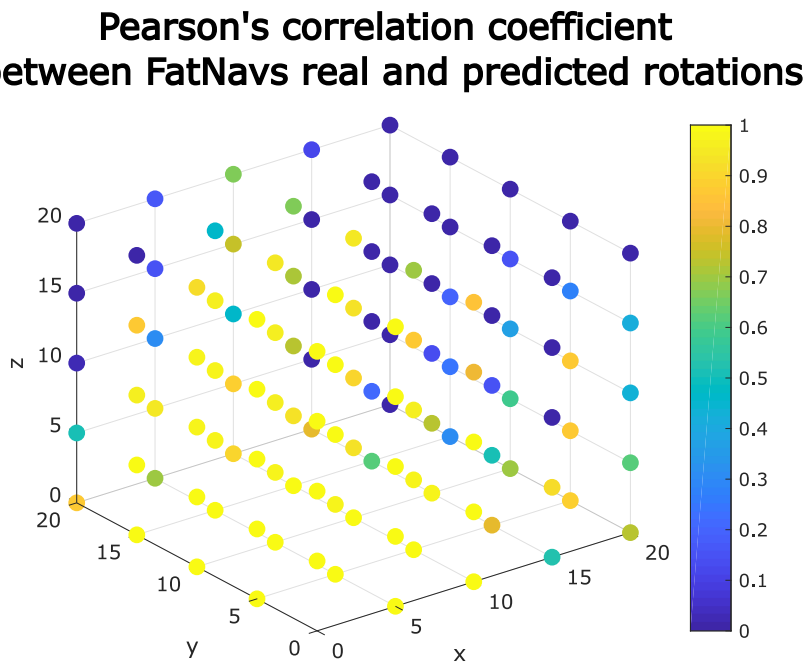

Figure 3.3.2: Pearson's coefficient values between real (Pre-GRAPPA) and predicted motion parameters (Post-GRAPPA). The color map represents the value of the correlation coefficient changing based on the amount of rotational motion occurring: as expected, the correlation decreases as the motion increases along the three axis.

3.3.3 Multinomial logistic regression

Figure 3.3.3 presents the results from the Multinomial logistic regression performed between the observers' evaluations and the image quality relative to each image. Each curve describes the changes in probability distribution based on the GE value among categories. As the GE value increases, the probability to fall into a category representing a low level of motion artifacts decreases, as expected. These results were further corroborated by the one-way ANOVA test, whose results are reported in Table 3.3.

3.3.4 Linear regression between RMS and GE

It was found that the relationship between rotational, translational motion and the gradient entropy could be described by the linear model defined in Eq. 3.2: the use of the interaction term resulted in a lower BIC score compared to the model without, confirming that the interaction term provided a better fit to the data. All the statistical parameter resulting from the linear regression test are reported in Table 3.4. The linear model was used to estimate the rotational and translational motion corresponding to the GE value found at categories' interceptions via the multinomial logistic regression. Figure 3.3.4 compares the image quality achieved by using FatNavs motion correction against no-motion correction: each coloured region bounds the rotational and translational motion parameters range for each

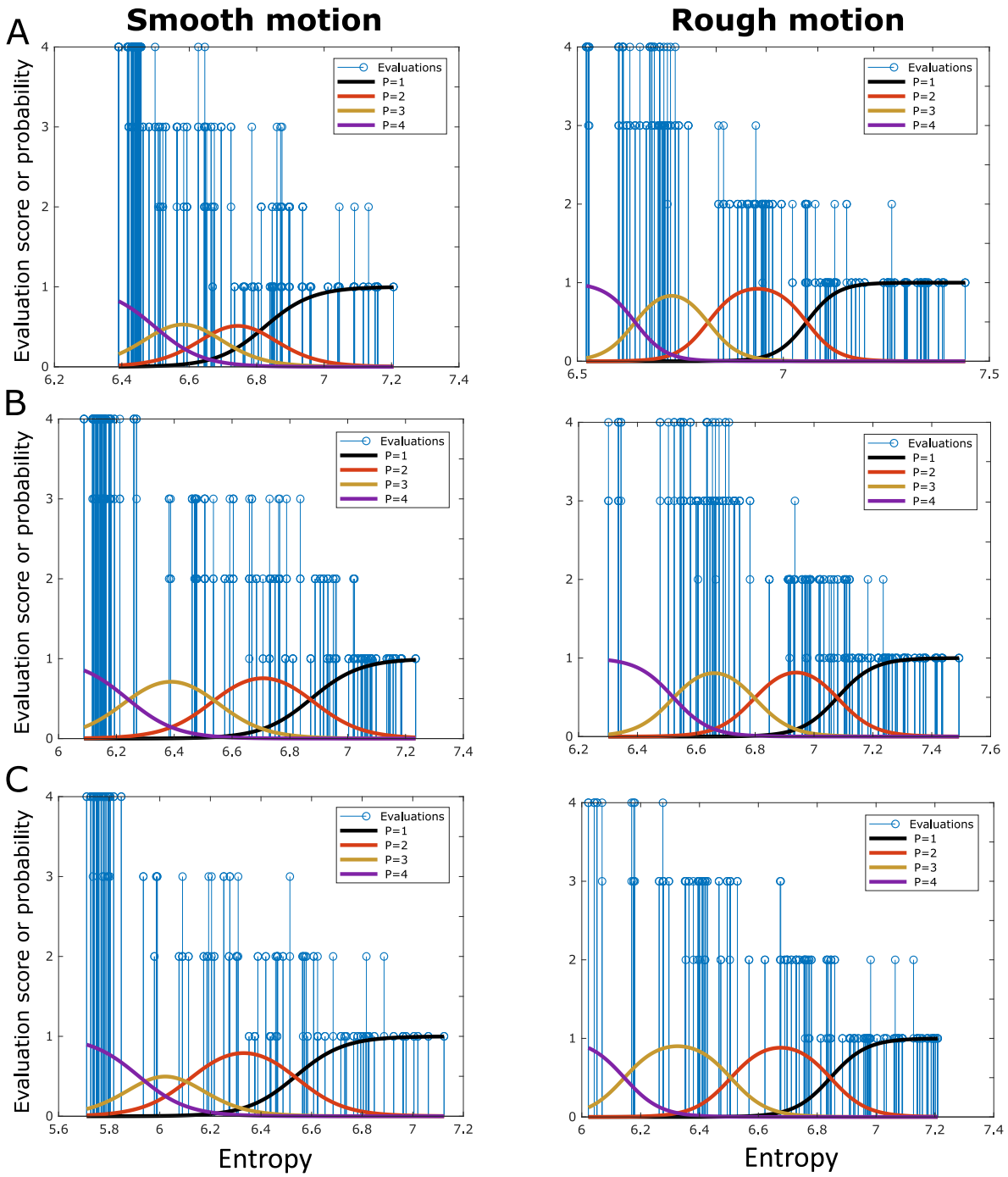

Figure 3.3.3: Multinomial Logistic Regression between image evaluations and the GE in case of smooth and rough motion for dataset (A) 1, (B) 2 and (C) 3. All evaluations, from 1 to 4, are plotted as blue vertical lines, while each coloured Gaussian waveform represents the probability of falling in one of the four evaluation's categories: category 4 (no visible artifacts) in purple, category 3 (some motion artifacts) in yellow, category 2 (strong motion artifacts) in orange and category 1 (severe motion artifacts) in black. Lower entropy values corresponded to higher category rating and, therefore, to a better image quality.

One-way ANOVA test			
Dataset	**Motion type**	**F-value (3,284)**	**p-value**
Dataset 1	Smooth motion	283.06	1.89e-69
	Rough motion	200.34	2.67e-58
Dataset 2	Smooth motion	563.71	3.11e-119
	Rough motion	787.49	2.89e-137
Dataset 3	Smooth motion	508.73	7.37e-114
	Rough motion	551.63	4.30e-188

Table 3.3: One-way ANOVA test results for dataset 1, 2 and 3: the mean value for each category is significantly different as corroborated by the p-values. This confirms the entropy being a significant factor on the probability of the evaluation to fall in a certain category.

Linear Regression model						
Dataset	**Motion**	**r-squared**	**F-value (4,92)**	**p-value**	**BIC with interaction term**	**BIC w/o interaction term**
Dataset 1	Smooth motion	0.77	103.29	2.39e-29	-106.76	-102.19
	Rough motion	0.87	215.95	1.63e-41	-168.00	-151.37
Dataset 2	Smooth motion	0.84	166.97	4.25e-37	-75.32	-57.59
	Rough motion	0.80	119.34	1.33e-31	-87.97	-65.44
Dataset 3	Smooth motion	0.83	152.67	1.34e-35	-40.63	-32.72
	Rough motion	0.81	137.65	6.76e-34	-84.90	-74.05

Table 3.4: Linear regression model statistical parameters for each dataset in case of smooth and rough motion; the F-values and related p-values, as well as the r-squared values, denote that the model selected adequately explains the data both in the case of smooth and rough motion; moreover, models with the interaction term (between rotations and translations) exhibit a lower BIC value compared to models without.

evaluation category with FatNav correction and without motion correction, in case of smooth and rough motion. FatNavs is shown to correct very well for a RMS value along the three axes of $\sim 3.7^\circ/3\,\text{mm}$ and $\sim 2^\circ/1.6\,\text{mm}$ for smooth and rough motion respectively (category 4 boundary), while motion parameters estimation accuracy drops above $\sim 5.3^\circ/4.6\,\text{mm}$ and $\sim 3.7^\circ/2.9\,\text{mm}$ (category 2 boundary). On the other hand, image quality falls much more

quickly without motion correction, where the category 2 boundary is set at $\sim 3.5°/2.5\,\text{mm}$ for smooth motion and $\sim 1°/0.6\,\text{mm}$ for rough motion. RMS values at each category boundary are reported in Table 3.5, for rotational and translational motion, with and without using FatNav motion correction: in presence of rough motion, it seems not possible to achieve a category 4 image quality (no visible artifacts) without FatNavs.

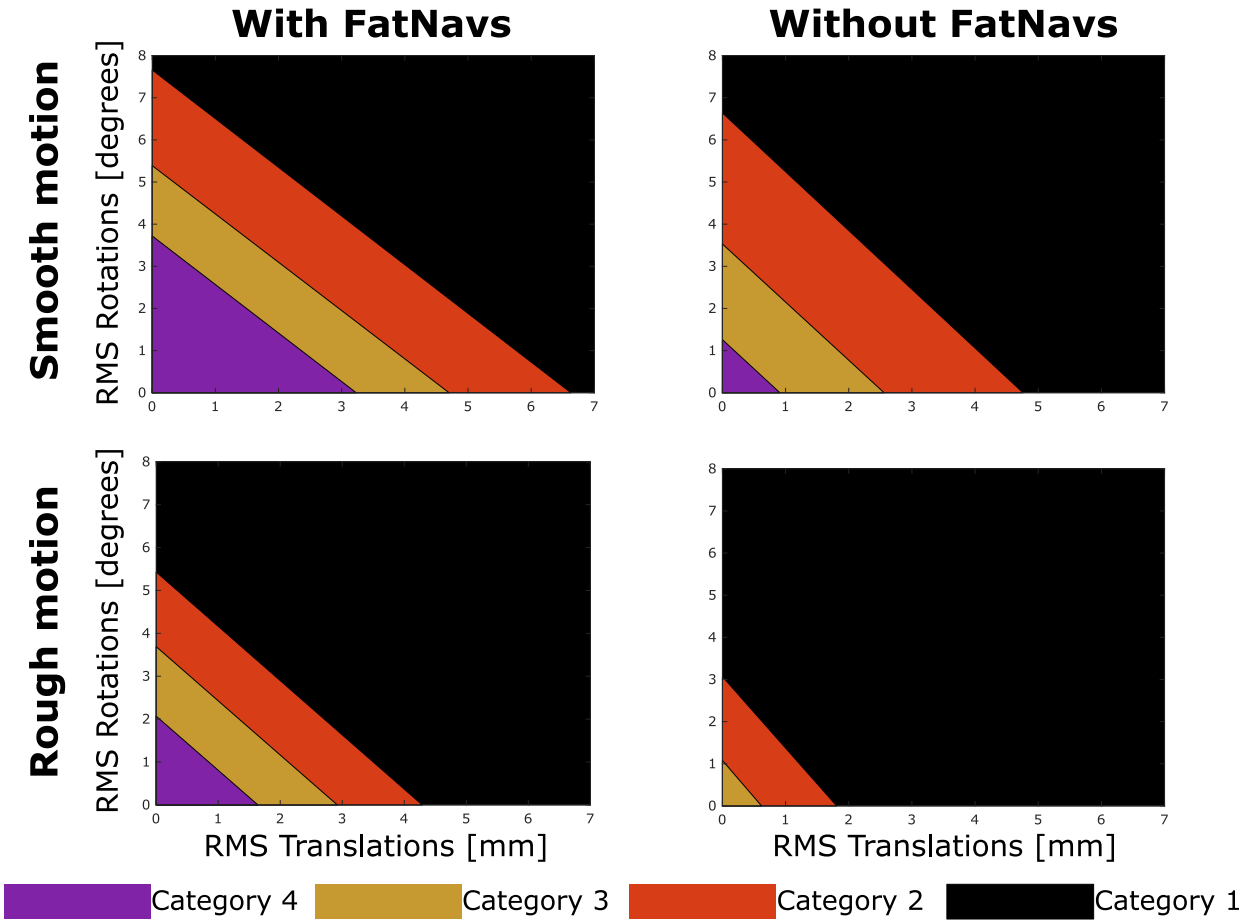

Figure 3.3.4: Motion level at each category boundary (as average across the three datasets) for smooth (A) and rough motion (B) in case of FatNav or without motion correction: FatNavs shows a high tolerance to motion, whereas the image quality decreases faster for images without motion correction.

3.3.5 Linear and non-linear regression between FD and GE

The relation between the mean FD and GE was investigated, comparing a linear and a logarithmic regression model. The two models are compared in Figure 3.3.5 and 3.3.6 for smooth and rough motion respectively. In case of smooth motion (Figure 3.3.5), the results are quite nuanced, with no model providing a clearly superior fitting compared to the other:

Category boundaries – RMS								
Category	**Smooth motion**				**Rough motion**			
	With FatNavs		**No motion correction**		**With FatNavs**		**No motion correction**	
Category 4 to 3	3.18 mm	3.67°	0.87 mm	1.21°	1.55 mm	1.97°	0 mm	0°
Category 3 to 2	4.63 mm	5.32°	2.48 mm	3.44°	2.71 mm	3.43°	0.47 mm	0.78°
Category 2 to 1	6.81 mm	7.83°	4.94 mm	6.85°	4.10 mm	5.19°	1.67 mm	2.81°

Table 3.5: Translational and rotational RMS values at each category boundary for smooth and rough motion if FatNav motion correction was used.

based on the r-squared value (0.91/0.88/0.87 and 0.76/0.90/0.86 for the linear and non-linear models respectively), the linear model is shown to describe the data better than the non-linear model in case of datasets 1 and 3. On the other hand, the non-linear model greatly improved the data fitting compared to the linear model in all three datasets, with r-squared values being 0.87/0.78/0.75 and 0.96/0.98/0.98 for the linear and non-linear model respectively. This denoted that although the linear regression model could potentially describe well both smooth and rough motion, the rough data was explained better by the non-linear model.
Linear and non-linear regression models were used to find the categories' boundaries based on the mean FD for smooth and rough motion respectively: if FatNavs were used, image quality degraded to a "strong motion artifacts" level (category 2) for FD values of 0.22 mm and 0.42 mm for smooth and rough motion respectively. The FD values for each category boundary are reported in Table 3.6.

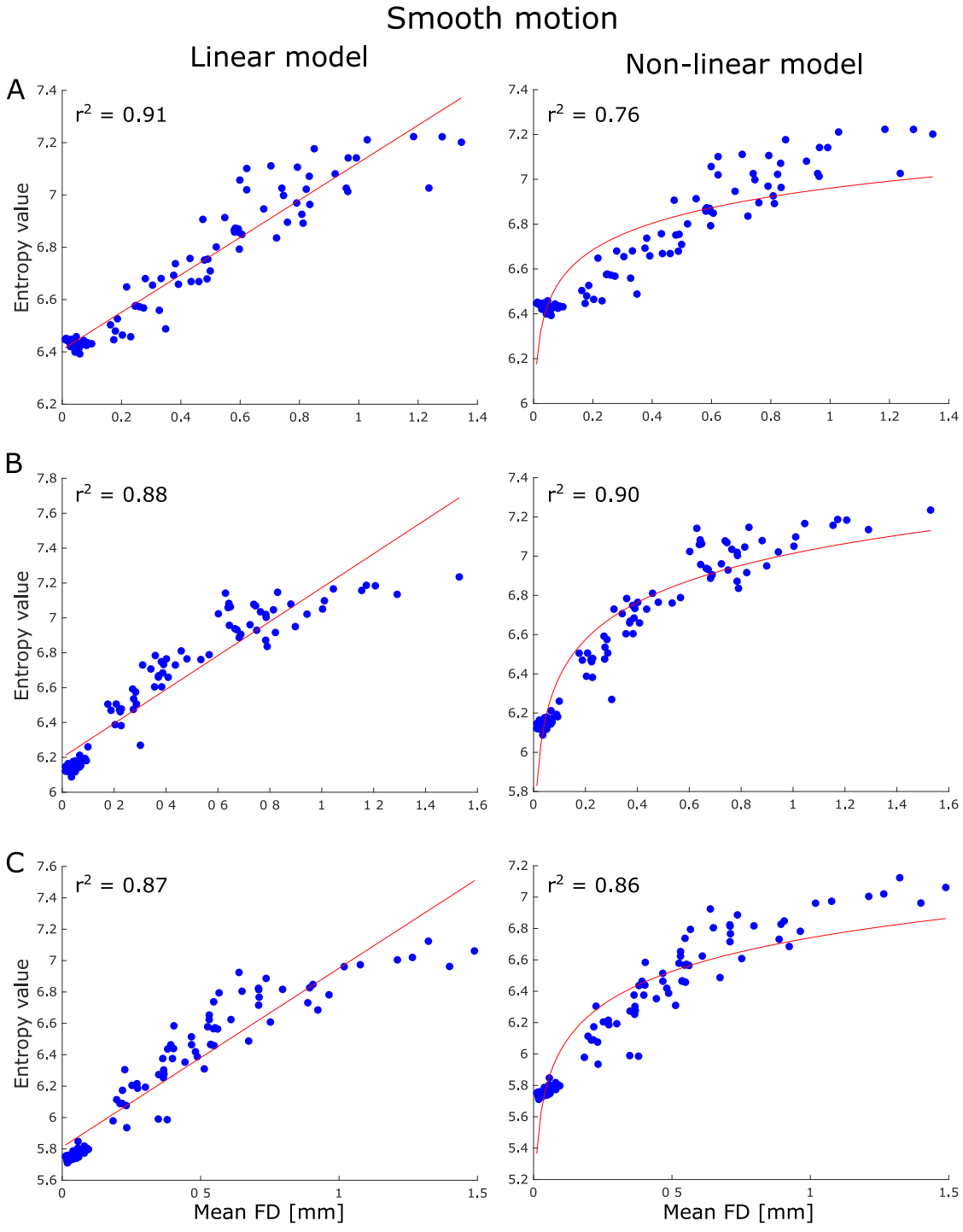

Figure 3.3.5: Comparison between linear and non-linear regression models in case of smooth motion for dataset (A) 1, (B) 2 and (C) 3: the linear model explained better the data in datasets 1 and 3. Relative r-squared (r^2) values are reported on each figure.

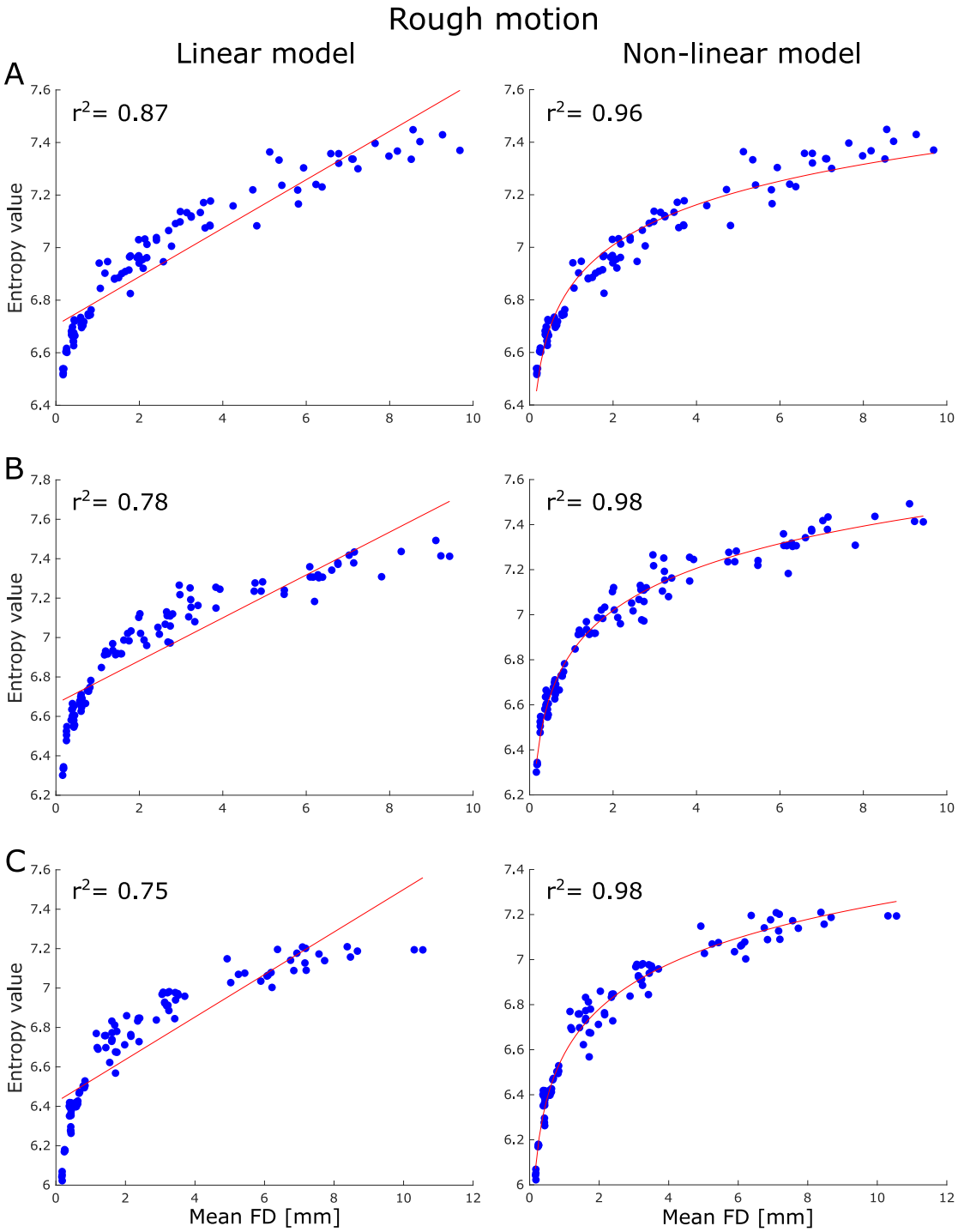

Figure 3.3.6: Comparison between linear and non-linear regression models in case of rough motion for dataset (A) 1, (B) 2 and (C) 3: the logarithmic model is shown to explain better the data in all cases compared to the linear model. Moreover, the mean FD range is much larger (up to 12 for Dataset 3) compared to the FD range displayed for smooth motion (Figure 3.3.5). Relative r-squared (r^2) values are reported on each figure.

3.4 Discussion

In this study, we assessed a simulation of the accuracy of motion parameter estimation from FatNavs across a broad range of head motion. GRAPPA reconstruction was expected not to work properly in case of large head position changes, because of inconsistencies between the ACS lines and the FatNav volume being reconstructed. The effect of this mismatch is shown in Figure 3.3.1: the Post-GRAPPA FatNav's image quality degraded compared to the Pre-GRAPPA volumes as the motion increases from "low" to "very high".

Two observers were asked to evaluate a total of 576 images from 1 (severe motion artifacts) to 4 (no visible motion artifacts) using a GUI in MATLAB. The multinomial logistic regression was performed to test the relation between the observers' scores and the GE, and to understand when the evaluation changed based on the entropy value. Figure 3.3.3 shows that the probability of falling into category 4 (no visible motion artifacts) decreased as the GE value increased, as expected. Nevertheless, the boundary between each category was found to be better defined in case of rough motion compared to smooth motion: Figure 3.3.3 shows that the probability does not exceed 0.5 for category 3 and 2 in Dataset 1 and for category 3 in Dataset 3 in presence of smooth motion. However, it is very close to 1 when rough motion affects the images. This is due to the fact that the image quality degrades much more quickly in case of rough motion compared to smooth data, with less ambiguous cases which could be assigned to both categories. Observers are expected to find less difficult to discern between images with some motion artifacts (category 3) and with strong motion artifacts (category 2), producing even a stronger agreement among evaluators. Moreover, the observers were asked to evaluate the image based on its overall quality: in future studies, trained neuroradiologists would be asked to assess the quality of clinical images based on the expected ability to discern abnormality of different sizes, which is expected to lead to more accurate evaluations.

Although FatNavs were demonstrated to correct for a large scale of motion, the GRAPPA reconstruction of the FatNavs themselves will be compromised in the presence of strong head position changes. This may lead to a misestimation of the motion parameters. Nonetheless, Figure 3.3.4 shows that for levels of motion (as RMS) between 3.7° and 3 mm, GRAPPA reconstruction does not affect FatNavs' estimation accuracy: our data suggests that motion that would be sufficient to lead to a category 2 rating (strong artifacts) can typically be corrected with FatNavs to a level corresponding to category 4 (no noticeable artifacts). Especially in case of rough motion, FatNav motion correction was proven to be indispensable, as a category 4 image quality could not be achieved without motion correction (Table 3.5). If a particular subject group is likely to move more than this, it may be necessary to adapt the FatNavs' acquisition to make it more robust to large motion, which is expected to be possible if the GRAPPA weights are dynamically updated during the scan.

The relation between the mean FD and the GE was investigated by comparing how well a linear and a non-linear regression models could fit our smooth and rough data. It was found that the

logarithmic model could describe our rough data much better compared to the linear model, as shown in Figure 3.3.6. This could be due to the entropy being based on the log-function. On the other hand, both linear and non-linear models did not seem to provide an exceptionally good fit to our smooth data: it is possible that a different model would provide a better description of our motion traces, which would lead to a more accurate estimation of the FD value that defines each image quality category boundary (Table 3.6). Unlike the RMS, which averages the motion parameters across the entire scan duration, the FD metric estimates the head position change between consecutive volumes throughout the acquisition. This made possible to analyse the extent of the motion corruption caused by different motion types, as the smooth and rough motion proposed in this study. As shown in Figure 3.3.6, our rough motion parameters resulted in much higher FD values compared to smooth motion ones for similar entropy values, with the FD increasing up to 10 in Datasets 1 and 2 and up to 12 in Dataset 3, while it did not exceed 1.6 in case of smooth motion (Figure 3.3.5). This is due to the fact that during rough motion, the subject is expected to perform abrupt head position changes, which result in larger motion between consecutive volumes. Although a definition of smooth and rough motion was given, more studies will be necessary to find a mathematical way to describe the difference between them. It is expected that the majority of routine MRI acquisitions are affected by smooth motion, where subjects move very slowly throughout the acquisition; however, rough motion is expected to be performed by less compliant subjects during MRI scans. The clear differences shown here in artifacts between the two categories suggests that being able to distinguish between smooth and rough motion becomes important to be able to test motion correction accuracy for different types of motion.

Category boundaries – Mean FD		
Category	**Smooth motion**	**Rough motion**
Category 4 to 3	0.078 mm	0.24 mm
Category 3 to 2	0.22 mm	0.42 mm
Category 2 to 1	0.50 mm	1.05 mm

Table 3.6: Mean FD category boundaries after FatNav correction was applied: rough motion FD values are shown to be higher then smooth ones, because of larger changes in head position between volumes, which characterize that motion type.

CHAPTER 4

Robust retrospective motion correction of head motion using navigator-based and markerless motion tracking techniques

Based on:

Elisa Marchetto, Kevin Murphy, Stefan Glimberg, Daniel Gallichan, *Robust retrospective motion correction of head motion using navigator-based and markerless motion tracking techniques*, (in final preparation).

Elisa Marchetto, Kevin Murphy, Daniel Gallichan, *Comparison of two retrospective tracking techniques in presence of fast and slow motion*, ISMRM 30th Annual Meeting, 2022.

Elisa Marchetto, Kevin Murphy, Daniel Gallichan, *Comparing retrospectively corrected motion with two tracking techniques*, Motion Detection and Correction: GatherTown Poster Session, 2021.

4.1 Introduction

Motion artifacts are a well-known issue in MR images [11], which might impede the interpretation of a patient's condition and obscure pathologies and regions of interest. To address these problems, MRI acquisitions can be repeated, but this leads to discomfort for the patient and increased costs for clinical or research centres [84], [85]. Methods have been developed in MRI to estimate the motion occurred and restore sharpness and resolution to reduce the need for reacquisition. For more details on the subject, please refer to Section 1.2 of this thesis.

In this work, we compared the motion correction based on the 3D FatNavs [44] and the Tracoline (TCL) markerless motion tracking system, which are described in Sections 1.2.4 and 1.2.5 respectively. We investigated which motion leads to the worst artifacts and how well image quality can be restored with the two different motion-tracking estimates. The aim is to understand how to achieve the best image quality in different motion scenarios, which is clinically relevant to reduce the need for rescans. To allow a direct comparison, the motion correction based on motion-estimates from the two tracking techniques was applied retrospectively to the same data.

4.2 Methods

4.2.1 Image acquisition

Data were collected from a group of 9 healthy subjects on a Prisma scanner (Siemens Healthcare, Erlangen, Germany) using a 64 channel RF coil array for signal reception. All subjects were scanned with an MPRAGE sequence at 1 mm isotropic resolution with TI/TE/TR = 1100/3.03/2410 ms and FA = 8°.
Following each readout train of the MPRAGE, a 3D FatNav navigator was acquired at 4 mm isotropic resolution (TE/TR = 1.43/3.4 ms, TA = 0.37 s), acceleration factor R=16, for a total scanning time of 5:38 min. ACS lines for the FatNavs were acquired once at the beginning of the scan to perform the GRAPPA reconstruction.
Calibration of the TCL data was performed at the end of the acquisition via the TracSuite software (v3.0.74), which involves aligning the reference point cloud from the TCL system to the surface of a structural MR volume of the whole head. The first MPRAGE scan from each session, without deliberate motion, was used for this calibration procedure.

Ethical approval for this study was obtained from Cardiff University School of Psychology Ethics Committee board. Written informed consent was obtained from all subjects before the study.

4.2.2 Motion experiments

Subjects were asked to follow the instructions given on an MR compatible screen positioned inside the scanner and visible via a mirror attached to the head coil. The mirror was positioned so that the participant could clearly see the screen and the TCL camera FOV was not affected. Instructions were coded using PsychoPy v. 30 [86] and consisted of a dot moving in different directions on screen: participants were asked to follow the dot with their nose so that movements could be carried out in a controlled way.
Different types of motion were conducted: stepwise, circular, pitch and "simulated realistic"

motion, as shown in Figure 4.2.1. During stepwise motion (Figure 4.2.1A and B), the dot moved in a "cross" shape: up, down, right, left, and along two diagonals (up-right, down-left; up-left, down-right), changing position every 35 s. The projected dot movement was 2.5 cm and 7.5 cm for small and large stepwise motion respectively, with an expected head motion of 1.9°and 5.6° based on the eye-screen distance of 76 cm.

Circular motion (Figure 4.2.1C) was performed similarly to Frost *et al.* [36], with the participant's head following a dot moving in circle (radius of 2.5 cm) for 1 min at different speeds: 6 cycles/minute and 4 cycles/minute. The motion was performed three times during a single MPRAGE acquisition: at the beginning, half-way through and towards the end of the scan, for a total of 3 min of motion over 5:38 min of scan time. The head was expected to rotate of 2.9° per ¼ of the circle.

Finally, "simulated realistic" motion patterns were generated, based heuristically on an example of existing motion traces in a non-compliant subject during an fMRI experiment, acquired without deliberate motion, where the subject seemed to move predominantly along the x-axis performing abrupt pitch rotations or slowly moving their head throughout the acquisition. Therefore, we derived two other types of motion: slow diagonal motion (Figure 4.2.1D and E) and pitch-wise motion (Figure 4.2.1F). The aim was to test the correction methods with what we considered more "realistic" motion. In our pitch-wise (nodding) motion scenario, the dot moved quickly down in 2 s, moved up to resting position in 15 s and stayed still for 35 s, for a total motion time of 17 s/min. The projected dot moved vertically on the screen for 2.5 cm, 5 cm, or 7.5 cm, corresponding to small, medium, and large levels of motion, for an expected pitch rotation of 1.9°, 3.8° and 5.6°. In our slow diagonal motion case, the subject was moving the head slowly for 1:30 min, starting from the centre along the up-right diagonal or the down-right diagonal (projected motion of 3.5 cm and predicted motion of 1.9°). One MPRAGE without deliberate motion was also acquired as a motion-free reference image for each session.

We obtained a total of 11 datasets, with subjects 3 and 4 being scanned twice on different days. We will refer to different acquisitions of the same experiment as runs. Table 4.1 details the experiments performed by each subject, summarised here as:

- Large Stepwise (LSW) and Small Stepwise (SSW), with head motion every 35 s.
- Circular motion 6 cycles/min (C6) and Circular motion 4 cycles/min (C4), with 3 min of motion per 5:38 min of total scan time.
- Small Pitch-wise (SPW), Medium Pitch-wise (MPW) and Large Pitch-wise (LPW), with a total motion time of 17 s/min.
- Slow Diagonal Up (SDU) and Slow Diagonal Down (SDD), with 1:30 min of motion per 5:38 min of total scan time.

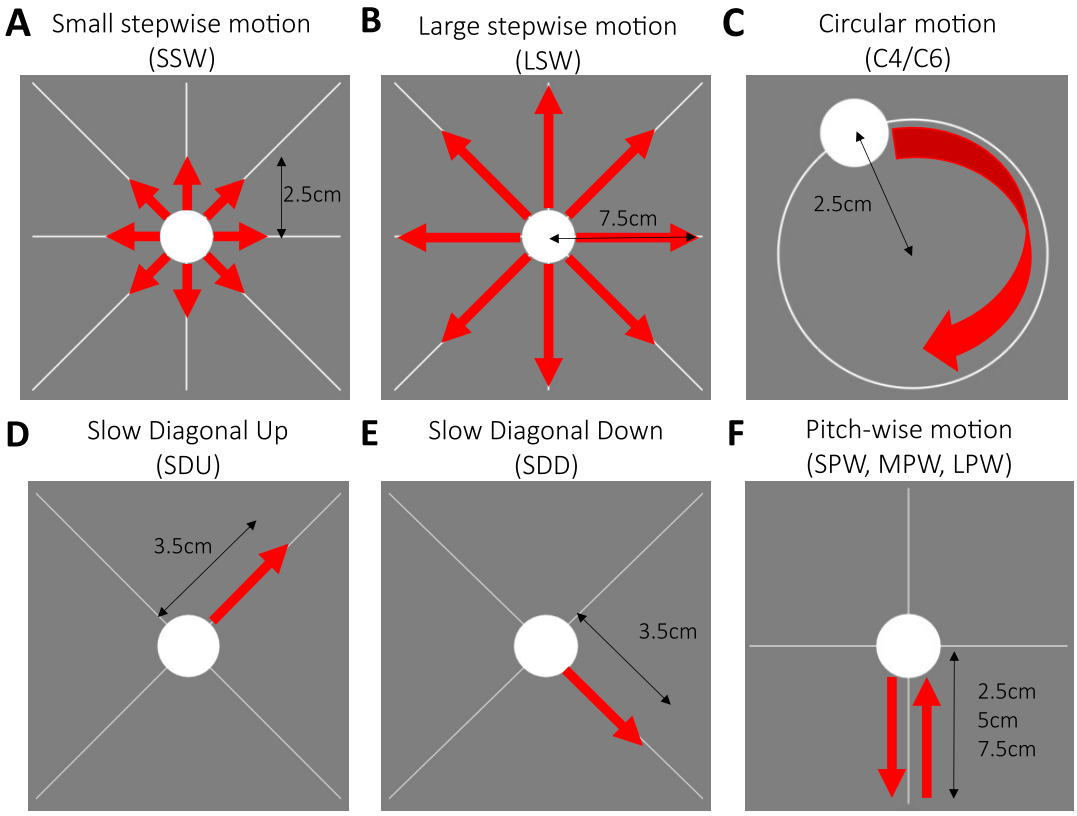

Figure 4.2.1: Projected dot motion directions for (A) small stepwise motion (head position changing every 35 s), (B) large stepwise motion (head position changing every 35 s), (C) circular motion (at 4 or 6 cycles/min, total head motion of 3 min over 5:38 min of total scan time), (D) slow diagonal motion along the up-right diagonal (total head motion 1:30/5:38 min), (E) slow diagonal motion along the down-right diagonal (total head motion 1:30/5:38 min) and (F) pitch-wise motion (head motion 17 s/min). The dot projected movement is reported (in cm) for each motion scenario. The predicted head motion was estimated based on the eye-to-screen distance (76 cm) as: (A) 1.9°, (B) 5.6°, (C) 2.9°, (D,E) 1.89° and (F) 1.9°, 3.8° and 5.6° for small (SPW), medium (MPW) and large (LPW) pitch-wise motion respectively.

4.2.3 Motion quantification

The motion score is a single value motion metric used by Tisdall *et al.* (10) to estimate the motion occurring during each TR. It is defined as:

$$score = \Delta R + \Delta x^2 + \Delta y^2 + \Delta z^2 \tag{4.1}$$

with Δx^2, Δy^2 and Δz^2 being the estimated translations along x, y and z.
ΔR (Eq. 4.2) is the largest displacement experienced by any point on a sphere of 64 mm radius rotated by an angle θ (Eq. 4.3).

Experiments performed for each participant

Subject 1	Still, Small Pitch-wise (SPW), Slow Diagonal Up (SDU), Slow Diagonal Down (SDD)
Subject 2	Still, Large Pitch-wise (LPW), Medium Pitch-wise (MPW), Circular motion 6 cycles/min (C6)
Subject 3	Still, Large Stepwise (LSW), Small Stepwise (SSW), Large Stepwise (LSW), Small Stepwise (SSW).
Subject 4	Still, Large Stepwise (LSW), Small Stepwise (SSW), Large Stepwise (LSW), Small Stepwise (SSW), Circular motion 4 cycles/min (C4)
Subject 5	Still, Large Stepwise (LSW), Small Stepwise (SSW), Circular motion 4 cycles/min (C4)
Subject 6	Still, Large Stepwise (LSW), Small Stepwise (SSW), Circular motion 6 cycles/min (C6)
Subject 7	Still, Circular motion 4 cycles/min (C4), Circular motion 6 cycles/min (C6)
Subject 8	Still, Circular motion 4 cycles/min (C4), Circular motion 6 cycles/min (C6)
Subject 9	Still, Circular motion 4 cycles/min (C4), Circular motion 6 cycles/min (C6)

Table 4.1: Summary of the experiments performed for each subject.

$$\Delta R = 64\sqrt{(1 - cos\Theta)^2 + sin\Theta^2} \tag{4.2}$$

$$\begin{aligned} |\Theta| = |arccos\tfrac{1}{2}[-1 + cos(\Theta_x)cos(\Theta_y) + cos(\Theta_x)cos(\Theta_z) \\ + cos(\Theta_y)cos(\Theta_z) + sin(\Theta_x)sin(\Theta_y)sin(\Theta_z)]| \end{aligned} \tag{4.3}$$

We calculated the mean motion score from each motion estimate and used it as a single value to represent rotational and translational motion. Moreover, we estimated the expected motion score based on theoretical motion traces of each type of motion, and the corresponding predicted head motion calculated from the projected dot movement.

4.2.4 Image reconstruction

The image reconstruction was performed in MATLAB using the *retroMoCoBox toolbox* [70]. Because the TCL data displayed high frequency noise in the original motion parameters, a moving average filter was used to smooth out the data prior to the reconstruction with a window size of 99 samples.

4.2.5 Image quality assessment

The image quality after the motion correction was assessed visually and using two different mathematical metrics: the Feature Similarity Index (FSIM) [87] and the Normalized Gradient

Squared (NGS) [41].
The FSIM was chosen as it has been shown to achieve much higher consistency with radiologist evaluations of image quality than other metrics [88], including the commonly used Structural Similarity Index (SSIM) [89]. The primary feature used to calculate the FSIM is the Phase Congruency (PC), which is a robust spatial frequency-based system able to identify similarities at the edges: Fourier components (here calculated from a magnitude-image) with high PC values identify features with sharp changes between light and dark areas, which are what we visually perceive as edges.
The PC for each point x of a 2D image can be mathematically described as follows:

$$PC(x) = \frac{\sum_j E_{\theta_j}(x)}{\epsilon + \sum_n \sum_j A_{n,\theta_j}(x)} \tag{4.4}$$

with $E_{\theta_j}(x)$ being the local energy along the orientation θ_j (with j being the orientation angle), A_{n,θ_j} being the local amplitude on a scale n and ϵ a small positive constant.
Because the PC is contrast invariant, the gradient magnitude was added as the second factor of this metric, defined as shown in Eq.4.5.

$$G = \sqrt{G_x^2 + G_y^2} \tag{4.5}$$

with x and y the two directions along which the gradient was calculated.
The FSIM requires a reference image to be computed and its value varies between 0-1, where 1 is obtained when the two images being compared are identical. Firstly, the similarity map between the image being evaluated and a reference is calculated for the PC and the gradient separately:

$$S_{PC} = \frac{2PC_1(x) \cdot PC_2(x) + T_1}{PC_1^2(x) \cdot PC_2^2(x) + T_1} \tag{4.6}$$

$$S_G = \frac{2G_1(x) \cdot G_2(x) + T_2}{G_1^2(x) \cdot G_2^2(x) + T_2} \tag{4.7}$$

with $T_1 = 0.85$ and $T_2 = 160$ as in [87]. The two similarities are then combined as:

$$S_L(x) = S_{PC}(x) \cdot S_G(x) \tag{4.8}$$

As areas with high PC indicates sharp edges, the importance of S_L is weighted using $PC_m(x) = max(PC_1(x), PC_2(x))$. The FSIM can be mathematically described as:

$$FSIM = \frac{\sum_{x \epsilon \Omega} S_L(x) \cdot PC_m(x)}{\sum_{x \epsilon \Omega} PC_m(x)} \tag{4.9}$$

The quality of the acquired images was also assessed with the NGS metric, which has been found by McGee *et al.* as the second-best quality metric for autofocusing, correlating most closely with observer judgments on MRI images of the shoulder [41]. NGS allows the evaluation

of the image quality without comparing it with a reference and postulating that ideal images should have areas of uniform brightness separated by sharp edges.
The NGS is defined as the normalized convolution between the Prewitt operator and the pixel values $g_{i,j}$:

$$NGS = \sum_{ij} \left(\frac{\left| \begin{bmatrix} 1 \\ -1 \end{bmatrix} * g_{i,j} \right|}{\sum_{ij} \left| \begin{bmatrix} 1 \\ -1 \end{bmatrix} * g_{i,j} \right|} \right)^2 \tag{4.10}$$

It has been used by Lin *et al.* [90] because of its lower computational cost compared with the GE metric, and Bazin *et al.* [91] chose it as a metric as expected to be more sensitive than the entropy of gradients to limited motion. The NGS has also been successfully used by Gretsch *et al.* [45] to compare the quality of images after FatNav and MPT motion correction. The NGS value was expected to increase as the image became sharper.
Before all metrics were calculated, each 2D slice was normalized by subtracting the minimum value and dividing by the difference between the maximum and minimum values (min-max scaling). To estimate the FSIM metric, an extra rescale step between 0-255 was required. Final values were estimated averaging them over the 30 central axial slices [36].

4.2.6 Improving FatNavs motion estimation

When FatNav volumes are acquired, a strong signal can be detected in the neck region as well as around the scalp. The scalp can be expected to move reasonably rigidly with the head (and brain), whereas the neck movement is non-rigid. The standard processing for 3D FatNavs in the retroMoCoBox software is to use SPM [78] to perform 6-DOF rigid-body alignment between FatNav volumes in order to generate motion estimates. If more signal is acquired in the non-rigid neck region this will affect the quality of the motion estimates, an effect which is particularly noticeable using the Siemens 64-channel RF coil, because it is a "head and neck" coil with receive channels extending into the neck region.
Other navigator-based motion correction systems allow to compensate for the effect of non-rigid body motion to the estimated parameters. PROMO (PROspective MOtion correction) [30] uses a 2D spiral navigator (SP-Navs) and a image-based tracking technique [92] to estimate rigid-body motion parameters. Here an Extended Kalman Filter (EKF) was used to prevent non-rigid motion of the neck and jaw to corrupt the rigid motion parameters. On the other hand, PACE (Prospective Acquisition CorrEction) [93] uses automatically calculate bounding box to roughly cover the interior slices of a brain volume, therefore removing the non-rigid neck region.
We therefore tested whether masking the non-rigid part of the head would improve the motion parameter estimation and image quality in all our motion scenarios: we expected the mask to be particularly beneficial in the case of strong pitch-motion, as this direction of motion is

likely to have the largest discrepancy between head movement and apparent motion in the neck.

To generate the mask corresponding to the parts of the scalp expected to move rigidly (and therefore allowing exclusion of non-rigid regions), we first selected the T1-weighted (T1w) image of one dataset acquired without deliberate motion and the corresponding first FatNav volume. We registered the T1w and the FatNav volume using the FSL *FLIRT* function [94,95], to have a 3D FatNav and an MPRAGE image in the same space. After applying BET (*Brain Extraction Tool*) [96,97], we registered the T1w volume to the 1 mm MNI152 standard space brain [71]. By following the same process, a 3D FatNav for each subject could be brought into a standard space, and then averaged using *fslmaths* from the *FSLutils* [98] to obtain a standardised FatNav volume. *ITK-SNAP* [99] was used to manually define a mask in this standard space that would exclude the neck region. When estimating the motion parameters for each subject from the FatNavs, the first FatNav from the subject was co-registered to the standardised FatNav volume, allowing the mask to be brought into subject-space and incorporated as a weighting image to *spm_realign* (SPM) function.

4.3 Results

4.3.1 Comparison between FatNavs and TCL motion correction

Figure 4.3.1 summarises all the FSIM values (measured against the "still" image) for all motion scenarios and the 3 different motion correction methods. The FSIM score improved by applying all motion correction methods in our stepwise and slow diagonal motion scenarios. In our small and large stepwise motion scenarios, a substantial improvement in the sharpness was obtained by masking the non-rigid part of the head during the FatNav volumes registration, with only small residual artifacts still visible: the use of the neck-mask for FatNavs ("FN wMask") improved the image quality in runs 1, 2, 4, 5 and 6 for large stepwise motion and 1, 2 and 4 of small stepwise motion shown in Figure 4.3.1, compared to when no mask is used ("FN woMask"). In Figure 4.3.2, we compare the motion parameters and MPRAGE images obtained from the two FatNav's tracking methods for the corresponding run 2 of small stepwise motion, showing the clear improvements obtained by removing the neck-region during the FatNavs registration. Moreover, the masked FatNav and the TCL corrections are compared in Figure 4.3.3: here the top parts of the image (front regions of the brain) were clearly made sharper by the TCL correction. However, the overall best motion correction was obtained using the masked FatNav estimates: although some artifacts are still visible on the top part of the image, the correction reduced the ringing artifacts on the bottom of the image compared to the TCL method. For circular motion at 6 cycles/min, circular motion at 4 cycles/min and small, medium and large pitch-wise motion, the outcome is more nuanced, including some examples of cases where the motion-correction even appears to lead to a loss of image quality (i.e. a reduction in FSIM following the application of the motion-correction). Figure 4.3.4 illustrates an example of circular motion with the participant performing head rotations at 4 cycles/min. The ringing artifacts visible on the uncorrected image were successfully reduced (although not fully eliminated) by correcting using all three motion-estimation techniques, leading to a better image quality.

For pitch-wise motion (images not shown), subjects moved at three different magnitudes for each run, following a projected dot movement of 2.5 cm for run 1, 7.5 cm for run 2 and 5 cm for run 3, corresponding to small, medium and large pitch-wise motion. The artifacts were almost undetectable in run 1 (2.5 cm), as the subject movement had such low magnitude. In run 2 (7.5 cm), TCL-based correction led to an apparent degradation of the image quality measured by the FSIM: despite some small improvements visible on the top part of the image, the bottom part displayed strong artifacts, probably caused by the abrupt nod motion or facial movements that reduced the tracking accuracy. During run 3 (5 cm), ringing artifacts were reduced by FatNavs and TCL, especially in the top part of the brain, improving the image quality compared to the uncorrected image, as shown in Figure 4.3.1 (pitch-wise motion

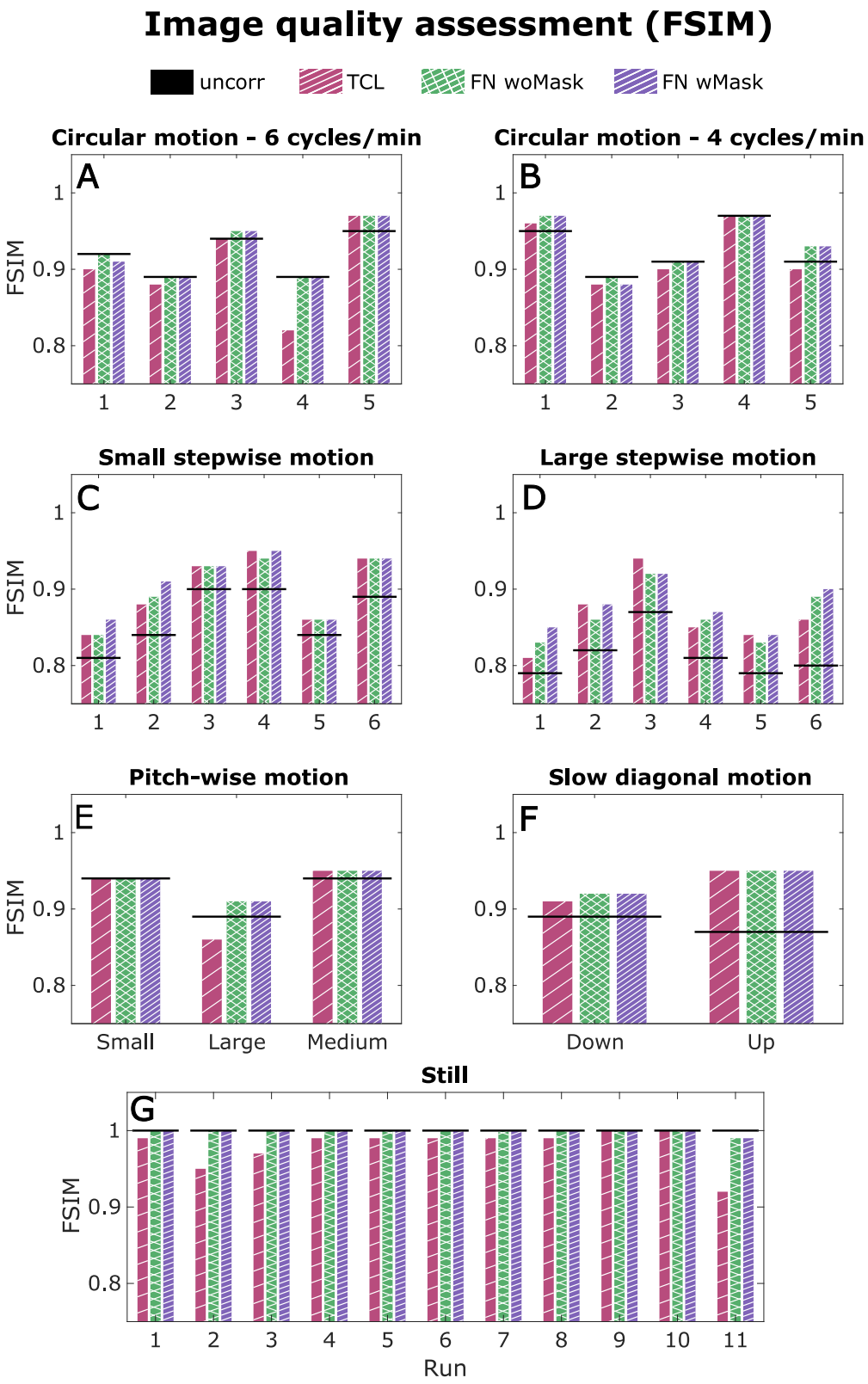

Figure 4.3.1: Comparison of FSIM values (against the reference image) of TCL-based corrected (red), FatNav without mask ("FN woMask" in green) and with mask ("FN wMask" in purple) corrected images obtained from the runs performed for each motion scenario. The FSIM value of the initial uncorrected image is reported as a straight black line.

case).

Both FatNavs and TCL performed well when applied to retrospectively correct the images affected by slow diagonal motion across the two diagonals. One example is illustrated in Figure 4.3.5 where the motion-corrected images from both FatNavs and TCL motion estimates are sharp and clear, with no visible residual artifacts.

When comparing between motion-estimation methods, no clearly better correction was found for any of the motion scenarios. However, the image quality after FatNav motion correction is shown to be very close to 1 in all runs of our non-deliberate motion acquisition (still scenario in Figure 4.3.1), meaning perfect matching with each corresponding reference image. The good sharpness displayed by the reference images shown in Figure 4.3.6 corroborated that FatNav motion correction did not introduce any degradation when no-deliberate motion was performed. On the other hand, TCL is shown to have a FSIM score as high as FatNavs in only two cases, namely runs 9 and 10 in Figure 4.3.1, indicating that the image quality decreased due to artifacts originated from the TCL motion compensation especially in runs 2, 3 and 11. FatNavs and TCL motion traces for the aforementioned runs (2, 3, 9 and 10) are reported in Figure 4.3.7 for comparison.

4.3.2 Smoothing TCL motion parameters

We chose to smooth the motion estimates from the TCL prior to performing the retrospective motion-correction to reduce the influence of high-frequency fluctuations present in the data. The smoothing function did not cause any image degradation, improving the image quality in some of our motion scenarios (e.g. runs 1, 2, 3, 4 and 6 of small stepwise motion in Figure 4.3.8), compared to the non-smoothed images, based on the value measure by the FSIM quality metric. One example for small stepwise motion (run 5 in Figure 4.3.8) is reported in Figure 4.3.9. However, the FSIM score still resulted below the target value of 1 in our non-deliberate motion case (still scenario) as shown in Figure 4.3.1, which was attributed to a tracking error rather than the noise on the motion traces, because of the TCL higher motion scores compared to FatNavs, which are reported in Figure 4.3.10.

4.3.3 Motion quantification

The mean motion score was chosen as single value measurement to evaluate the amount of motion performed by each subject in our motion scenarios and it is estimated as the average of the difference between consecutive head poses. A summary of all the mean motion scores estimated for TCL and FatNav with and without mask are reported in Figure 4.3.10. One clear observation from this figure is that the magnitude of the TCL-based motion parameters is larger than the FatNav-based estimate in most of our experiments. It also displays how differently the motion parameters are estimated by FatNav with and without the mask,

especially in the case of stepwise motion. Moreover, Figure 4.3.10 shows that the motion score found based on the motion performed by our participant was smaller compared to the expected motion score (black horizontal line in Figure 4.3.10) estimated based on theoretical motion traces. The estimated magnitude of the head rotation was expected to be 1.9° and 5.6° for small and large stepwise motion respectively, based on the eye to screen distance and the projection of the dot movement on the screen. Subjects moved more than expected while performing small stepwise motion, with a head rotation averaged across subjects of 2.8° ($\pm$0.9) and 2.0° ($\pm$0.8) for TCL and the masked FatNav respectively. In case of large stepwise motion, the average rotation was found as 5.1° ($\pm$3.3) and 4.4° ($\pm$3.4). The large standard deviation obtained for large stepwise motion is due to the different range of motion across runs: this demonstrates how different participants varied in the magnitude of motion when performing the same motion type (in the top four graphs of Figure 4.3.10, the motion shown on the MR projection screen was the same for all subjects for the same motion type). The motion estimates obtained from FatNav with and without the mask for all motion types are compared using scatter plots in Figure 4.3.11. Most of the dots lie close to the identity line (y = x), apart from for the rotations around the x-axis. This fits our expectation that nodding motion of the head leads to the strongest deviations from purely rigid motion within the FOV of the FatNav.

4.3.4 Image quality assessment

Both FatNavs and TCL motion correction are shown to improve the image quality in presence of small stepwise, circular and slow diagonal motion, reported in Figure 4.3.3, 4.3.4 and 4.3.5 respectively, with the corresponding FSIM quality metric values, which are reported for each correction method, concurring with this observation by increasing after the motion correction. On the other hand, the NGS values found for the same motion cases was reported to be smaller for the corrected images compared to the uncorrected cases: this implies a reduction in image quality, which is in contrast with simple visual inspection of the images in Figures 4.3.3, 4.3.4 and 4.3.5. More examples of this behaviour are found in Figure 4.3.12 for the small stepwise motion scenario.

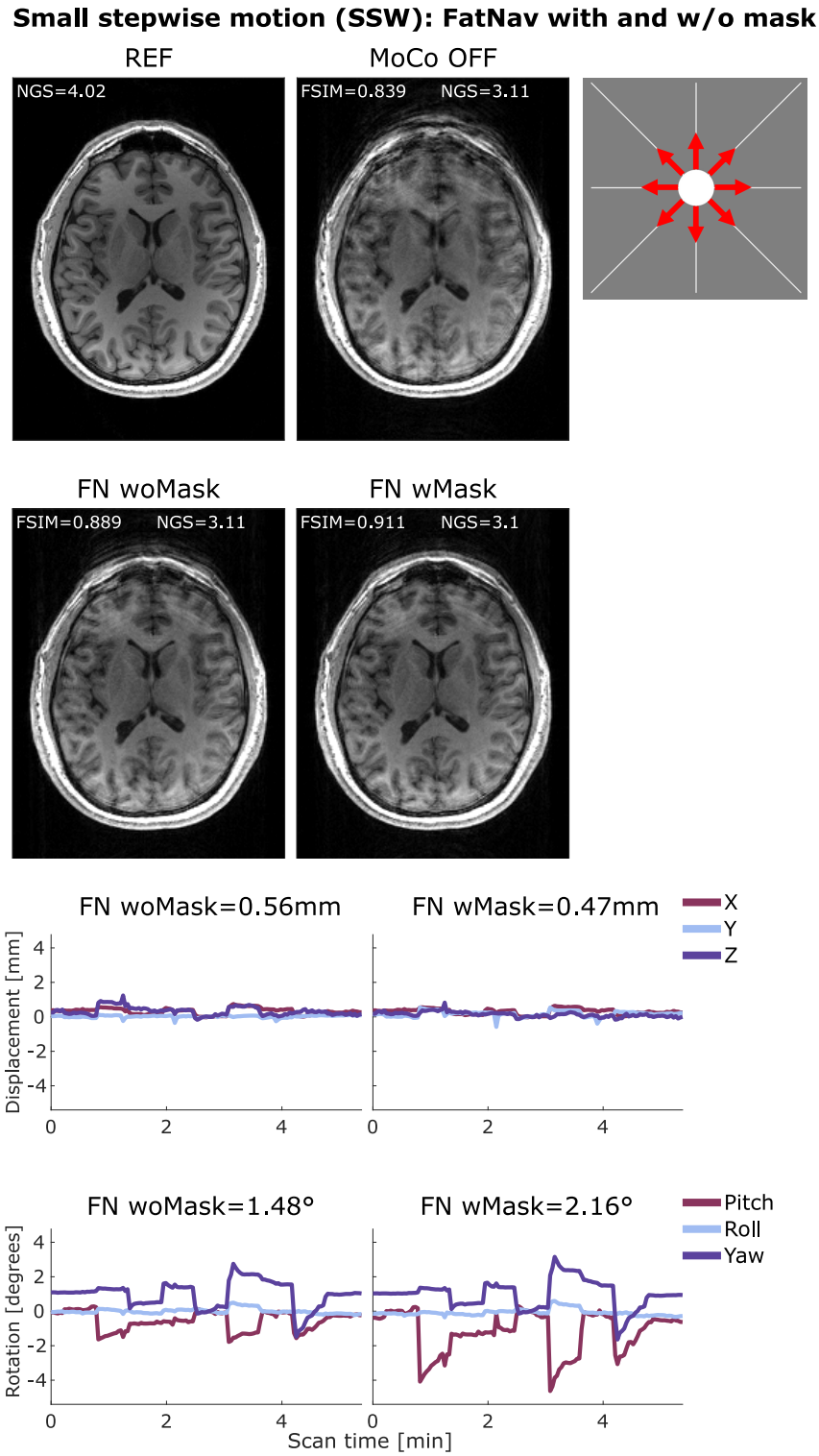

Figure 4.3.2: (A) Comparison between reference (Ref), uncorrected (MoCo OFF), and the corrected images (FN woMask, FN wMask) for small stepwise motion: the NGS and FSIM values are reported for each image. (B) Motion parameters estimated by the FN woMask (left column) and the FN wMask (right) tracking methods, with the RMS value reported on top of each motion trace for translations (in mm) and rotations (in degrees). The motion was timed to start 20 s after the beginning of the scan, with the head position changing every 35 s after that. The total scan duration was 5:38 min.

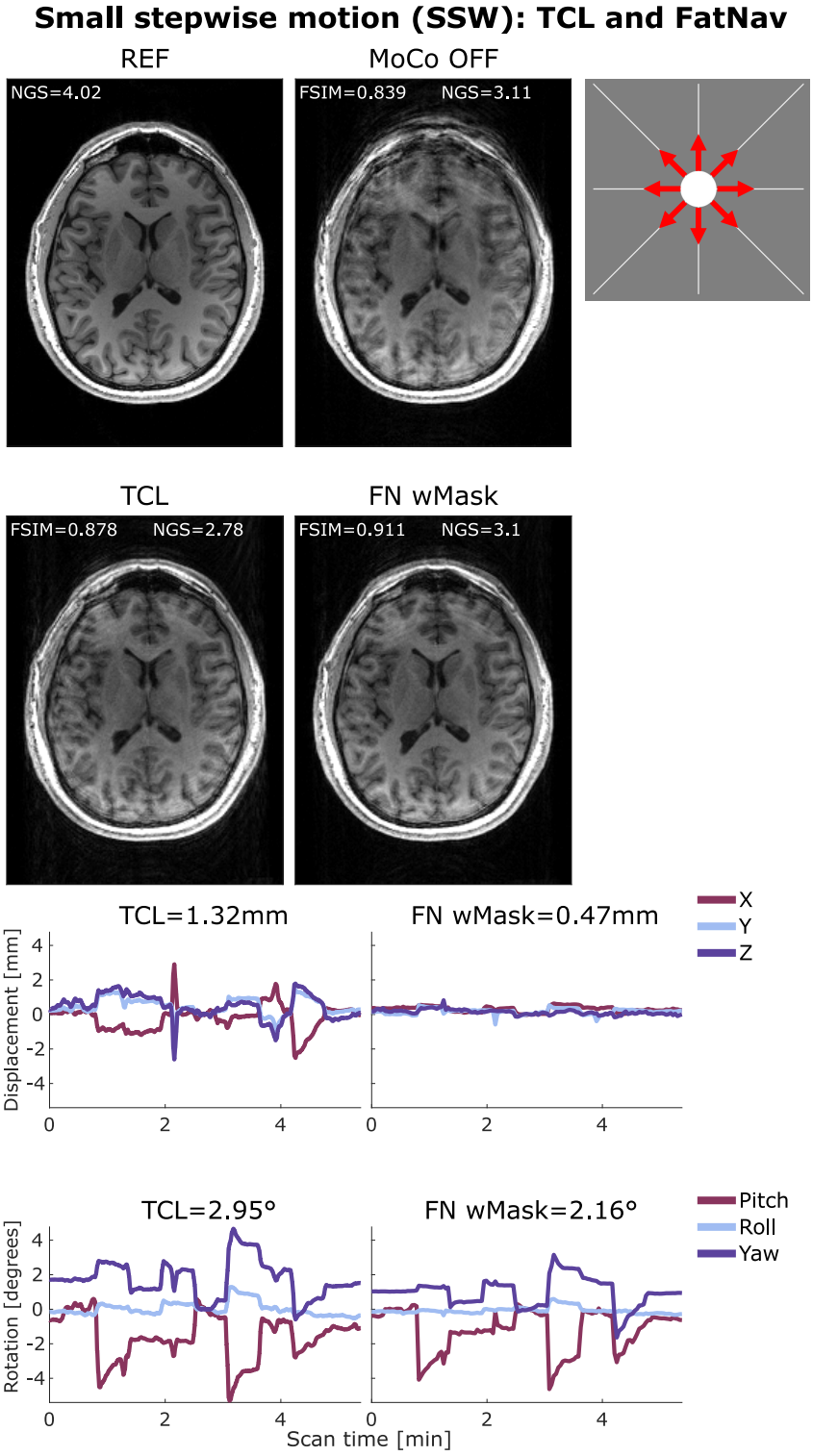

Figure 4.3.3: (A) Comparison between reference (Ref), uncorrected (MoCo OFF), and the corrected images (TCL, FN wMask) for small stepwise motion: the NGS and FSIM values are reported for each image. (B) Motion parameters estimated by the TCL (left column) and the FN wMask (right column) tracking methods, with the RMS value reported on top of each motion trace for translations (in mm) and rotations (in degrees). The motion was timed to start 20 s after the beginning of the scan, with the head position changing every 35 s after that. The total scan duration was 5:38 min.

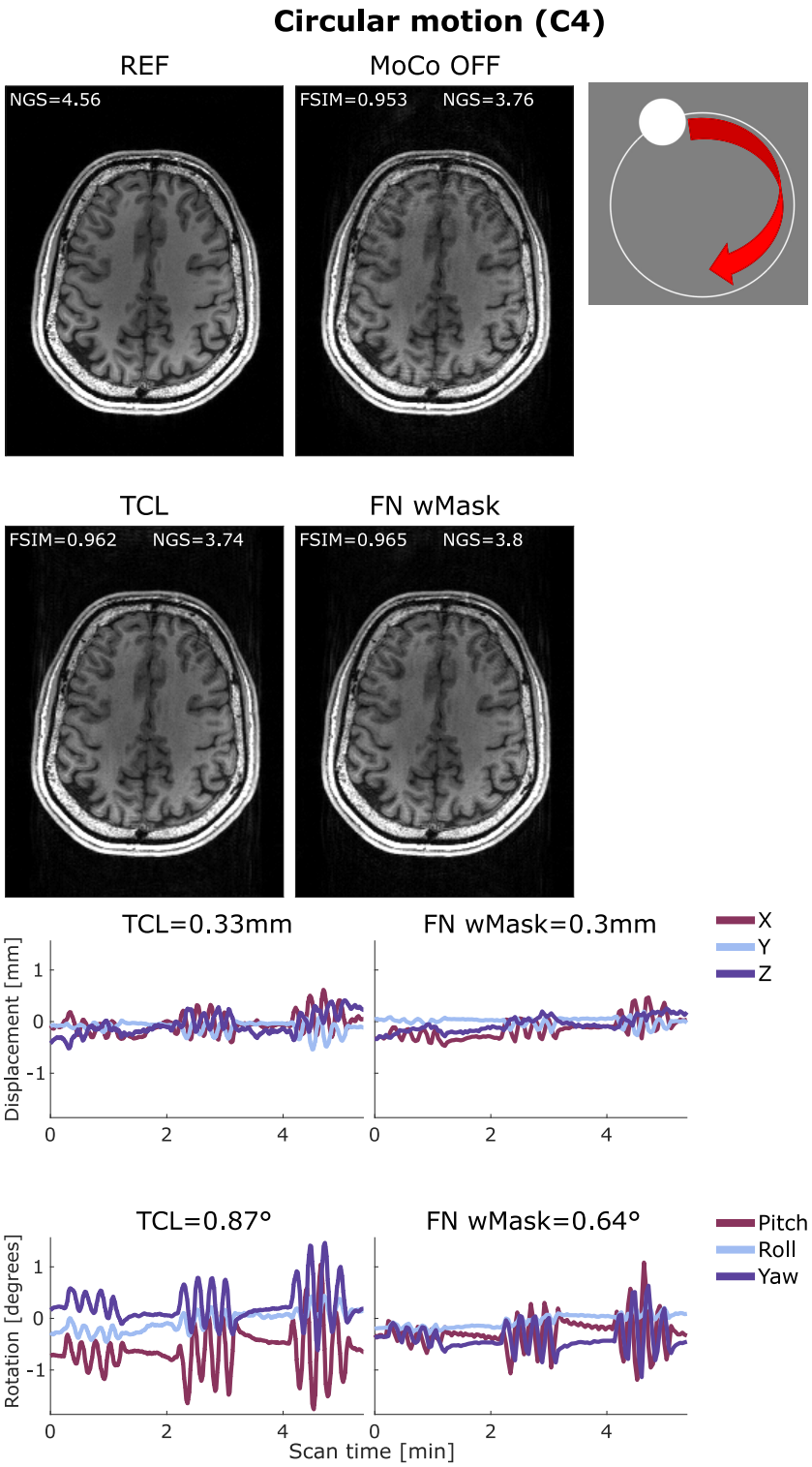

Figure 4.3.4: (A) Comparison between reference (Ref), uncorrected (MoCo OFF), and the corrected images (TCL, FN wMask) for circular motion (4 cycles/min): the NGS and FSIM values are reported for each image. (B) Motion parameters estimated by the TCL (left column) and the FN wMask (right column) tracking methods, with the RMS value reported on top of each motion trace for translations (in mm) and rotations (in degrees). The motion was timed to start 10 s after the beginning of the scan, continue for 1 min followed by 1 min without voluntary motion and repeated other two times, for a total head motion time 3/5:38 min.

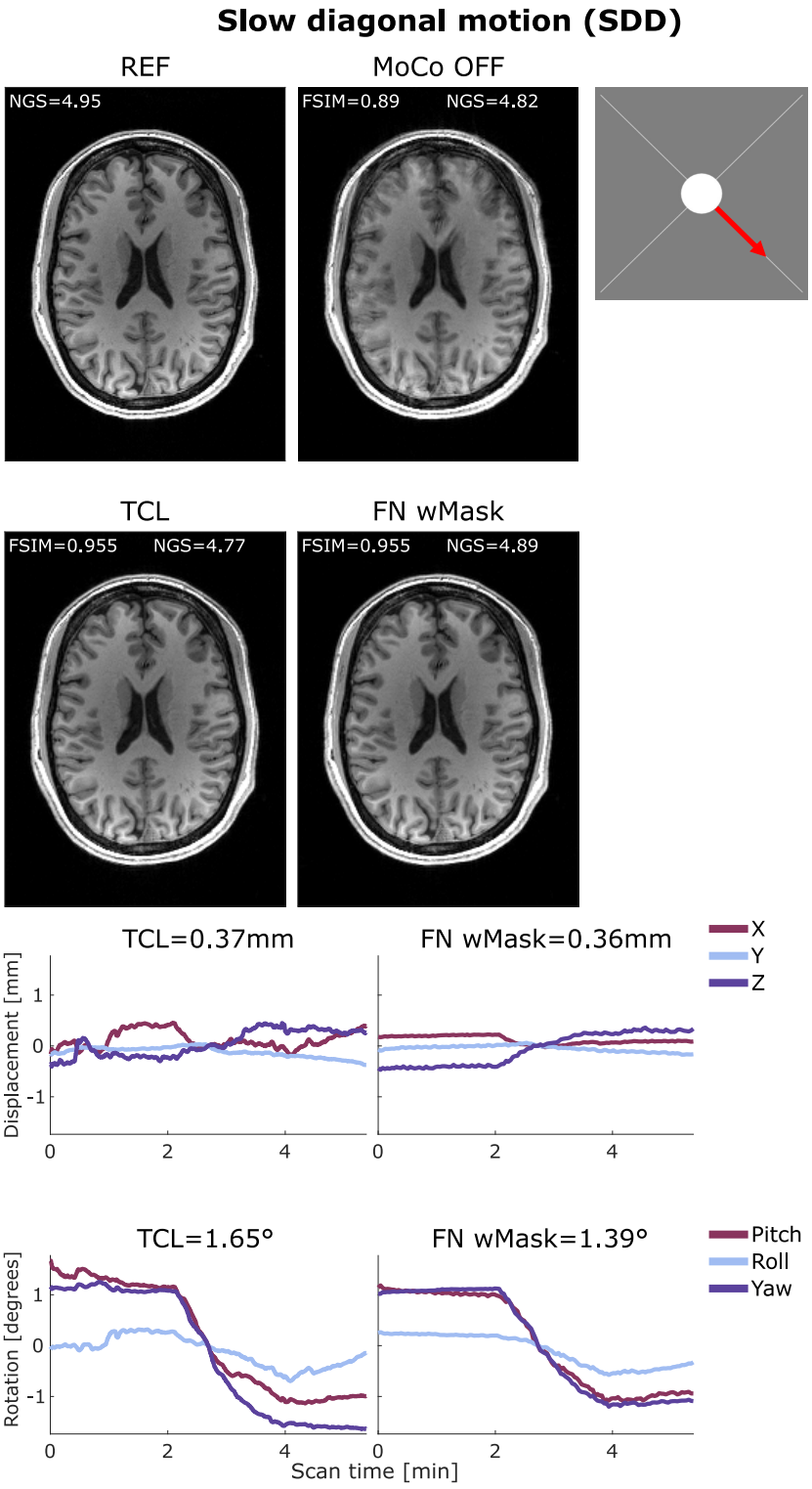

Figure 4.3.5: (A) Comparison between reference (Ref), uncorrected (MoCo OFF), and the corrected images (TCL, FN wMask) for slow diagonal motion (SDD): the NGS and FSIM values are reported for each image. (B) Motion parameters estimated by the TCL (left column) and the FN wMask (right column) tracking methods, with the RMS value reported on top of each motion trace for translations (in mm) and rotations (in degrees). The motion started 2 min after the beginning of the scan and continued for 1:30 min, for a total head motion of 1:30/5:38 min.

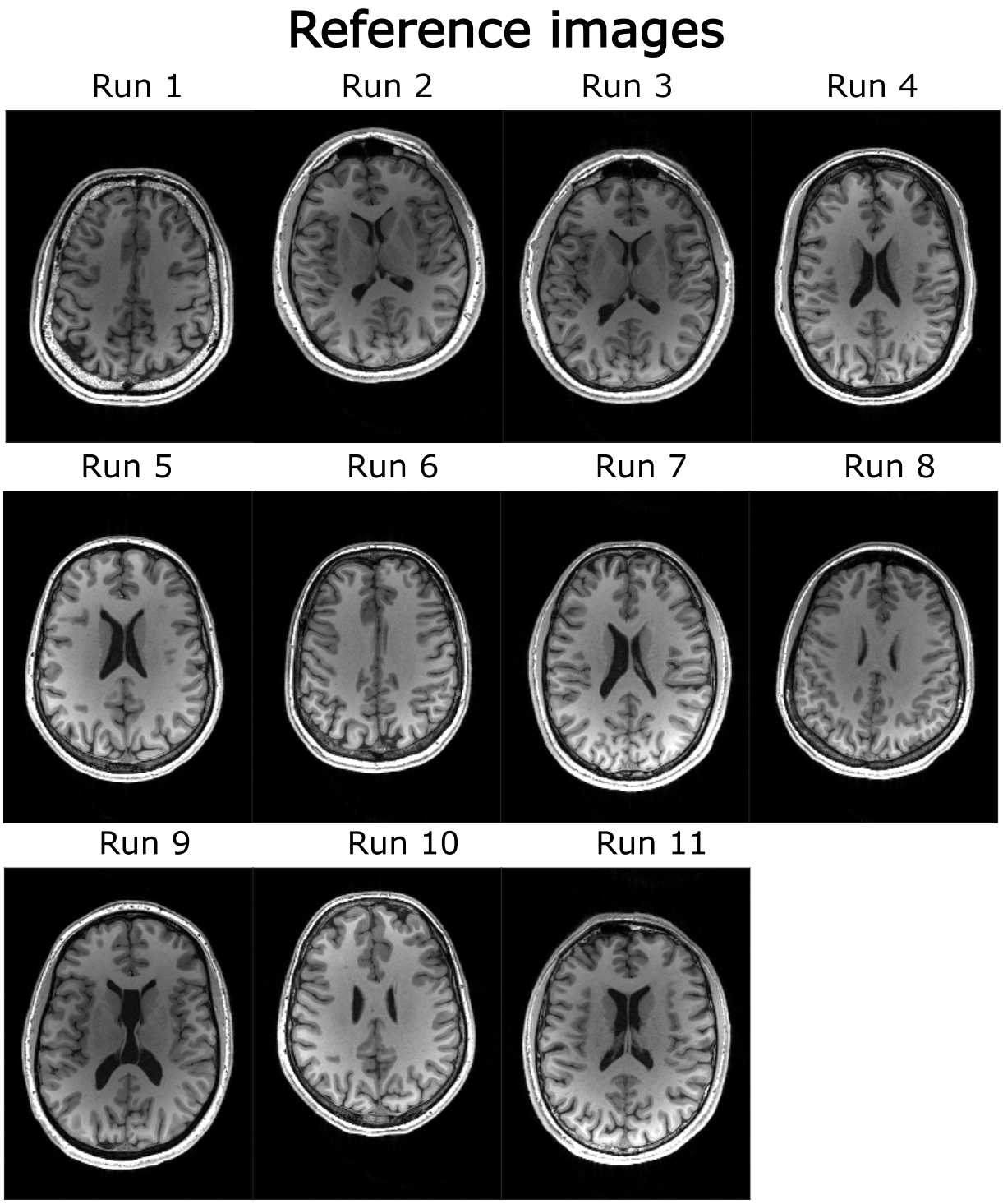

Figure 4.3.6: Comparison of all reference volumes acquired without deliberate motion at the beginning of each scan session. No motion correction was applied. All subjects were instructed to stay as still as possible during the scan, which resulted in no visible motion artifacts in the volumes acquired.

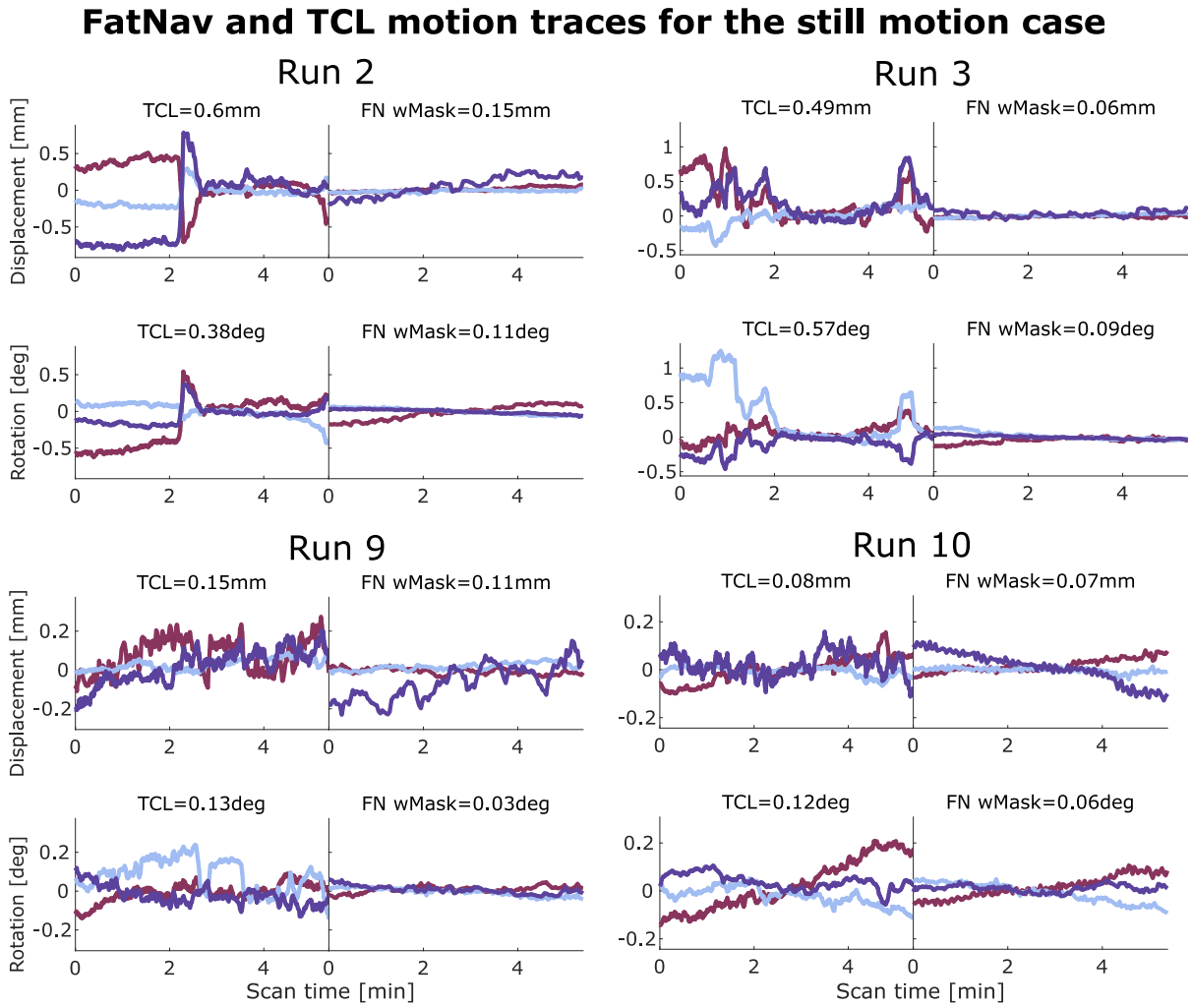

Figure 4.3.7: Comparison of FatNav and TCL motion parameters for the still motion experiments 2, 3, 9, 10 and 11 shown in Figure 4.3.6G. In runs 2, 3 and 11, the image quality seems to decrease after TCL motion correction based on the FSIM score, while the image quality is the same as FatNavs in runs 9 and 10.

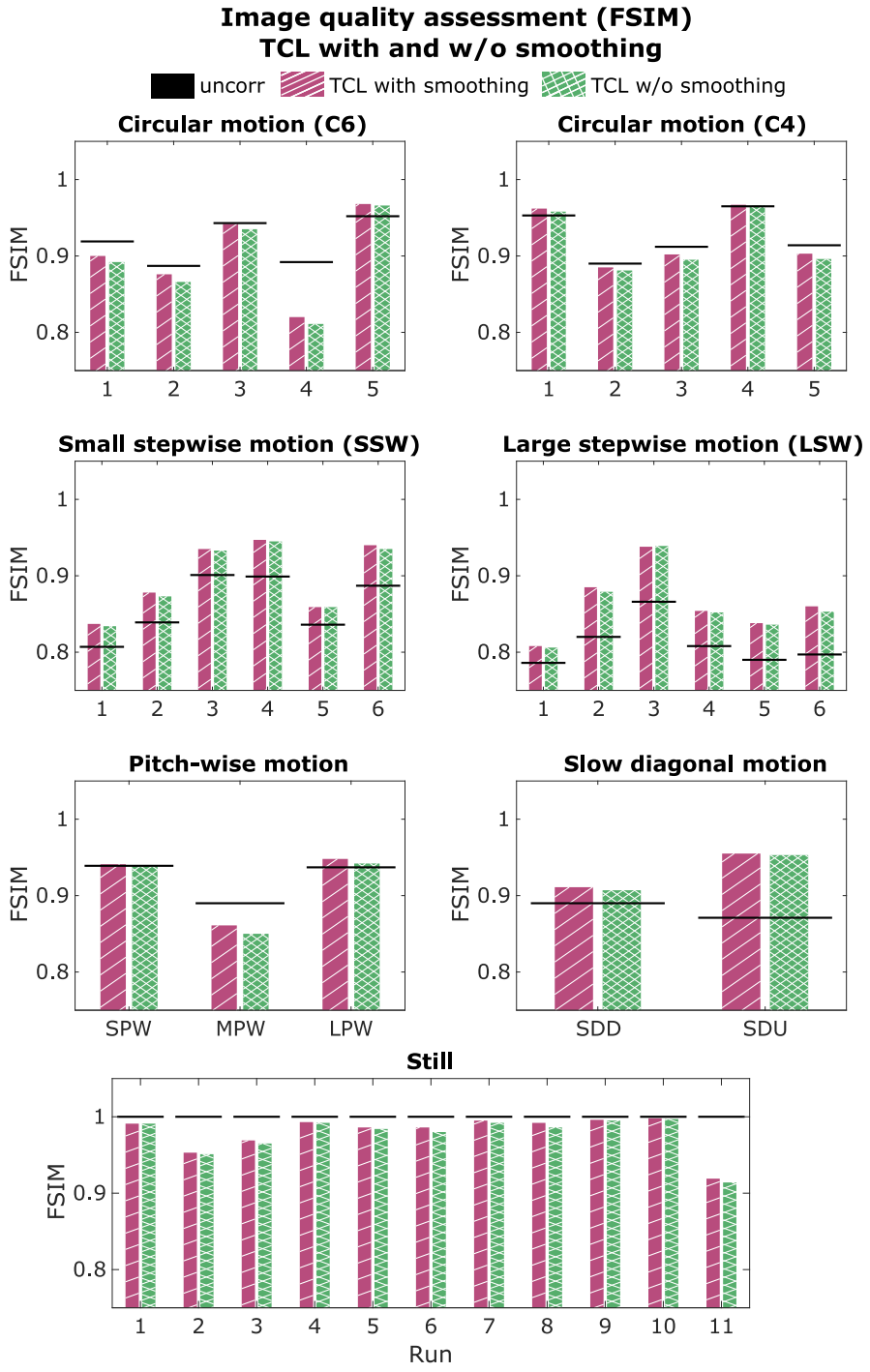

Figure 4.3.8: Comparison of the FSIM quality score, calculated against the reference images, in all our motion scenarios with and without using a smoothing function (pink and green respectively) on the TCL motion parameters prior reconstruction. The smoothed function did not cause any degradation compared to the non-smooth case, improving the image quality in some runs of our motion scenarios (e.g. runs 1, 2, 3, 4, and 6 of small stepwise motion). However, the FSIM score still resulted below the target value of 1 in our non-deliberate motion case (still scenario), which was attributed to a tracking error rather than the noise on the motion traces, because of the TCL higher motion score compared to FatNavs (runs 2, 3, 4, 5, 6, 8, 9, and 11 in Figure 4.3.10).

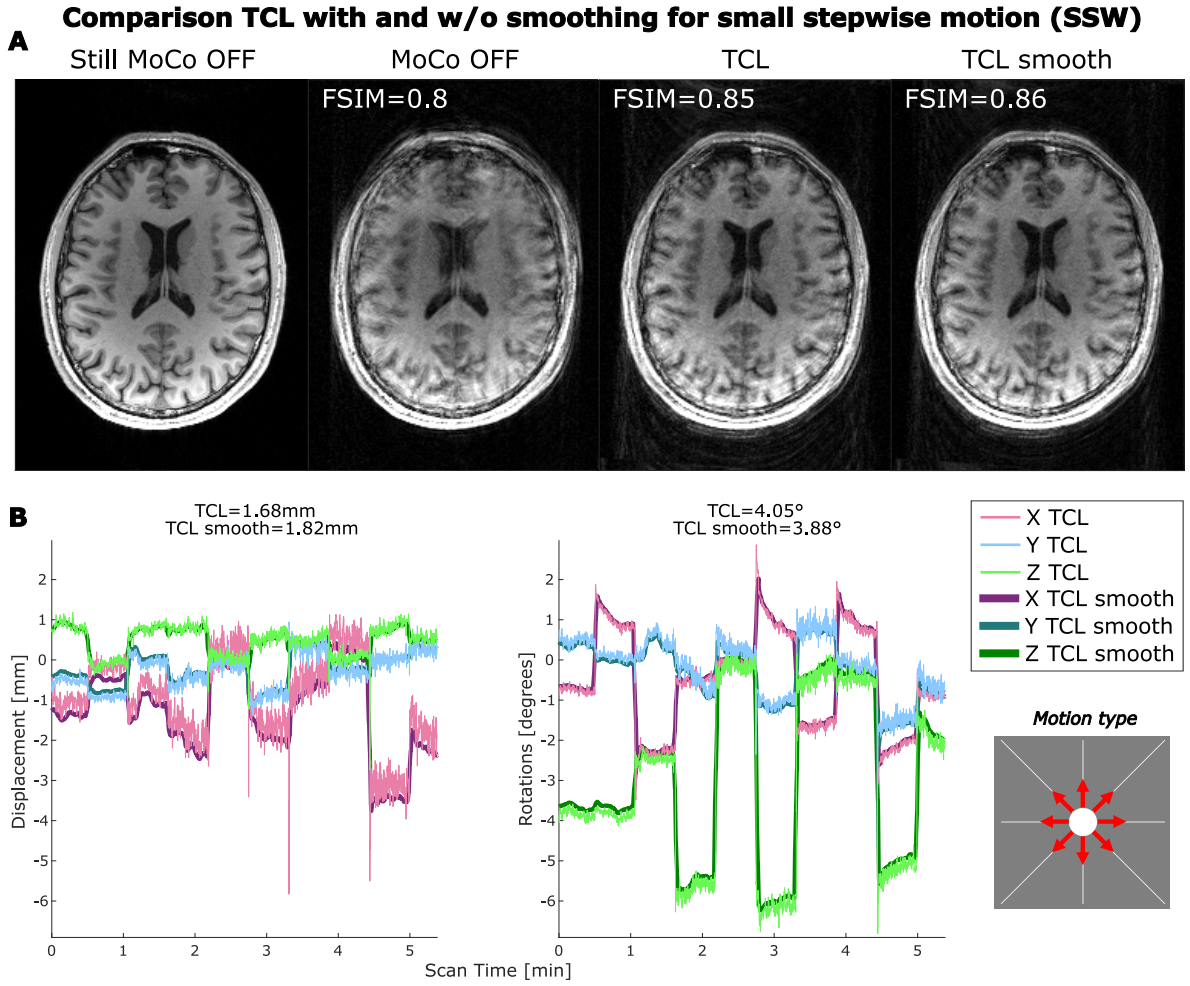

Figure 4.3.9: The effect of smoothing on the TCL-based motion estimation. Comparison between TCL-based motion estimation before and after applying the smoothing function: (A) TCL after smoothing (TCL smooth) shows less ringing artifact compared to the "unsmoothed" version (TCL), which is corroborated by the improvement in the FSIM value. (B) the unfiltered parameters (thin lines) are affected by noise, which is suppressed after filtering (thicker lines).

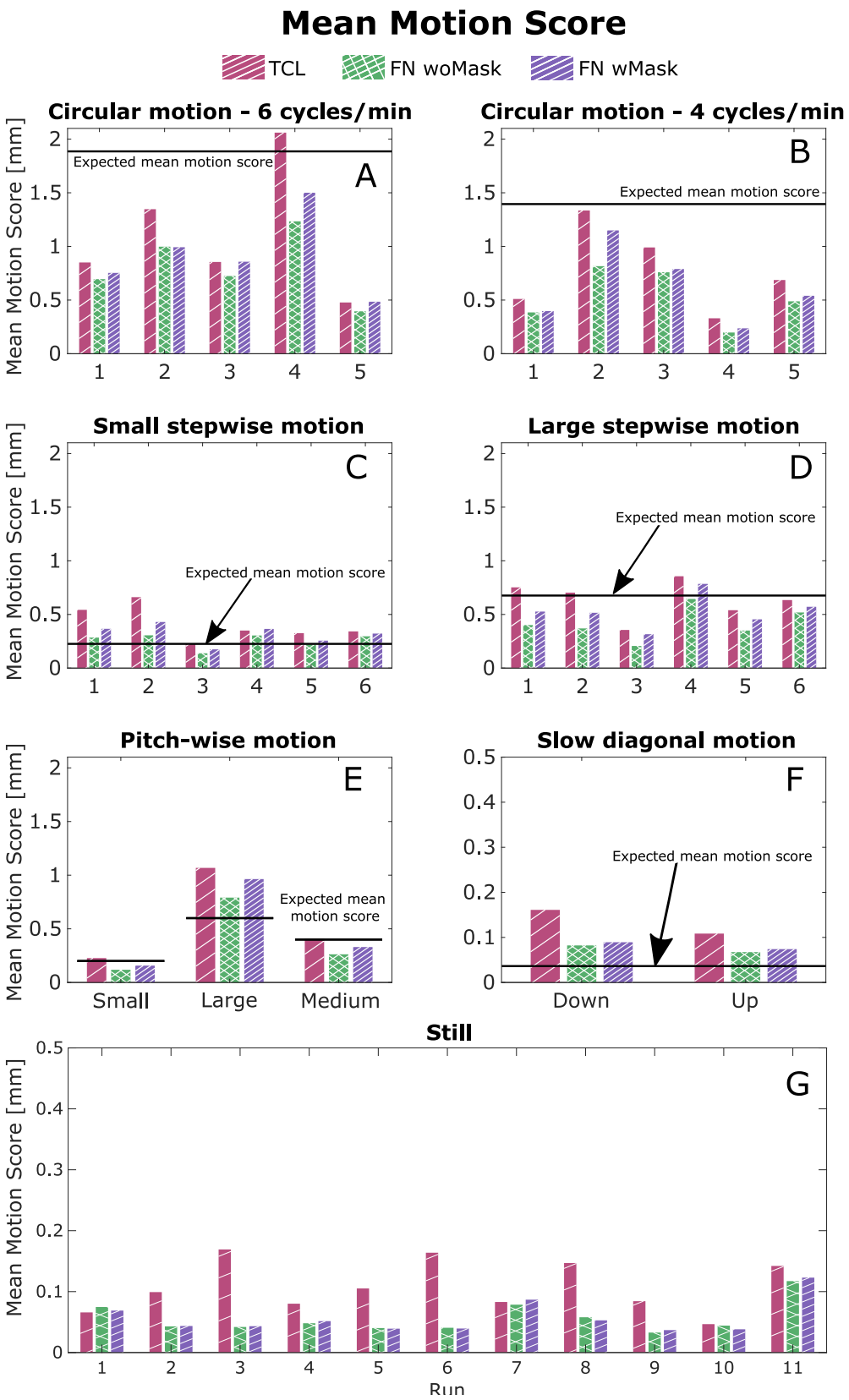

Figure 4.3.10: Comparison of the motion scores estimated for each run of our motion scenarios. Each motion score was calculated from the motion parameters measured by our three motion tracking modalities: TCL (red), FN woMask (green) and FN wMask (purple). The expected motion score (based on the eye-to-screen distance and the projected dot motion) is reported as a black horizontal line. The y-axis for the still and slow diagonal motion cases was ranged differently (from 0 to 0.6 mm instead of from 0 to 3.5 mm) to easily see the difference in the motion score values between tracking techniques.

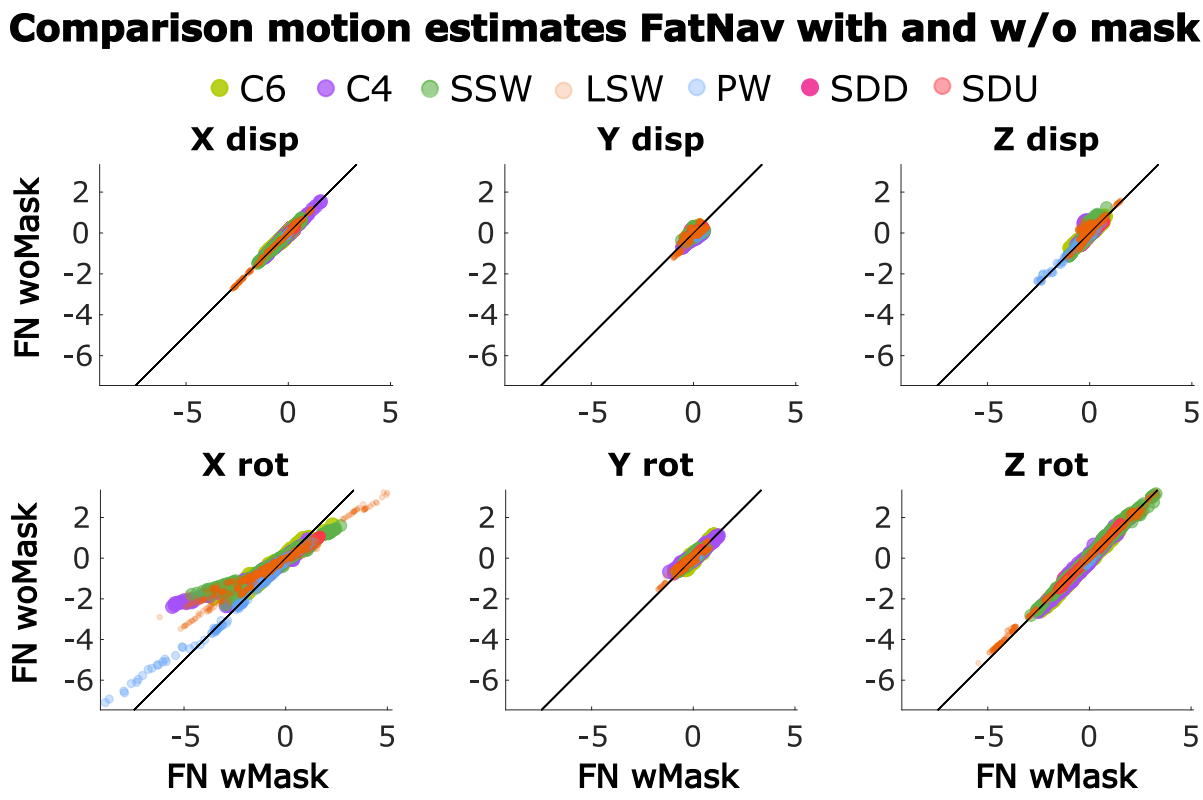

Figure 4.3.11: Comparing motion estimates from FatNavs with and without masking. Each colour represents one experiment performed for that type of motion across all subjects: PW (comprehensive of small, medium and large pitch-wise motion), SDU (slow diagonal up), SDD (slow diagonal down), C6 (circular motion at 6 cycles/min), C4 (circular motion at 4 cycles/min), LSW (large stepwise motion) and SSW (small stepwise motion). The rotation around the x-axis (X-rot) is the only parameter where FN woMask and FN wMask noticeably deviate in their motion estimates, as made clear by the divergence of the plots from the line of identity.

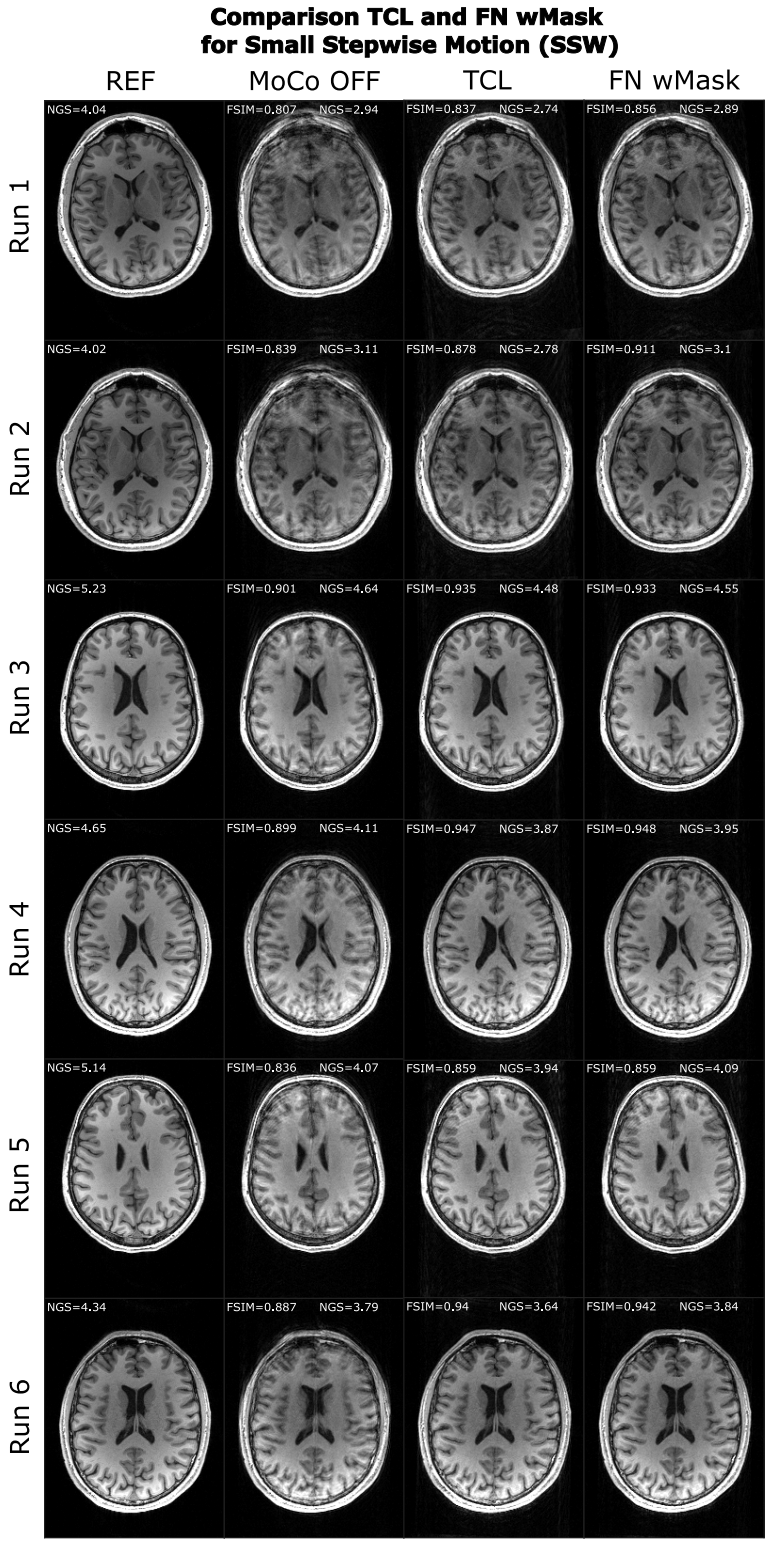

Figure 4.3.12: Uncorrected (MoCo OFF) and corrected images using TCL or FN wMask against the reference image (REF) for all runs of our small stepwise (SSW) motion scenario. Image quality metrics are reported on each image for comparison between our reference-based metric (FSIM) and our non-reference-based: NGS values imply a reduction in image quality even if improvements are clearly visible compared to the uncorrected image.

4.4 Discussion

4.4.1 Comparison between FatNavs and TCL motion correction

In this study, two tracking techniques were used to retrospectively compensate for different types of motion: small and large stepwise motion, circular motion at 4c/min and 6c/min, small, medium, and large pitch-wise motion and slow diagonal motion. Motion-estimates from both tracking methods could successfully restore image quality in the case of slow diagonal motion and small and large stepwise motion. In Frost et al. [36], stepwise motion was performed by changing head position every 1-minute, starting from the centre then looking up, down, left, right and back to the centre. Although in our study the head position changed more frequently (every 35 s) and moved also along the two diagonals, both studies showed good results in improving the image quality.

Both FatNavs and TCL methods struggled to allow the restoration of good image quality in the case of circular motion: the FSIM-based image quality metric even decreased after TCL motion correction in some cases despite the high sampling rate ($\sim$30 Hz) compared to FatNavs ($\sim$0.4 Hz). This might be caused by extensive violations of the Nyquist criterion due to the head rotations involved, which could not be compensated by the single-step NUFFT-based retrospective reconstruction. It is possible that iterative methods for applying the motion correction, such as autofocusing algorithms, could complement the motion tracking system and may help to reduce some of these residual artifacts, as suggested by Atkinson *et al.* [43]. Prospective motion correction using the TCL camera has been successfully used to compensate motion artifacts derived from the so-called "continuous" motion scenario [36], consisting in circular head motion at 1, 4 and 6 cycles/minute. The same experiments have been performed in Slipsager et al. [47], using both prospective and retrospective motion correction. However, these studies are not directly comparable with our results, as continuous motion was performed only for 1 minute during the centre of k-space sampling, against the 3 minutes proposed in this study (at the beginning, centre and end of the acquisition), which might have increased the amount of motion and therefore artifacts affecting the images. Moreover, prospective motion correction using the estimates from the TCL tracking device has been recently demonstrated to be more robust to motion artifacts compared to retrospective motion correction [47]: because of the reduced local effect of Nyquist violation, prospective motion correction could be beneficial in the case of strong head rotations, which were not fully compensated by both FatNavs and TCL retrospective motion correction. Future studies will investigate the sampling rate required to accurately estimate head position changes per different motion scenarios, as our results suggested that none of the investigated motion scenarios fully exploited the fast-sampling rate allowed by the TCL device.

4.4.2 Improving FatNavs motion estimation

In this study, we also demonstrated that FatNavs estimation accuracy can be improved by masking the non-rigid part of the neck especially when large pitch-wise motion is involved (our stepwise motion scenarios): Figure 4.3.2 shows how the mask improved the quality of the MPRAGE image especially in anterior regions of the brain.
Looking at Figure 4.3.1, we can see that, in only two experiments involving circular motion, the FSIM measure of image quality obtained after masking was slightly lower than the original FatNavs' correction and the uncorrected image. However, an inspection of the three volumes did not detect any visually perceived difference in the image quality. Another example is shown in Figure 4.4.1: the dissimilarities in the FSIM metric values are attributed to being due to the strong background noise arising after the motion correction. In all other cases, the masked FatNavs provided motion estimates that gave a corrected image at least as good as using the original FatNavs.

4.4.3 Smoothing TCL motion parameters

The TCL data displayed high frequency noise in the original motion parameters, which was likely due to limited light conditions and thus the fluctuations in pixel intensities from the camera images. The TCL motion parameters were therefore smoothed by using a moving average filter, which replaces each value for the mean across the samples included in the filter's window (99 samples in our case). The filter was found to remove all the unwanted high frequency fluctuations visible on the initial motion traces (Figure 4.3.9), and provided some improvements in the tracking accuracy, as showed for all runs of circular motion in Figure 4.3.8. However, our results also suggested that the filter did not substantially affect the overall image quality in our motion scenarios. It is possible that the use of a smoothing filter would be more beneficial in case of strong and continuous motion throughout the acquisition, where the noise would be the main contribution of tracking inaccuracy. In this scenario, the retrospective motion correction has been demonstrated to be more robust against tracking noise compared to prospective motion correction, as well as allowing for retrospective tracking compensation: a more compelling solution would then be to combine retrospective and prospective motion correction to achieve robustness against Nyquist violations and tracking noise [47].

4.4.4 Motion quantification

Overall, it was found that TCL-based motion estimates tended to be larger in magnitude than FatNav-based estimates. Despite this difference, the image quality metrics estimated for TCL and FatNavs were found overall to be quite similar, indicating that we cannot easily determine from our data which estimates are a better representation of the "true" motion. This effect

is most easily recognised in the small and large stepwise motion categories, where TCL shows larger motion scores compared to FatNavs (e.g. in runs 1, 2, 3, and 5 of the small stepwise motion in Figure 4.3.10), whereas Figure 4.3.1 shows that there is no consistent difference between the FSIM scores of the images corrected by these motion estimates.
FatNavs motion parameters are characterized by zero-motion time point placed in the centre of the acquisition, as it is the time point with lowest discrepancy between image with and without motion correction. TCL motion parameters were therefore re-centred, using SPM [78] affine transformation, at the same time point as FatNavs, to allow a comparison between the two methods. Discrepancies in the motion estimates around that time-point will generate a visual shift of the motion traces. This effect is noticeable in Figure 4.3.4, where TCL estimates look shifted compared to FatNavs. However, this effect is not expected to influence neither the motion-correction procedure nor the motion-score estimation, as the latter is based on frame-to-frame motion. Overall, it was found that TCL-based motion estimates tended to be larger in magnitude than FatNav-based estimates. Despite this difference, the image quality metrics estimated for TCL and FatNavs were found overall to be quite similar, indicating that we cannot easily determine from our data which estimates are a better representation of the "true" motion. Figure 4.4.2 shows that for circular motion, we get a good agreement between TCL and FatNav motion estimates for 'X rotations', but all other axes are less clear-cut. We therefore suspect that the discrepancies we see here in Y and Z rotation are largely compensated within the FOV of the TCL by the discrepancies in displacement estimates. However, as we have no 'gold-standard' measure of motion for our current experimental setup, we cannot fully determine which estimates are a better reflection of the true head motion.

4.4.5 Background ghosting artifacts

In some cases, it was found that the motion-correction led to visibly more ghosting in the image background than the uncorrected image, as shown in Figure 4.4.1: as the motion correction applied is based on estimated motion parameters which might not fully reflect the real motion occurred, discrepancies can arise in the k-space, leading to the appeared ghosting artifacts. We believe this ghosting may also be affecting the interpretation of the FSIM metric: the TCL correction shown in Figure 4.4.1 seemed to lead to a reduction in the image quality based on the FSIM value, despite visible improvements in the image sharpness.

To determine the effect of background ghosting to our image quality metric, we compared the FSIM values of all our images with and without applying a 2D background mask. This mask was based on a threshold value which was used to create a convex hull, that contained all the points included after the thresholding. The convex hull was slightly dilated to be sure to retain the CSF/brain boundary. The mask was then applied to the 30 central slices of each volume over which the FSIM was estimated. The results obtained from a Mann-Whitney U-test

(MATLAB function *ranksum*) demonstrated that applying a mask to the image background did not provide a significant difference in the FSIM values as shown in Figure 4.4.3 ($U = 340.5$, $p = 0.78$ for FatNav wMask and $U = 338.5$, $p = 0.83$ for TCL), concluding that the ghosting in the background did not influence the quality metric chosen. As extremely strong background noise was limited only to a few cases of circular motion, it is possible that no significant result would emerge from a statistical test. We therefore analysed whether the mask could potentially make a difference in only those cases where the background ghosting was extremely strong. This was performed by firstly estimating the signal power of the background region, which would be cut off by the head mask, as the ratio between the sum-of-squares of the background and the overall signal. The estimated background power and the difference between the FSIM values with and without mask were shown to correlate significantly (MATLAB function corrcoef, $r(18) = 0.5$, $p = 0.02$), demonstrating that the stronger the background noise the more the FSIM metric would increase if a background mask was applied. Figure 4.4.4 compares the FSIM values after applying the background mask to the same images previously showed in Figure 4.4.1: both FatNavs and TCL correction resulted in an improved image quality based on the FSIM, which was not detected when the mask was not applied.

4.4.6 Image quality assessment

In this study, we found that the FSIM reference-based metric could give a good indication of the true image quality – generally also agreeing with subjective visual assessment. In our data, the NGS quality metric showed an unclear behaviour in our experiments, with changes in its scores not seeming to correlate with what visually seemed like a good improvement from the uncorrected to the corrected image, as shown for small stepwise, circular and slow diagonal motion cases reported on Figure 4.3.3, 4.3.4 and 4.3.5 respectively. Figure 4.4.5 compares the values from FSIM and NGS for FatNavs with mask and TCL in case of small stepwise motion. In all our runs, both FatNavs and TCL improved the image quality, as pointed out by the FSIM values being higher than the uncorrected images' ones for all tracking techniques. This was further corroborated by a visual check of all images, which displayed a qualitatively higher level of sharpness compared to when no motion correction was applied (Figure 4.3.12). On the other hand, NGS value altered in the opposite way to what would be expected in all but one run. Further studies will need to be performed to assess the correlation between metrics used to estimate brain MR images quality and radiologist evaluations, which is still to be considered the standard reference. Moreover, additional research is needed to evaluate how these metrics are affected by different artifacts: our results suggest that metrics such as the NGS may not be optimal metrics for driving automated motion-correction techniques, as we have several examples of a visually "better" image that scores "worse" when judged by NGS.

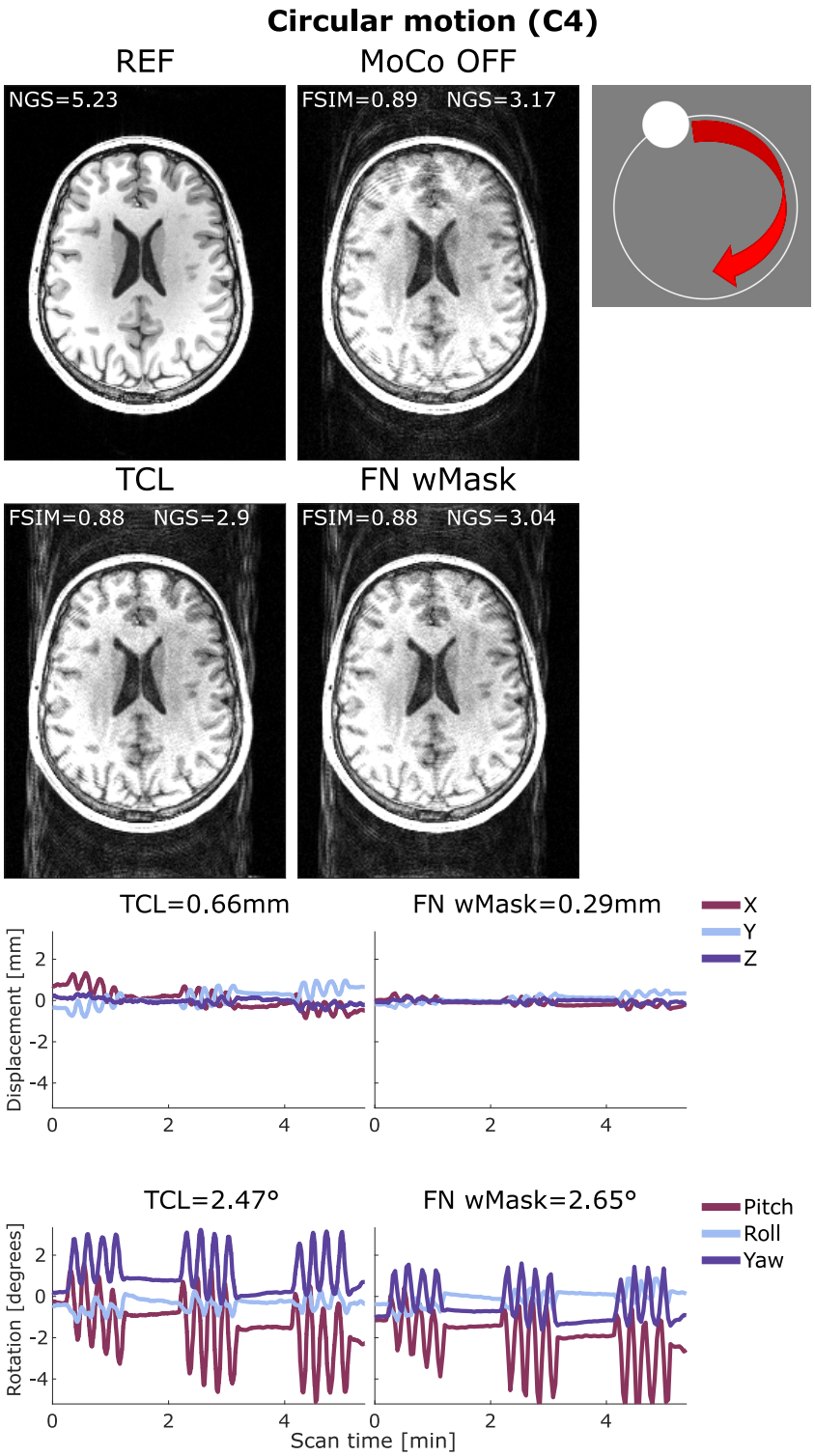

Figure 4.4.1: (A) Comparison between reference (Ref), uncorrected (MoCo OFF), and the corrected images (TCL and FN wMask) for circular motion at 4 cycles/min (FC4): the corrected images are affected by strong background ghosting which is not present in the uncorrected image. Images in this figure have been windowed to allow easier visualization of the ghosting rather than optimal viewing of grey/white contrast across the brain. (B) Motion parameters are reported for TCL and FN wMask, with the RMS value reported on top of each motion trace for translations (in mm) and rotations (in degrees).

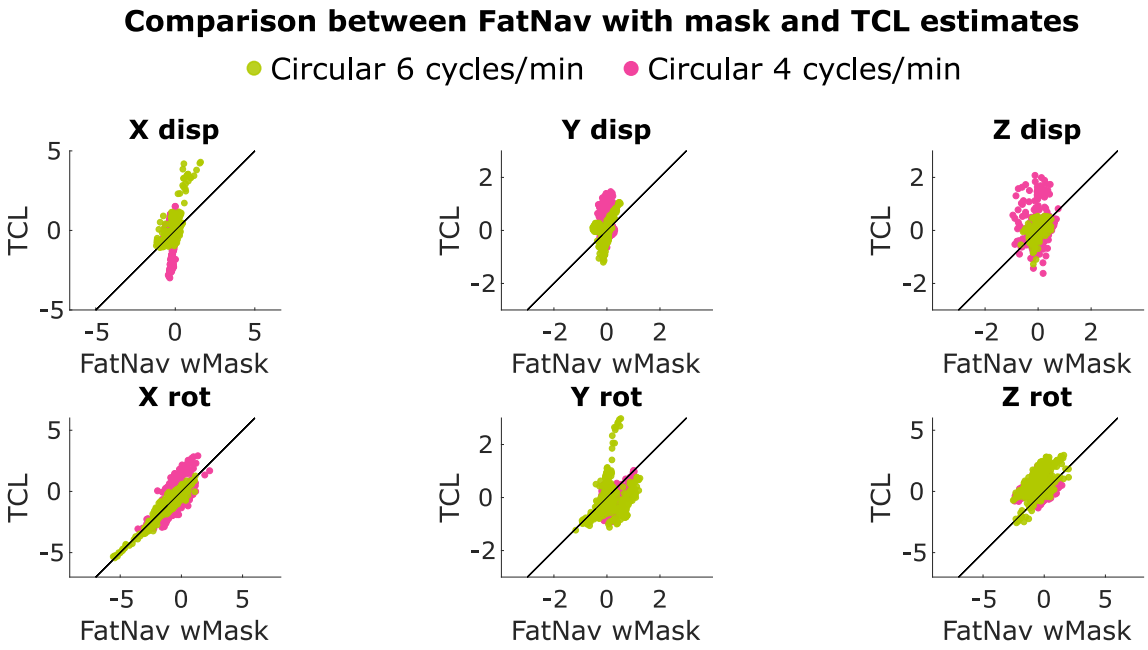

Figure 4.4.2: Comparison TCL and FatNav motion parameters for all our motion scenarios across the three axis for rotations and translations. The dots' deviation from the diagonal indicates differences in the motion parameters estimated by the two tracking systems, with the strongest differences detected along the x-axis for translations and y-axis for rotations.

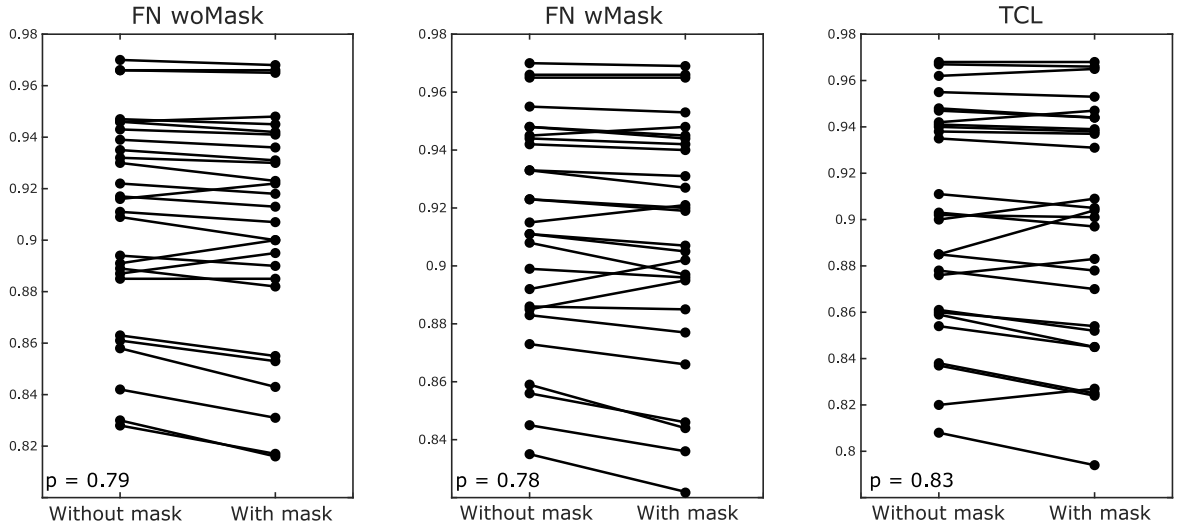

Figure 4.4.3: Result of two samples data Mann-Whitney U-test performed between the FSIM values of the images without masking the background (Without mask) and masking the image background (With mask) for FN woMask, FN wMask and TCL. The p-values for the three tests are reported on each image.

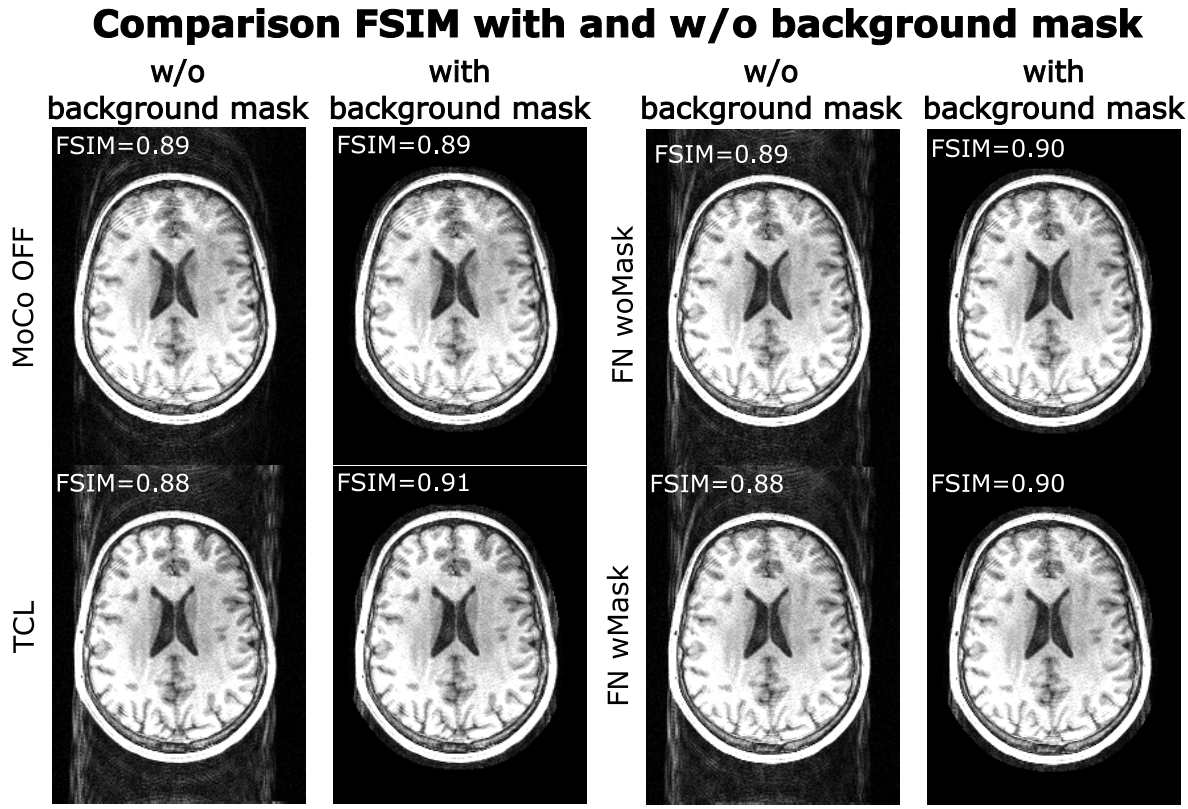

Figure 4.4.4: Comparison between the FSIM values of images affected by circular motion (C4), showed in Figure 4.4.1, without (w/o background mask) and with masking the image background (with background mask) in case of TCL, FN woMask and FN wMask motion correction and without motion correction (MoCo OFF).

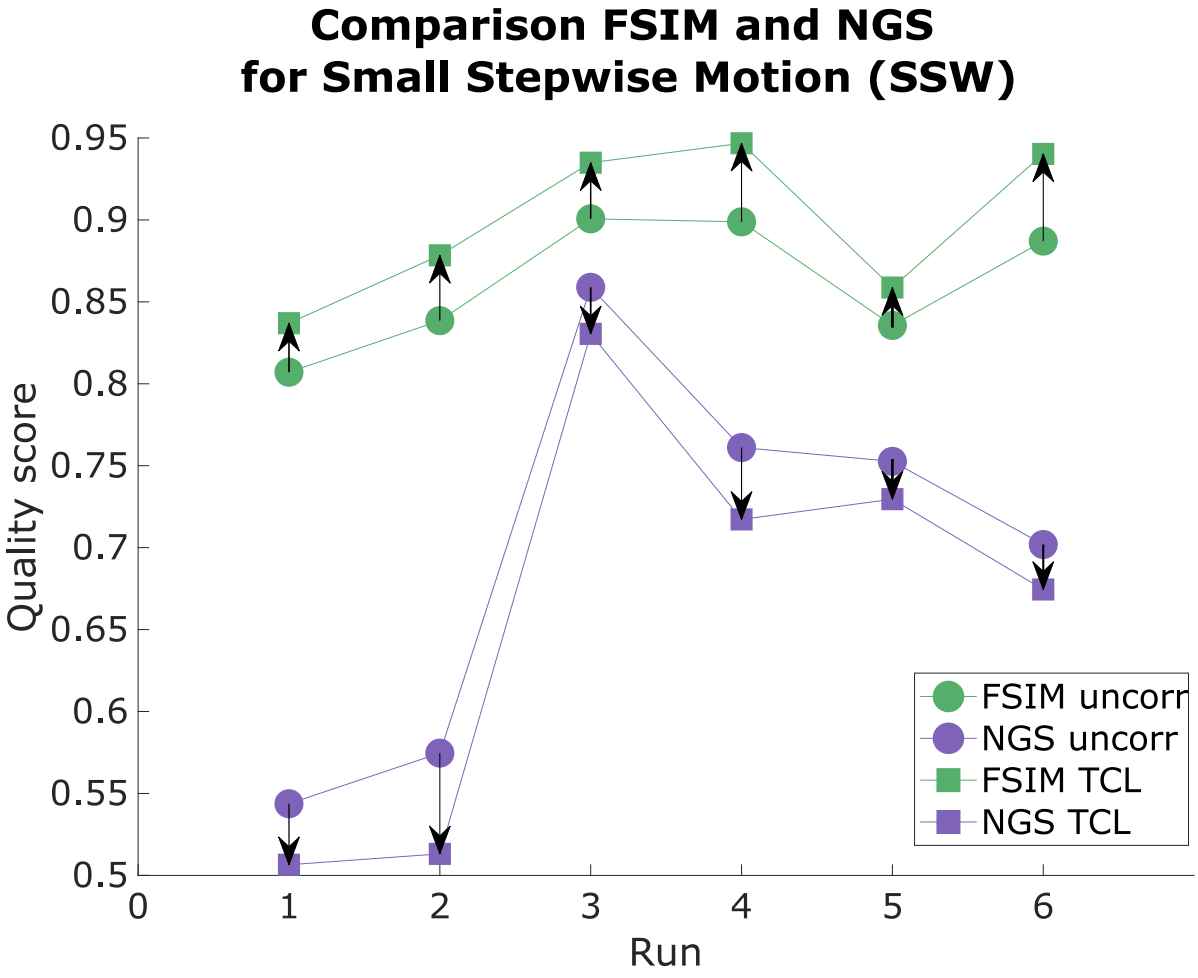

Figure 4.4.5: Comparison of FSIM and NGS image quality metrics values for each run of small stepwise motion estimates from TCL tracking device. Both metrics were first normalized between 0-1 and the mean value across runs of the experiment subtracted for each metric for display purposes. The circle markers represent the image quality metric value (FSIM in green and NGS in purple) before motion correction; the square markers indicate the metrics' values after the TCL-based motion correction. Both FSIM and NGS are expected to increase (arrow pointing up) if the image quality improves.

CHAPTER 5

Noise reduction in MRI: design and test of motion-robust pulse sequences using Pulseq.

Based on:
Elisa Marchetto, Maxim Zaitsev, Daniel Gallichan, *Rapid prototyping of a motion-robust 2D Radial GRE sequence with reduced acoustic noise generation using Pulseq*, ISMRM 30th Annual Meeting, 2022.

5.1 Introduction

The major source of acoustic noise in MRI is the electric current flowing in the gradient system: the induction effect generated by the magnetization causes *Lorentz forces*, which can result in the vibration and deformation of the gradient coils generating the unwanted MR noise. This effect has been extensively described in Section 1.2. The acoustic noise produced during an MRI scan can contribute to patients' discomfort and anxiety [24], but it also rises safety concerns when fast sequences are used, such as diffusion gradient sequences, as they reach safety limits: vulnerable patient groups as neonates and pregnant women are particularly susceptible to this kind of hazard [53]. Moreover, it may induce hearing impairment in patients who regularly undergo MRI examinations [25]. Various solutions are currently available to apply acoustic noise attenuation during the MR acquisitions, which have been described in Section 1.2.6.

Neonatal scans are often performed in natural sleep in research settings. To ensure a undisrupted sleep during the scan, different active and passive strategies can be adopted to reduce the acoustic noise levels. In Dean et al. [101], the slew rate and maximum gradient magnitudes were reduced of 30% and 75% respectively, as well as changes in the pulse

sequences to soften sharp changes of the gradients. Removable sound-insulating foam insert was included as passive measure, which were rated to reduce the acoustic noise of 20 dB(A). Moreover, electrodynamic headphones with ear pads were adopted, for a further reduction of 45 dB(A). These measures allowed for an overall success rate of 97% of the scans.

In this preliminary study, we adjusted gradient timings and waveforms of a radial GRE sequence to test different strategies to reduce the acoustic noise generated when the pulse sequence is running. Designing and testing were performed using *Pulseq*, which is an open-source framework that allows rapid prototyping of pulse sequences [102]. Prospective motion correction of voluntary motion was carried out using a markerless device tracking communicating with the scanner via the *libXPACE* (*eXternal Prospective Acquisition CorrEction*) framework [103], that was linked directly to a customized Pulseq interpreter. The initial aim was to design a motion-robust and acoustically optimized sequence to acquire a single-slice MR image of the brain. The sequence was meant to be used with paediatric or infant age group, where research scans are typically conducted while the subject is sleeping.

5.2 Methods

5.2.1 Pulseq

Pulseq is an open-source framework for the design and testing of MRI and Magnetic Resonance Spectroscopy (MRS) pulse sequences [102], which allows the user to rapidly code MR sequences both in MATLAB or Python (as *PyPulseq* [104]). In this study, pulse sequences were programmed in MATLAB using Pulseq v1.4.0.

The MATLAB workflow requires the user to initially define basic system parameters such as TR, TE and FOV. System limits (e.g. maximum gradient strength and slew rate) must also be outlined. Sequences in Pulseq are defined as a concatenation of blocks: the user can add RF pulses, gradients and ADC events within each block. Each element does not have to start or end at zero at each block boundary. RF pulses and gradients can be created using Pulseq built-in functions, with the user selecting either trapezoidal or arbitrary waveforms (e.g. sinusoidal) and defining timing and shape of the gradients. Pulseq allows the user to verify the raster alignment and the k-space sampling using the built-in functions *checkTiming* and *calculateKspace* respectively. Moreover, it is possible to obtain a rough estimation of the sequence acoustic noise via the *sound* function. Once the sequence is ready, the built-in function *write* can be used to generate a *.seq* file, which can be transferred to the MR scanner. The user can visualize and select the designed Pulseq sequence (.seq file) from the scanner computer as shown in Figure 5.2.1 and run the sequence.

Via the libXPACE framework, the user can select to apply dummy sources of motion to the image (*Noise* option), coming from a noise random generator, or previously recorded motion

traces (*File* option) as shown in Figure 5.2.2. The prospective motion correction is enabled via the MPT option, using motion traces estimated via an external tracking device (e.g. Moiré phase tracking). The user can select the *Correction Level*, or correction frequency, from the options available, which are displayed in Figure 5.2.3. The *disabled* option can be selected to acquire the image without motion correction.

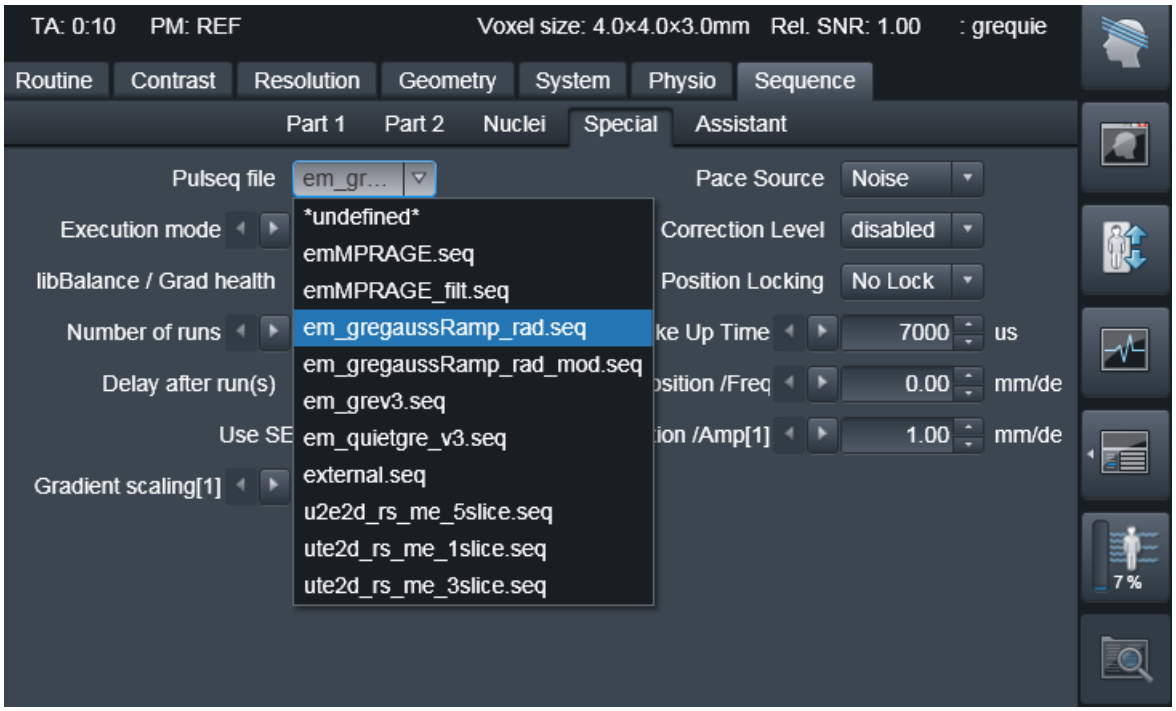

Figure 5.2.1: A list of the uploaded Pulseq sequence files. The user can then select the desired sequence and run it on the scanner.

5.2.2 Pulse sequence optimization

The next sections describe the different configurations designed to acoustically optimize a standard radial 2D GRE sequence (Original GRE).

5.2.2.1 Configuration 1: optimized trapezoidal waveform

As the slew rate is directly proportional to the acoustic noise [105], we allowed more time to ramp-up and ramp-down each gradient, without modifying their original trapezoidal waveforms. The spoiler gradient (G_x) after the readout was performed by extending the ramp-down gradient, to avoid the switching off and on of the two gradients. The slice-selection gradient was ramped more slowly, minimizing abrupt changes in the gradient's amplitude. Care was also taken to temporally align all ramps that would not affect the image encoding.

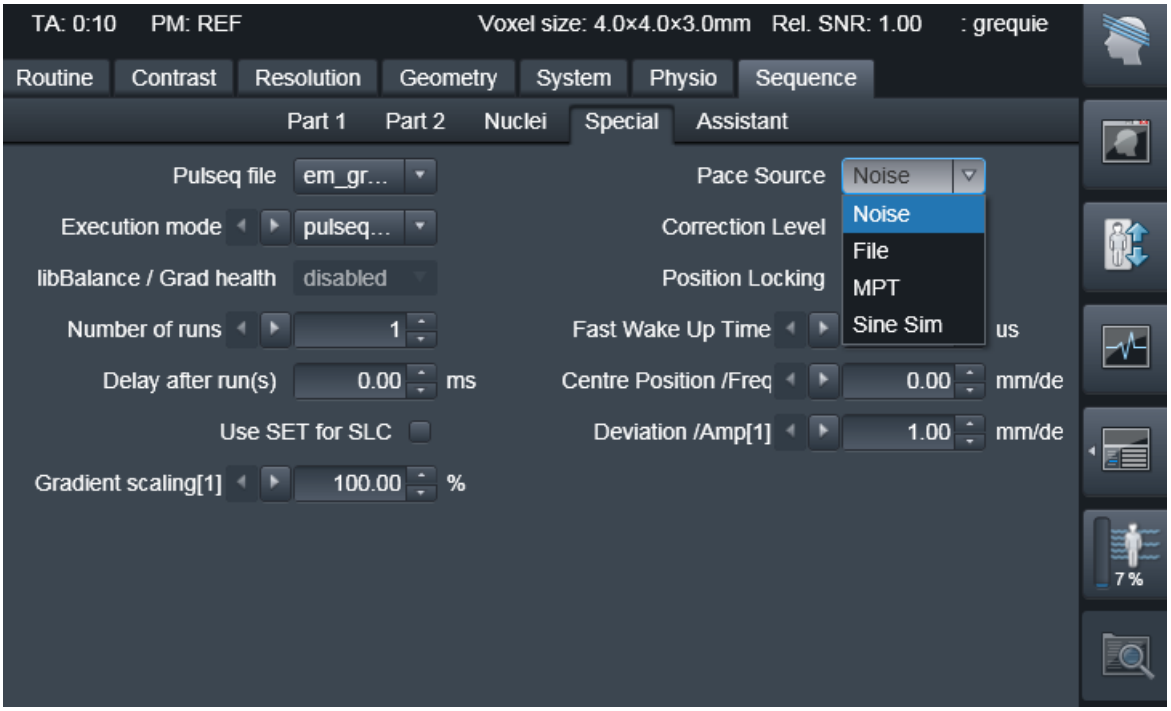

Figure 5.2.2: Correction types available via the libXPACE framework. The user can select which source of motion estimates to use for prospective motion correction.

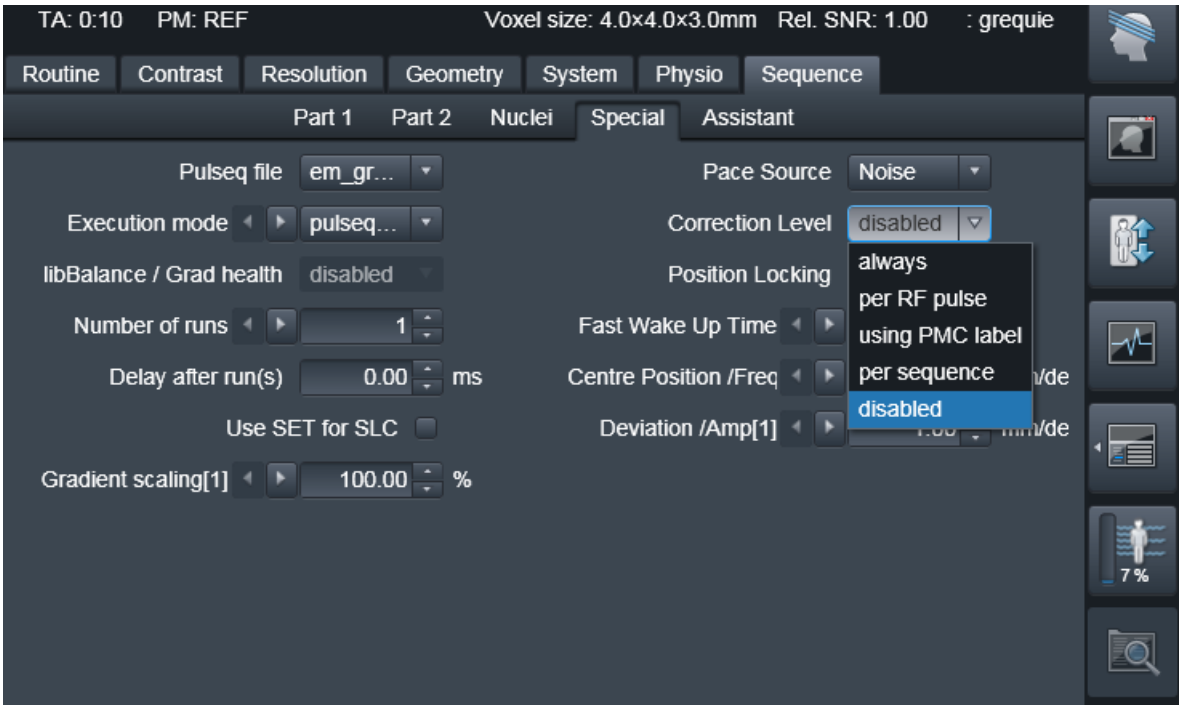

Figure 5.2.3: The "Correction Level" option allows the user to select the frequency of the correction. No motion correction is performed choosing the "disabled" option. In this work, we adopted the "per RF pulse" option when motion correction was enabled, which updates the scanner gradients once per each TR based on the motion estimates acquired.

5.2.2.2 Configuration 2: non-linear waveform

The original trapezoidal gradient waveforms were replaced with Gaussian-shaped ramps (soft gradient waveform) to further acoustically optimize the sequence. The Gaussian waveforms were used to maximize the ramps gradual ascent and descent. The gradient amplitudes were chosen based on the known gradient area required to encode the phase and frequency information without changing the flat-top time.

5.2.2.3 Configuration 3: improved configuration 2

The Configuration 2 sequence was further modified so that the spoiler gradient along the z-direction would not completely ramp-down to zero before the next excitation pulse: the spoiler gradient would slowly decrease to the same amplitude level of the next slice selection gradient. Gradient timings were aligned so that when the spoiler gradient reached that point, the following slice selection gradient would start. This configuration was expected to further reduce the acoustic noise, compared to its previous configuration, because it would avoid consecutive ramp-down and ramp-up of the spoiler and slice selection gradients respectively.

5.2.3 Experiments

All four sequences were tested on a 3T Prisma scanner (Siemens Healthcare, Erlangen, Germany) with TR/TE = 18.2/8 ms, FA = 20°, slice thickness = 3 mm and FOV = 256 mm, for a total acquisition time of TA = 10 s for a single slice. Preliminary scans were performed with a phantom to undertake acoustic-noise measurements using the *Decibel X* app (SkyPaw Co., Ltd). Decibel X is a noise meter app that allows pre-calibrated measurements via a mobile phone. It supports different filters, including an *A-Weighting* filter, which turns standard dB measurements of the sound pressure level (SPL) into dB(A), which is considered as an accurate estimation of the apparent noise levels as perceived by the human hear. Based on the standard IEC 61672-1:2013, the conversion dB to dB(A) can be performed by applying the weighting function $R_A(f)$ to the unweighted SPL:

$$R_A(f) = \frac{12194^2 f^4}{(f^2 + 20.6^2)\sqrt{(f^2 + 107.7^2)(f^2 + 737.9^2)}(f^2 + 12194^2)} \tag{5.1}$$

$$A(f) = 20log_{10}(R_A(f)) + 2.00$$

The noise was recorded from a mobile phone device positioned at the entrance of the scanner room for safety reasons. The phone was not touched or moved from its position for the entire duration of the recording. The mean of the acoustic noise was calculated within the sequence

running time (10 s)
The original sequence and its first optimization (Configuration 1) were tested in vivo with the participant performing slow back-and-forth head rotation, with and without motion correction enabled. A separate 2D slice was collected without deliberate motion as reference. The motion parameters were estimated using the Tracoline (TCL) markerless device; the real-time motion-tracking updates were sent to the scanner once every TR (*per RF pulse* option in Figure 5.2.3) via the libXPACE framework, to allow prospective motion correction. A cross calibration step was performed to align the tracking and the scanner coordinate system through a semi-automatic cross calibration tool using an MPRAGE scan collected without deliberate motion prior the main acquisition [106]. Image reconstruction was performed in MATLAB using the Pulseq reconstruction script, which recognizes and analyse the trajectory from the generated .seq file and performs the reconstruction.

5.3 Results

5.3.1 Configuration 1: optimized trapezoidal waveform

Figure 5.3.1 compares the gradients along the x- and z-direction of the original GRE sequence and of its first acoustically optimized configuration. The readout gradient (G_x) ramp-up time was increased from 50 μs to 500 μs, while the spoiler gradient magnitude was significantly reduced by extending the readout gradient area and ramped it down more slowly. The rephaser gradient (G_z) was allowed to ramp-down more slowly (from 110 μs to 610 μs) and timed to end up in zero at the beginning of the k-space readout. The spoiler gradient magnitude along the z-direction was also greatly reduced by increasing the ramp-up and ramp-down times.
The results from the acoustic noise test performed using the Decibel X app from a mobile phone are reported in Figure 5.3.2: the acoustically optimized Configuration 1 reduced the averaged acoustic noise of 5 dB(A) compared to the original GRE sequence (from 68.9 dB(A) to 63.9 dB(A)). The maximum noise peak also decreased from 69.5 dB(A) to 65.3 dB(A).

5.3.2 Configuration 2: non-linear waveform

Configuration 2 was generated by substituting all the linear ramps of the acoustically optimized Configuration 1 sequence with Gaussian waveforms. A comparison between Configuration 1 and Configuration 2 is illustrated in Figure 5.3.3: the magnitude of the rephaser and the spoiler gradients along the z-direction were automatically reduced by using the Gaussian waveforms. On the other hand, the amplitude of the prephaser gradient (G_x) was increased to correctly encode the frequency information. Nevertheless, the Configuration 2 is shown to lead to

a further acoustic noise reduction of more than 4 dB(A), from 63.9 dB(A) to 59.7 dB(A), compared to the trapezoidal Configuration 1. The maximum noise peak also decreased from 65.3 dB(A) to 62.7 dB(A).

5.3.3 Configuration 3: improved configuration 2

A comparison between Configuration 2 and 3 is shown in Figure 5.3.5. In the Configuration 3, the first slice selection gradient was generated starting from the second TR, to allow for the first spoiler gradient to ramp-down to magnitude level of the following slice selection gradient. Therefore, no ADC event was performed during the first TR. Configuration 3 provided a reduction in the average acoustic noise level of almost 1 dB(A) compared to Configuration 2 (from 59.7 dB(A) to 58.1 dB(A)), as shown in Figure 5.3.6. Furthermore, the maximum noise peak decreased from 62.7 dB(A) to 61.8 dB(A).

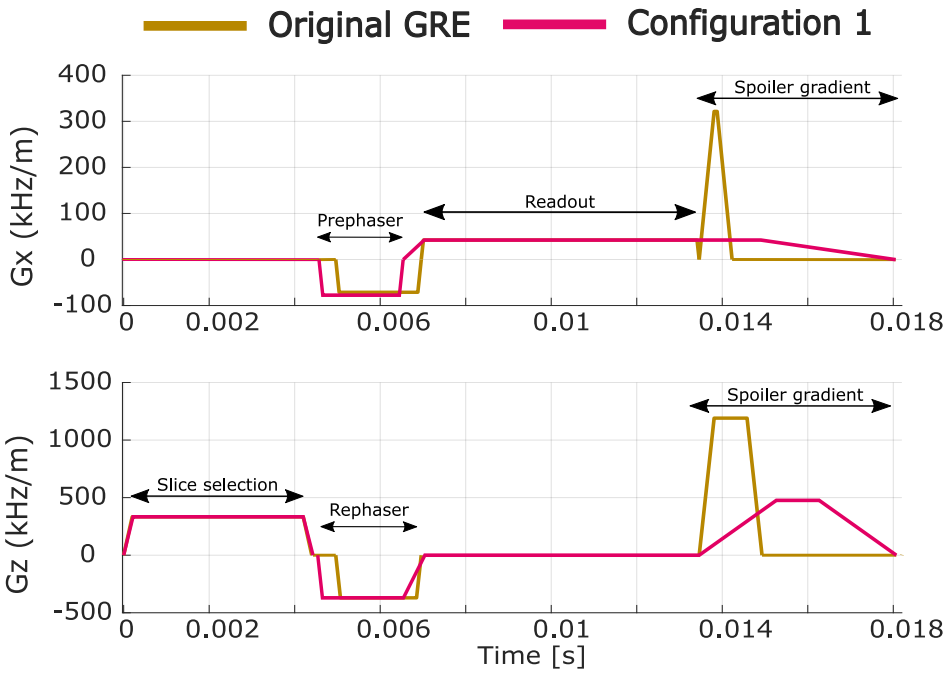

Figure 5.3.1: Comparison between the gradients along the x- and z-axis of the original GRE and Configuration 1 (with acoustically optimized trapezoidal waveforms) sequences during one single TR. The phase-encoding gradient (G_y) is not displayed to simplify the comparison. The readout gradient ramp-up time was increased, while the rephaser gradient was ramped-down more slowly compared to its original configuration. The magnitude of both spoiler gradients (along x and z) were substantially reduced.

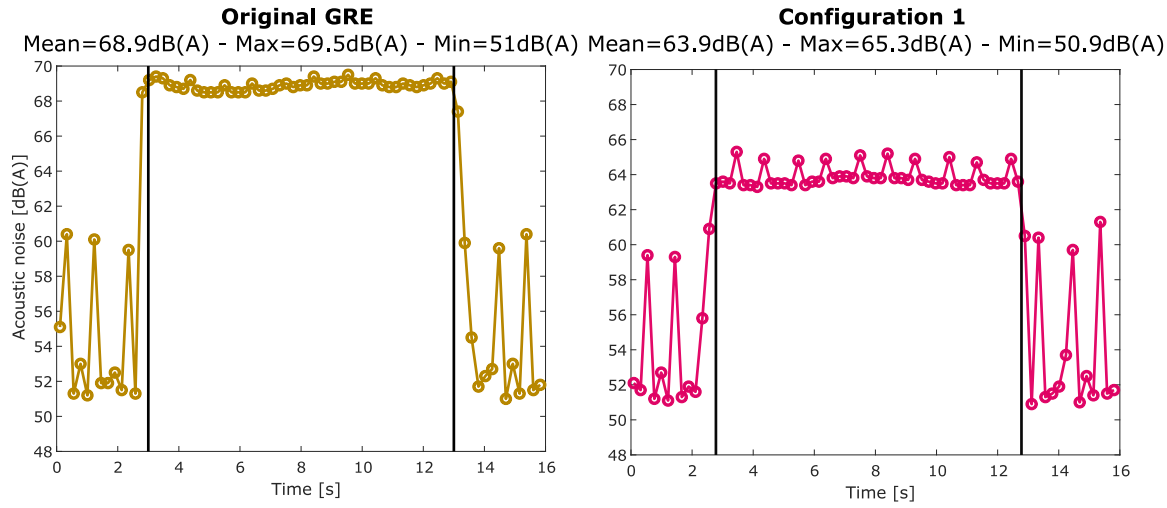

Figure 5.3.2: Comparison of the sound waves acquired from the Original GRE and Configuration 1 sequences via the Decibel X app using a mobile phone positioned at the entrance of the scanner room. The Configuration 1 allowed for a substantial reduction in the mean noise of 5 dB(A) compared to the Original GRE configuration. The mean value was found by averaging the values within the time range when the sequence was running, indicated by the two black vertical lines. The spikes visible at the beginning and at the end of the acquisition (before and after the black lines) are caused by the noise of the scanner cooling system.

5.3.4 In-vivo tests

Figure 5.3.8 compares images acquired with and without motion correction against a reference images for the original GRE and the Configuration 1, with reasonable image contrast obtained for both sequences. The motion parameters measured by the tracking device during the experiments with and without motion correction are reported in Figure 5.3.7 together with the corresponding RMS values for translations and rotations: the results show that the participant moved slightly more during the acquisition using the acoustically optimized sequence, both with and without motion correction in place. Nevertheless, the prospective motion correction worked nicely with both sequences, improving the image quality as corroborated by the FSIM image quality score [87] reported on each image.

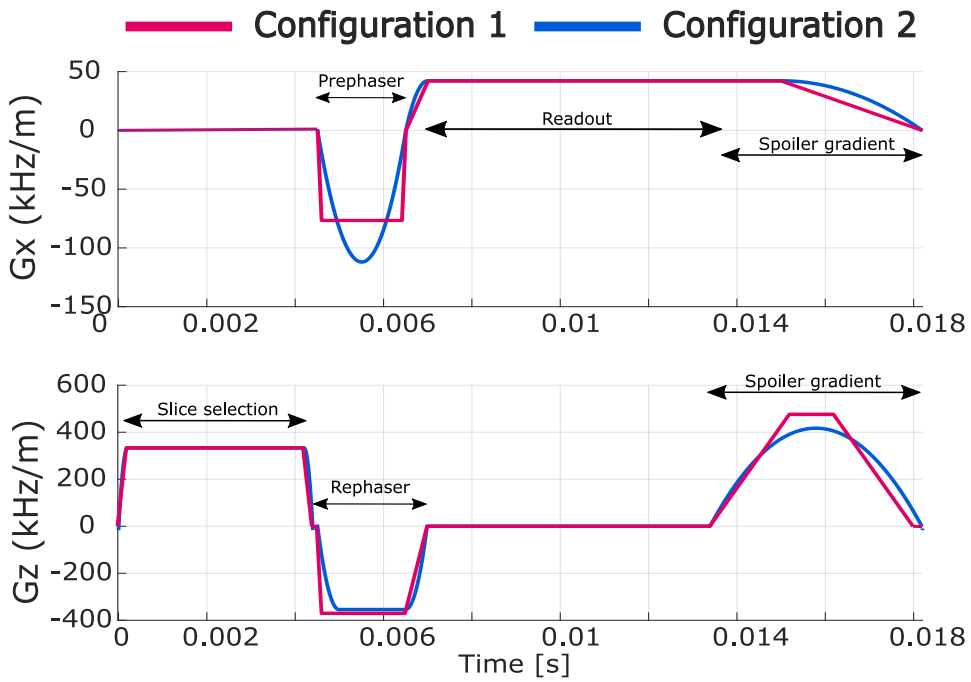

Figure 5.3.3: Comparison between the optimized Configuration 1 (with trapezoidal waveforms) and the Configuration 2 (with Gaussian waveforms). The amplitude of the prephaser gradient had to be increased to maintain the same gradient area compared to its trapezoidal configuration. On the other hand, the magnitude of the rephaser and spoiler gradients on the z-axis could be slightly reduced, as the Gaussian ramps partially compensated for the area required to correctly encode the spatial information.

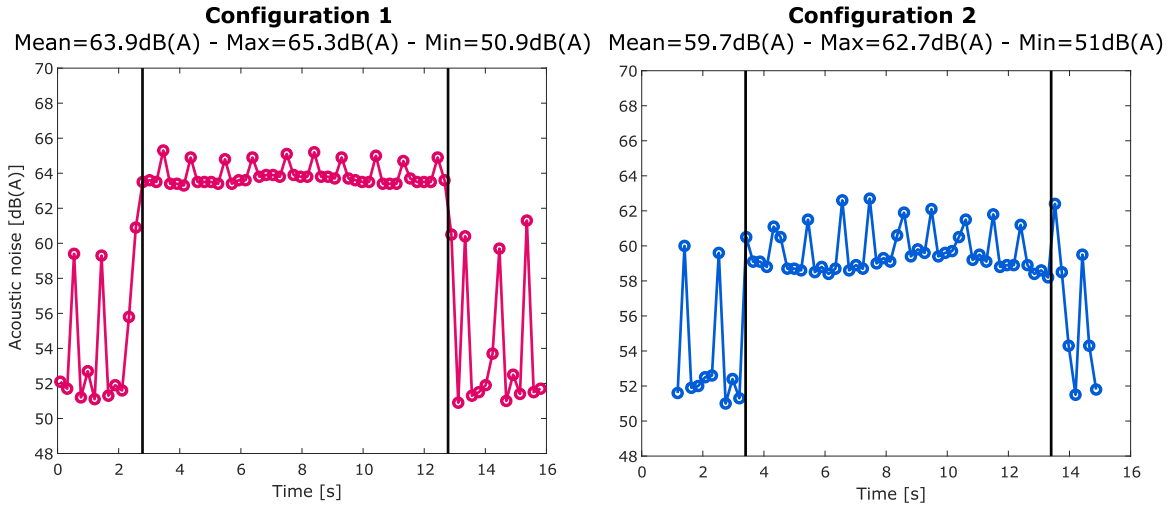

Figure 5.3.4: Comparison of the sound waves measured from the Configurations 1 and 2 sequences. Despite the prephaser gradient magnitude being higher compared to the Configuration 1 (Figure 5.3.3), using Gaussian waveforms helped reducing the average acoustic noise further, as well as the maximum and the minimum sound peaks, compared to the trapezoidal configuration. The black vertical lines indicate the beginning and end of each sequence.

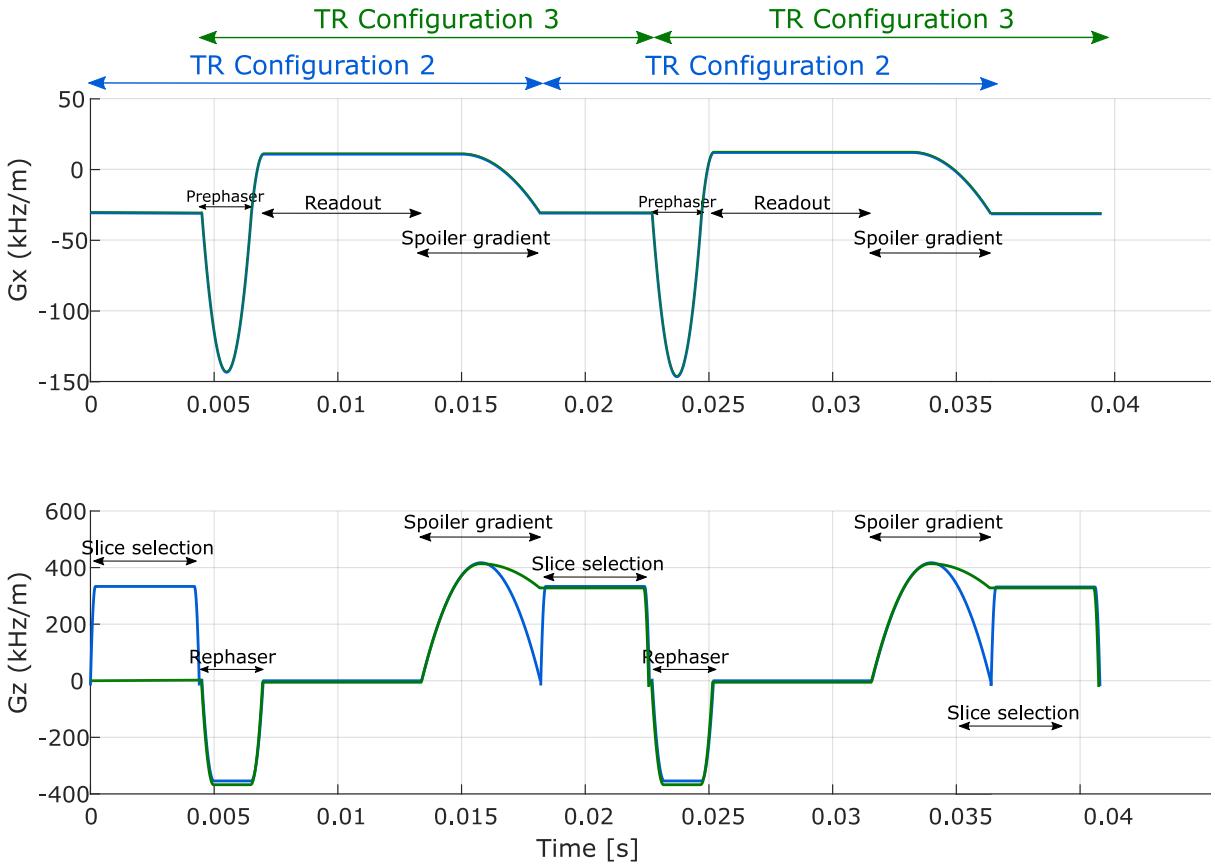

Figure 5.3.5: Comparison between Configurations 2 and 3: the only modification performed was to ramp-down the spoiler gradient along the z-direction to the same magnitude of the consecutive slice selection gradient, with the aim of reducing the acoustic noise caused by a complete gradient ramp-down and the following slice-selection ramp-up. The gradient events performed along the x-axis were identical for the two configurations. No ADC event was performed during the first readout of the Configuration 3, as the first slice selection gradient was generated at the end of the first TR.

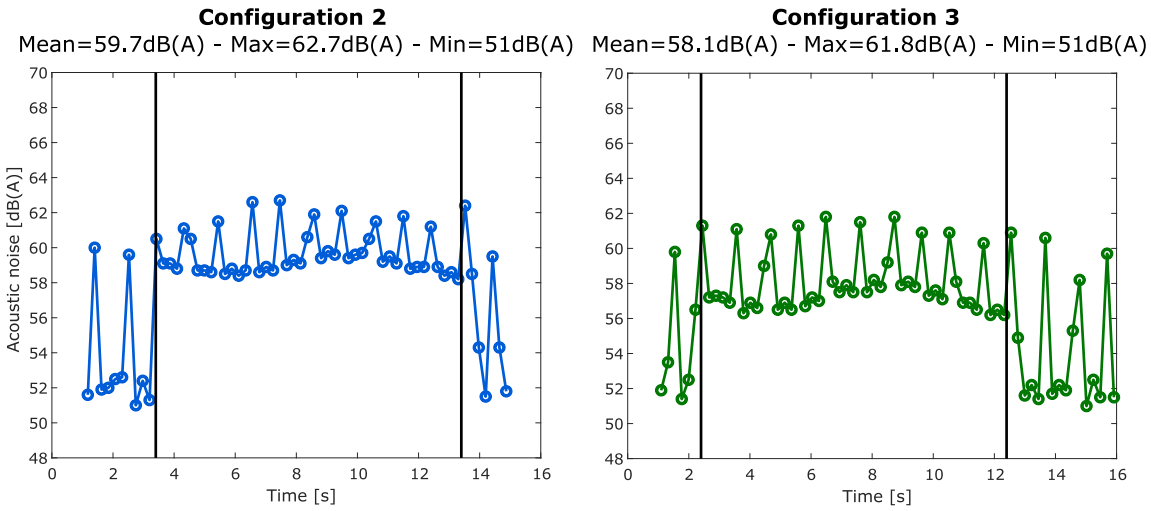

Figure 5.3.6: Comparison of the sound waves from the Configurations 2 and 3. Not ramping down the spoiler gradient along the z-direction (Configuration 3) allowed for a reduction in the averaged acoustic noise of almost 1 dB(A). The maximum noise peak also decreased from 62.7 dB(A) to 61.8 dB(A)). The black vertical lines indicate the beginning and end of the sequences.

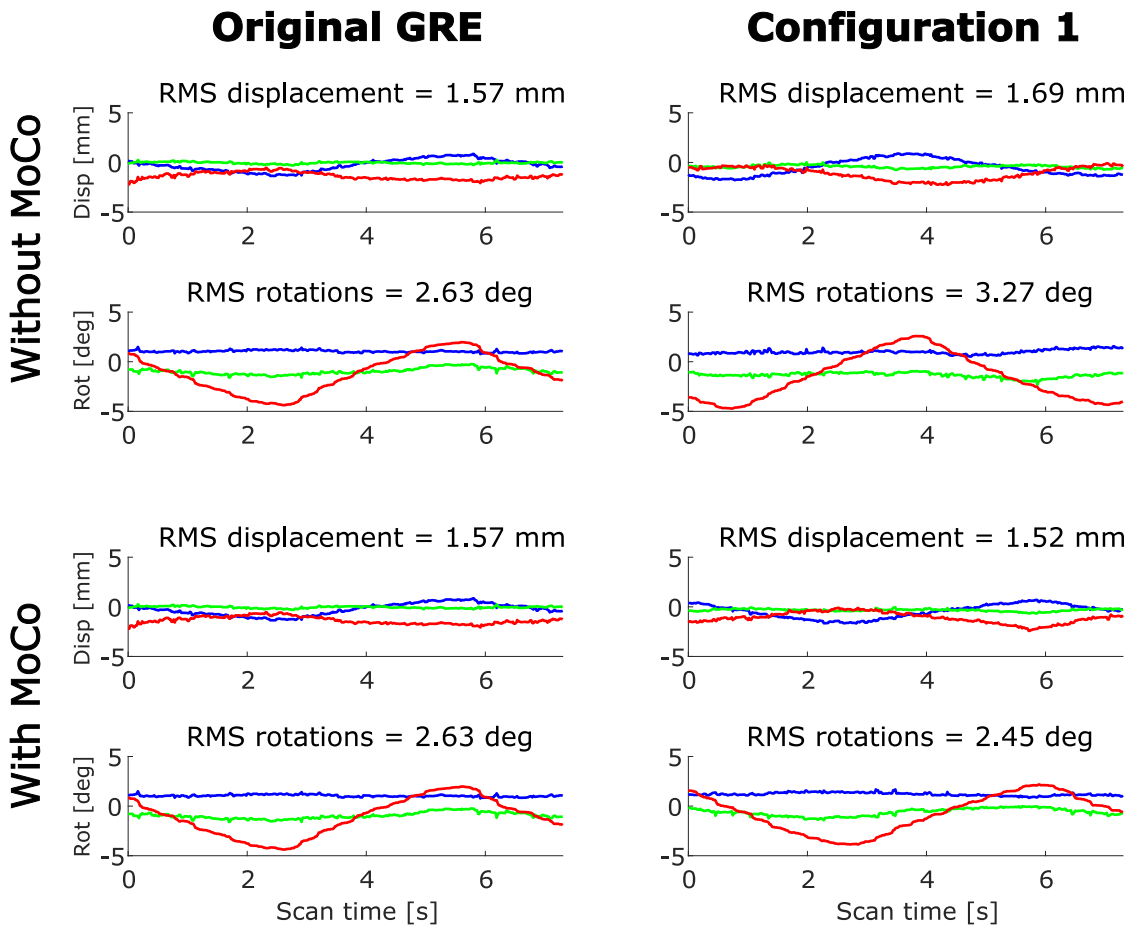

Figure 5.3.7: Motion parameters obtained by the TCL tracking device without and with motion correction (without MoCo and with MoCo respectively) for the original GRE sequence and its first acoustically optimized configuration.

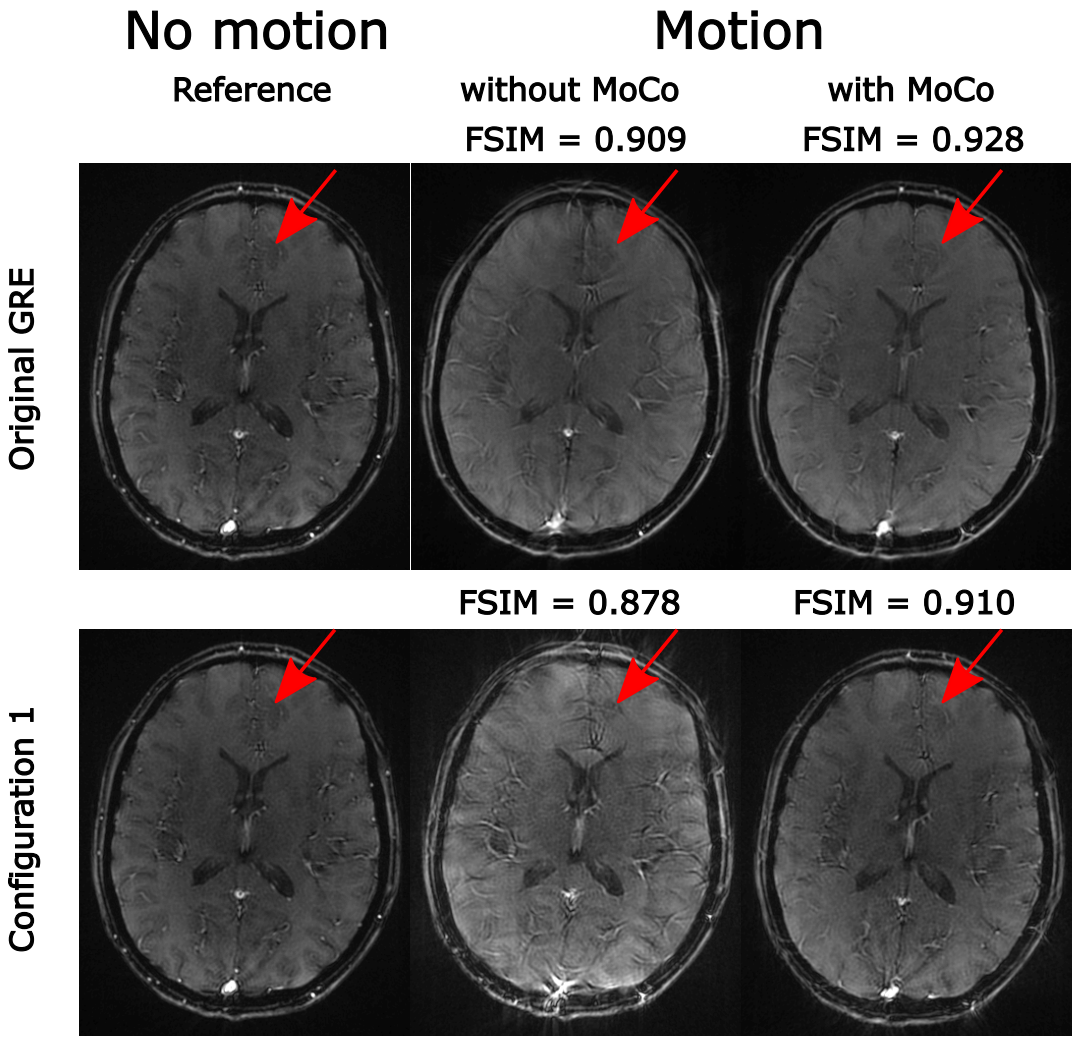

Figure 5.3.8: Comparison between prospective motion corrected images (with MoCo) and without motion correction (without MoCo) acquired using the original GRE and the acoustically optimized Configuration 1 (with trapezoidal gradient waveforms) sequences. Motion-free scan without motion correction is reported here as reference image. The motion correction improved the image sharpness compared to the uncorrected images, especially in the region above the CSF as indicated by red arrows.

5.4 Discussion

In this study, we designed and tested different acoustically optimized configurations of a GRE sequence using Pulseq, to reduce the acoustic noise produced by the MR sequence. The noise measurement performed on Configuration 1 showed a noise reduction of around 5 dB(A) compared to the Original GRE sequence (Figure 5.3.2), by applying slower rising and falling of gradients as well as optimization of spoiler gradient areas (Figure 5.3.1). A further acoustic noise reduction was obtained by substituting the classical trapezoidal gradients' ramps with Gaussian waveforms (Configuration 2), as shown in Figure 5.3.3: despite the increased prephaser magnitude, the Configuration 2 showed a decrease in the average sequence noise of around 4 dB(A) compared to Configuration 1, due to the inherently gradual ramping attributed to "soft" gradient waveforms, and to the reduction in the spoiler gradient magnitude along the slice selection gradient direction (G_z). The sinusoidal waveform has been used in previous studies to reduce the acoustic noise produced by the gradients ramps as its "soft" behaviour allows for a reduction in the acoustic noise function range [61]. However, a direct comparison between using a Gaussian or a sinusoidal waveform have not been performed yet, and would be explored in future studies.

Configurations 2 and 3 are characterized by the same gradient timings and shape, with the only difference that the spoiler gradient, applied along the z dimension, was not ramped down to zero before the beginning of the next TR; instead, the ramp was gradually decreased to the same gradient magnitude of the following slice selection gradient. This configuration provided a further reduction of almost 1 dB(A) in the acoustic noise level. The maximum peak value of the Configuration 3 decreased of around 1 dB(A) as well. On the other hand, the minimum sound noise produced by the scanner helium cooling system was the same for all configurations, with a value around 51 dB(A). Future study will require the use of a calibrated MR safe equipment at the entrance of the scanner bore, where the strongest noise can be measured [55]. Moreover, it would be preferable to also conduct the acoustic experiments with the chiller pump temporarily switched off. The consistent results we observed with the current hardware setup suggest that it is sufficient for obtaining indicative estimates of dB(A) improvements with different pulse sequence modifications. The reader can find the audio files of the original and three optimized configurations here: Audio files.

Prospective motion correction was enabled via the libXPACE framework, using the motion parameters measured by an external tracking device. The motion parameters tracked by the TCL device show that the motion performed by the subject has comparable magnitude, although differing in the shape depending on at what moment of the back-and-forth head motion the scan took place (Figure 5.3.7). For this proof-of-concept study, the motion correction was tested successfully for one single slice acquisition: further study will investigate the motion correction robustness in the case of multi-slice acquisitions. Even in the images where no motion correction was applied, some fine anatomical features can still be recognized.

This is attributed to the inherent robustness of radial sampling to motion, where motion artifacts tend to be less severe than for Cartesian sampling. Nonetheless, prospectively corrected images show substantially higher level of detail than when no motion correction was applied.

In this study, we increased the TR of a radial GRE sequence from 15 ms to 18.2 ms, causing an increase in the time required to acquire a full 2D slice (from around 9 s to 11 s). This increase in the TR time rise a concern related to the motion sensitivity of the sequence. However, the quiet configurations tested in this study significantly reduced the sound pressure level produced by the three sequences, which was shown to improve the overall experience of participants undergoing an MR scan [25], which would translate in less subject's motion affecting the image. Moreover, neonatal scanning are usually performed in natural sleep in research settings: quiet sequences can then be crucial to reduce the risk of disrupted sleep which might affect the success of the scan itself [101].

The aim of this proof of concept study was to show how to quickly design and test a motion robust and acoustically optimized MR pulse sequence to acquire brain MR images of infants subjects, taking advantage of the acoustic noise reduction especially when no sedation or anaesthesia are used. The sequence was shown to be motion robust even without the prospective motion correction enabled due to the radial sampling, which could be advantageous compared to standard Cartesian sequences (e.g. PETRA) in case of small movements that could still occur during neonatal sleep [101]. However, the sequence is still at an initial prototype stage as it is currently limited to a single 2D slice acquisition. The three configurations tested were indeed found to considerably decrease the acoustic noise of the original sequence; however, the noise produced by the baseline GRE sequence was already not as high as for some other commonly used sequences – but was chosen for its simplicity in testing the approach to rapid design of motion-corrected pulse sequences. Future work will attempt to apply the same strategies introduced in this experiment to reduce the acoustic noise produced during the GRE train of an MPRAGE sequence, where the noise level has been found to be around 87.4 dB(A) at 3T, measured using a microphone placed at a distance of 2.5 m from the front panel of the MR imaging scanner [58].

CHAPTER 6

Conclusions and future work

Motion artifacts can cause extensive degradation of MRI images, making them unsuited for clinical or research purposes. Motion correction can help reduce the need for rescan, help improve the scan experience for the participant as well as the image quality.
This thesis has explored different motion correction methods to maximize the image quality of brain MR images in different motion scenarios. This chapter summarises the main outputs of our investigation, and discusses some recommendations for future work.

6.1 Autofocusing

Autofocusing motion correction techniques do not use any previous knowledge coming from navigators or external devices to estimate the motion that occurred during the MR acquisition: the motion parameters are derived via a cost-function minimization strategy based on an image quality metric.
In this study, we developed and tested an autofocusing algorithm based on the GRAPPA parallel imaging technique; GRAPPA was used to predict one phase-encoding step in k-space based on the knowledge of the previous one, which was considered as motion free. The motion parameters were found by minimizing the difference between the predicted and real phase-encoding steps, using a cost function based on the MSE. Our results suggested that our algorithm can compensate very well for 2D translations; however, the algorithm struggled to estimate rotational motion both using the Fourier rotation theorem and shear transformations, despite the latter not requiring any regridding step. As the algorithm does not seem to be able to find a global minimum, it is possible that one of the major limitations of the current algorithm is the choice of the cost function. Future work might investigate the use of other image quality metrics present in the literature (e.g. GE), which are estimated in the image domain rather than the frequency domain.

6.2 Fat navigator accuracy

FatNav motion-parameter estimation relies on GRAPPA reconstruction of the highly accelerated navigator fat-volumes, which might be compromised by strong changes in the head position. Data from MPRAGE brain images have been used to find the motion corresponding to image quality boundaries and assess motion tolerance when FatNavs are used. Our results suggested that GRAPPA reconstruction will be compromised in the case of strong head position changes. Nevertheless, FatNavs were shown to be able to compensate for a large range of motion both in our smooth and rough motion scenarios. Future studies could explore the possibility of increasing FatNav robustness to strong motion artifacts by dynamically updating the GRAPPA weights during the scan, to avoid inconsistencies with the FatNavs during reconstruction. Although a definition of smooth and rough motion was given, future work might investigate a mathematical way to describe the difference between them. It is expected that the majority of routine MRI acquisitions are affected by smooth motion, where subjects move slowly throughout the acquisition; however, rough motion is expected to be performed by less compliant subjects during MRI scans. The clear artifact differences shown here between the two categories suggest that being able to distinguish between smooth and rough motion becomes important to be able to test estimation accuracy for different types of motion.

6.3 Navigator and markerless tracking

This study investigated the artifacts arising from different types of head motion in brain MR images and how well these artifacts can be compensated for by using retrospective correction based on two different motion-tracking techniques: FatNavs and Tracoline systems. Both methods could achieve good image quality in case of stepwise motion and slow changes in the head position (namely slow diagonal motion). When using FatNavs, our results suggested that it is beneficial to also incorporate a mask to exclude non-rigid parts of the neck to improve the image registration step – this is especially noticeable when larger motion occurs in the pitch-wise direction, as this emphasises the non-rigid movement. In the more extreme motion scenarios, the retrospectively corrected images often contained noticeable residual artifacts which we attributed to violations of the assumptions required for the retrospective correction used. Future work may investigate the theoretical limits that will lead to an artifact-free image after motion correction, elucidating to what extent residual artifacts can be alleviated by more advanced reconstruction techniques or whether real-time correction may be required when problematic motion scenarios are expected. In this study, we also showed that the use of a reference-based metric, such as the FSIM, gives a more reliable assessment of the image quality before and after motion correction compared to the non-reference-based metrics used. Future studies should examine if this is caused by the metrics' individual sensitivities to

the different manifestations of motion-related artifacts, and how these image quality metrics correlate with neuroradiologists' scores.

6.4 Combine motion correction with low acoustic noise

Three different configurations of a radial GRE-sequence were designed and tested using Pulseq, to reduce the acoustic noise produced by the rapid switching of gradient currents. Slower rising and falling of gradients, as well as optimization of spoiler gradient areas, resulted in 5 dB(A) reduction of acoustic noise using the Configuration 1 compared to the original GRE sequence. Configurations 2 and 3 allowed for a further noise reduction of around 4 dB(A) and 1 dB(A) respectively, by replacing the classical trapezoidal gradients' ramps with Gaussian waveforms. The acoustic measurements were performed using the Decibel X app on a mobile phone positioned outside the scanner room. To accurately measure the acoustic difference between sequences, further studies should use a calibrated microphone positioned at the entrance of the scanner bore, which is where the strongest acoustic noise is generated. Moreover, the same strategies could be tested to reduce the acoustic noise of sequences with sharper or more frequent variations between gradients (e.g. GRE train of an MPRAGE), which are expected to produce more acoustic noise compared to the sequence examined in this study.
The Configuration 1 was tested in-vivo with the subject performing slow back-and-forth head rotations. Prospective motion-correction was conducted using a markerless tracking device that sent the motion estimates to the scanner via the libXPACE framework, incorporated directly into Pulseq, to update gradients and RF pulses during the MR scan. The motion correction was tested successfully for one single slice acquisition, with the corrected images showing substantially higher image sharpness and level of detail. Further studies might investigate the robustness of sequence and motion correction methods in the case of multi-slice acquisition in infant subjects, taking advantage of the acoustic noise reduction especially when no sedation or anaesthesia are used.

Final remark

This thesis focused on different aspects of the motion correction problem in MRI, and proposed new approaches to help solving it. We started by presenting a new autofocusing motion correction method, to help compensate for the remaining motion artifacts expected when FatNav or the TCL retrospective motion correction are used. FatNav tracking accuracy and robustness was then investigated on simulated data, to find theoretical limits of the motion correction technique. Furthermore, FatNav and TCL markerless-tracking device were compared on real data against different types of motion, showing strength and limits of the two retrospective approaches. Finally, we showed how prospective motion correction using the TCL device could be easily exploit during pulse sequence design using Pulseq.

Bibliography

[1] L. G. Hanson and T. Groth, "Introduction to Magnetic Resonance Imaging Techniques," *TRANS.*, 2009.

[2] D. G. Nishimura, *Principles of Magnetic Resonance Imaging*. Stanford University, 1996.

[3] S. A. Huettel, A. W. Song, and G. McCarthy, *Functional Magnetic Resonance Imaging*. Sinauer Associates, 2004.

[4] L. E. Crooks, M. Arakawa, J. Hoenninger, B. McCarten, J. Watts, and L. Kaufman, "Magnetic resonance imaging: Effects of magnetic field strength.," *Radiology*, vol. 151, pp. 127–133, Apr. 1984.

[5] C. Lin, M. Bernstein, J. Huston, and S. Fain, "Measurements of T1 Relaxation times at 3.0T: Implications for clinical MRA," *ISMRM Abstract*, p. 1, 2001.

[6] G. J. Stanisz, E. E. Odrobina, J. Pun, M. Escaravage, S. J. Graham, M. J. Bronskill, and R. M. Henkelman, "T1, T2 relaxation and magnetization transfer in tissue at 3T," *Magnetic Resonance in Medicine*, vol. 54, pp. 507–512, Sept. 2005.

[7] S. Heiland, "From A as in Aliasing to Z as in Zipper: Artifacts in MRI," *Clinical Neuroradiology*, vol. 18, pp. 25–36, Mar. 2008.

[8] D. W. McRobbie, *MRI from Picture to Proton*. Cambridge, UK; New York: Cambridge University Press, 2006.

[9] M. A. Bernstein, K. F. King, and X. J. Zhou, *Handbook of MRI Pulse Sequences*. Elsevier, Sept. 2004.

[10] G. H. Glover and J. M. Pauly, "Projection Reconstruction Techniques for Reduction of Motion Effects in MRI," *Magnetic Resonance in Medicine*, vol. 28, pp. 275–289, Dec. 1992.

[11] M. Zaitsev, J. Maclaren, and M. Herbst, "Motion artifacts in MRI: A complex problem with many partial solutions: Motion Artifacts and Correction," *Journal of Magnetic Resonance Imaging*, vol. 42, pp. 887–901, Oct. 2015.

[12] K. P. Pruessmann, M. Weiger, M. B. Scheidegger, and P. Boesiger, "SENSE: Sensitivity encoding for fast MRI," *Magnetic Resonance in Medicine*, p. 11, 1999.

[13] A. Deshmane, V. Gulani, M. A. Griswold, and N. Seiberlich, "Parallel MR imaging," *Journal of Magnetic Resonance Imaging*, vol. 36, pp. 55–72, July 2012.

[14] D. K. Sodickson and W. J. Manning, "Simultaneous acquisition of spatial harmonics (SMASH): Fast imaging with radiofrequency coil arrays," *Magnetic Resonance in Medicine*, vol. 38, pp. 591–603, Oct. 1997.

[15] P. M. Jakob, M. A. Grisowld, R. R. Edelman, and D. K. Sodickson, "AUTO-SMASH: A self-calibrating technique for SMASH imaging," *Magma: Magnetic Resonance Materials in Physics, Biology, and Medicine*, vol. 7, pp. 42–54, Nov. 1998.

[16] M. A. Griswold, P. M. Jakob, R. M. Heidemann, M. Nittka, V. Jellus, J. Wang, B. Kiefer, and A. Haase, "Generalized autocalibrating partially parallel acquisitions (GRAPPA)," *Magnetic Resonance in Medicine*, vol. 47, pp. 1202–1210, June 2002.

[17] M. Blaimer, F. Breuer, M. Mueller, R. M. Heidemann, M. A. Griswold, and P. M. Jakob, "SMASH, SENSE, PILS, GRAPPA: How to Choose the Optimal Method," *Topics in Magnetic Resonance Imaging*, vol. 15, pp. 223–236, Aug. 2004.

[18] E. L. Hahn, "Spin Echoes," *Physical Review*, vol. 80, pp. 580–594, Nov. 1950.

[19] J. Hennig, A. Nauerth, and H. Friedburg, "RARE imaging: A fast imaging method for clinical MR," *Magnetic Resonance in Medicine*, vol. 3, pp. 823–833, Dec. 1986.

[20] M. Brant-Zawadzki, G. D. Gillan, and W. R. Nitz, "MP RAGE: A three-dimensional, T1-weighted, gradient-echo sequence–initial experience in the brain.," *Radiology*, vol. 182, pp. 769–775, Mar. 1992.

[21] F. Godenschweger, U. Kägebein, D. Stucht, U. Yarach, A. Sciarra, R. Yakupov, F. Lüsebrink, P. Schulze, and O. Speck, "Motion correction in MRI of the brain," *Physics in Medicine and Biology*, vol. 61, pp. R32–R56, Mar. 2016.

[22] L. Arena, H. T. Morehouse, and J. Safir, "MR imaging artifacts that simulate disease: How to recognize and eliminate them.," *RadioGraphics*, vol. 15, pp. 1373–1394, Nov. 1995.

[23] M. Bekiesińska-Figatowska, "Artifacts in Magnetic Resonance Imaging," *Polish Journal of Radiology*, vol. 80, pp. 93–106, 2015.

[24] R. C. Katz, L. Wilson, and N. Frazer, "Anxiety and its determinants in patients undergoing Magnetic Resonance Imaging," *Journal of Behavior Therapy and Experimental Psychiatry*, vol. 25, pp. 131–134, June 1994.

[25] E. Sartoretti, T. Sartoretti, M. Wyss, L. van Smoorenburg, B. Eichenberger, S. van der Duim, D. Cereghetti, C. A. Binkert, S. Sartoretti-Schefer, and A. Najafi, "Impact of Acoustic Noise Reduction on Patient Experience in Routine Clinical Magnetic Resonance Imaging," *Academic Radiology*, vol. 29, pp. 269–276, Feb. 2022.

[26] M. D. Tisdall, A. T. Hess, M. Reuter, E. M. Meintjes, B. Fischl, and A. J. W. van der Kouwe, "Volumetric navigators for prospective motion correction and selective

reacquisition in neuroanatomical MRI: Volumetric Navigators in Neuroanatomical MRI," *Magnetic Resonance in Medicine*, vol. 68, pp. 389–399, Aug. 2012.

[27] M. Bydder, D. Atkinson, D. J. Larkman, D. L. G. Hill, and J. V. Hajnal, "SMASH navigators," *Magnetic Resonance in Medicine*, vol. 49, no. 3, pp. 493–500, 2003.

[28] T. E. Wallace, O. Afacan, M. Waszak, T. Kober, and S. K. Warfield, "Head motion measurement and correction using FID navigators," *Magnetic Resonance in Medicine*, vol. 81, pp. 258–274, Jan. 2019.

[29] O. Afacan, T. E. Wallace, and S. K. Warfield, "Retrospective correction of head motion using measurements from an electromagnetic tracker," *Magnetic Resonance in Medicine*, vol. 83, pp. 427–437, Feb. 2020.

[30] N. White, C. Roddey, A. Shankaranarayanan, E. Han, D. Rettmann, J. Santos, J. Kuperman, and A. Dale, "PROMO: Real-time prospective motion correction in MRI using image-based tracking," *Magnetic Resonance in Medicine*, vol. 63, pp. 91–105, Jan. 2010.

[31] M. Zaitsev, C. Dold, G. Sakas, J. Hennig, and O. Speck, "Magnetic resonance imaging of freely moving objects: Prospective real-time motion correction using an external optical motion tracking system," *NeuroImage*, vol. 31, pp. 1038–1050, July 2006.

[32] G. Vaillant, C. Prieto, C. Kolbitsch, G. Penney, and T. Schaeffter, "Retrospective Rigid Motion Correction in k-Space for Segmented Radial MRI," *IEEE Transactions on Medical Imaging*, vol. 33, pp. 1–10, Jan. 2014.

[33] J. Fessler and B. Sutton, "Nonuniform fast fourier transforms using min-max interpolation," *IEEE Transactions on Signal Processing*, vol. 51, pp. 560–574, Feb. 2003.

[34] J. Maclaren, M. Herbst, O. Speck, and M. Zaitsev, "Prospective motion correction in brain imaging: A review: Prospective Motion Correction," *Magnetic Resonance in Medicine*, vol. 69, pp. 621–636, Mar. 2013.

[35] M. D. Tisdall, M. Reuter, A. Qureshi, R. L. Buckner, B. Fischl, and A. J. van der Kouwe, "Prospective motion correction with volumetric navigators (vNavs) reduces the bias and variance in brain morphometry induced by subject motion," *NeuroImage*, vol. 127, pp. 11–22, Feb. 2016.

[36] R. Frost, P. Wighton, F. I. Karahanoğlu, R. L. Robertson, P. E. Grant, B. Fischl, M. D. Tisdall, and A. van der Kouwe, "Markerless high-frequency prospective motion correction for neuroanatomical MRI," *Magnetic Resonance in Medicine*, vol. 82, pp. 126–144, July 2019.

[37] D. Atkinson, D. Hill, P. Stoyle, P. Summers, and S. Keevil, "Automatic correction of motion artifacts in magnetic resonance images using an entropy focus criterion," *IEEE Transactions on Medical Imaging*, vol. 16, no. 6, pp. 903–910, Dec./1997.

[38] W. Lin and H. K. Song, "Improved optimization strategies for autofocusing motion compensation in MRI via the analysis of image metric maps," *Magnetic Resonance Imaging*, vol. 24, pp. 751–760, July 2006.

[39] A. Loktyushin, H. Nickisch, R. Pohmann, and B. Schölkopf, "Blind retrospective motion correction of MR images: Blind Retrospective Motion Correction," *Magnetic Resonance in Medicine*, vol. 70, pp. 1608–1618, Dec. 2013.

[40] K. P. McGee, "Image Metric-Based Correction (Autocorrection)of Motion Effects: Analysis of Image Metrics," *Journal of Magnetic Resonance Imaging*, vol. 11, pp. 174–181, 2000.

[41] K. P. McGee, J. P. Felmlee, A. Manduca, S. J. Riederer, and R. L. Ehman, "Rapid autocorrection using prescan navigator echoes," *Magnetic Resonance in Medicine*, vol. 43, pp. 583–588, Apr. 2000.

[42] D. Atkinson and D. Hill, "Automatic Motion Correction Using Prior Knowledge," *ISMRM Abstract*, p. 1, 2001.

[43] D. Atkinson, D. L. G. Hill, P. N. R. Stoyle, P. E. Summers, S. Clare, R. Bowtell, and S. F. Keevil, "Automatic compensation of motion artifacts in MRI," *Magnetic Resonance in Medicine*, vol. 41, no. 1, pp. 163–170, 1999.

[44] D. Gallichan, J. P. Marques, and R. Gruetter, "Retrospective correction of involuntary microscopic head movement using highly accelerated fat image navigators (3D FatNavs) at 7T: 3D FatNavs for High-Resolution Retrospective Motion Correction," *Magnetic Resonance in Medicine*, vol. 75, pp. 1030–1039, Mar. 2016.

[45] F. Gretsch, H. Mattern, D. Gallichan, and O. Speck, "Fat navigators and Moiré phase tracking comparison for motion estimation and retrospective correction," *Magnetic Resonance in Medicine*, vol. 83, pp. 83–93, Jan. 2020.

[46] C. Glessgen, D. Gallichan, M. Moor, N. Hainc, and C. Federau, "Evaluation of 3D fat-navigator based retrospective motion correction in the clinical setting of patients with brain tumors," *Neuroradiology*, vol. 61, pp. 557–563, May 2019.

[47] J. M. Slipsager, S. L. Glimberg, L. Højgaard, R. R. Paulsen, P. Wighton, M. D. Tisdall, C. Jaimes, B. A. Gagoski, P. E. Grant, A. Kouwe, O. V. Olesen, and R. Frost, "Comparison of prospective and retrospective motion correction in 3D-encoded neuroanatomical MRI," *Magnetic Resonance in Medicine*, vol. 87, pp. 629–645, Feb. 2022.

[48] S. A. Winkler, F. Schmitt, H. Landes, J. de Bever, T. Wade, A. Alejski, and B. K. Rutt, "Gradient and shim technologies for ultra high field MRI," *NeuroImage*, vol. 168, pp. 59–70, Mar. 2018.

[49] J. Hutter, A. N. Price, L. Cordero-Grande, S. Malik, G. Ferrazzi, A. Gaspar, E. J. Hughes, D. Christiaens, L. McCabe, T. Schneider, M. A. Rutherford, and J. V.

Hajnal, "Quiet echo planar imaging for functional and diffusion MRI: Quiet Echo Planar Imaging," *Magnetic Resonance in Medicine*, vol. 79, pp. 1447–1459, Mar. 2018.

[50] T. Yamashiro, K. Morita, and K. Nakajima, "Evaluation of magnetic resonance imaging acoustic noise reduction technology by magnetic gradient waveform control," *Magnetic Resonance Imaging*, vol. 63, pp. 170–177, Nov. 2019.

[51] A. Copeland, E. Silver, R. Korja, S. J. Lehtola, H. Merisaari, E. Saukko, S. Sinisalo, J. Saunavaara, T. Lähdesmäki, R. Parkkola, S. Nolvi, L. Karlsson, H. Karlsson, and J. J. Tuulari, "Infant and Child MRI: A Review of Scanning Procedures," *Frontiers in Neuroscience*, vol. 15, p. 666020, July 2021.

[52] O. J. Arthurs, A. Edwards, T. Austin, M. J. Graves, and D. J. Lomas, "The challenges of neonatal magnetic resonance imaging," *Pediatric Radiology*, vol. 42, pp. 1183–1194, Oct. 2012.

[53] M. J. McJury, "Acoustic Noise and Magnetic Resonance Imaging : A Narrative/Descriptive Review," *Journal of Magnetic Resonance Imaging*, p. jmri.27525, Feb. 2021.

[54] W. A. Edelstein, R. A. Hedeen, R. P. Mallozzi, S.-A. El-Hamamsy, R. A. Ackermann, and T. J. Havens, "Making MRI Quieter," *Magnetic Resonance Imaging*, vol. 20, pp. 155–163, Feb. 2002.

[55] D. L. Price, J. P. De Wilde, A. M. Papadaki, J. S. Curran, and R. I. Kitney, "Investigation of acoustic noise on 15 MRI scanners from 0.2 T to 3 T," *Journal of Magnetic Resonance Imaging*, vol. 13, pp. 288–293, Feb. 2001.

[56] X. Zhao, H. Lee, H. K. Song, C.-C. Cheng, and F. W. Wehrli, "Impact of gradient imperfections on bone water quantification with UTE MRI," *Magnetic Resonance in Medicine*, vol. 84, pp. 2034–2047, Oct. 2020.

[57] D. M. Grodzki, P. M. Jakob, and B. Heismann, "Ultrashort echo time imaging using pointwise encoding time reduction with radial acquisition (PETRA)," *Magnetic Resonance in Medicine*, vol. 67, pp. 510–518, Feb. 2012.

[58] N. Aida, T. Niwa, Y. Fujii, K. Nozawa, M. Enokizono, K. Murata, and T. Obata, "Quiet T1-Weighted Pointwise Encoding Time Reduction with Radial Acquisition for Assessing Myelination in the Pediatric Brain," *American Journal of Neuroradiology*, vol. 37, pp. 1528–1534, Aug. 2016.

[59] D. P. Madio and I. J. Lowe, "Ultra-fast imaging using low flip angles and fids," *Magnetic Resonance in Medicine*, vol. 34, pp. 525–529, Oct. 1995.

[60] E. Ljungberg, N. L. Damestani, T. C. Wood, D. J. Lythgoe, F. Zelaya, S. C. Williams, A. B. Solana, G. J. Barker, and F. Wiesinger, "Silent zero TE MR neuroimaging: Current state-of-the-art and future directions," *Progress in Nuclear Magnetic Resonance Spectroscopy*, vol. 123, pp. 73–93, Apr. 2021.

[61] F. Hennel, F. Girard, and T. Loenneker, "Silent MRI with soft gradient pulses," *Magnetic Resonance in Medicine*, vol. 42, pp. 6–10, July 1999.

[62] L. Cordero-Grande, G. Ferrazzi, R. P. A. G. Teixeira, J. O'Muircheartaigh, A. N. Price, and J. V. Hajnal, "Motion-corrected MRI with DISORDER: Distributed and incoherent sample orders for reconstruction deblurring using encoding redundancy," *Magnetic Resonance in Medicine*, vol. 84, pp. 713–726, Aug. 2020.

[63] M. W. Haskell, S. F. Cauley, B. Bilgic, J. Hossbach, D. N. Splitthoff, J. Pfeuffer, K. Setsompop, and L. L. Wald, "Network Accelerated Motion Estimation and Reduction (NAMER): Convolutional neural network guided retrospective motion correction using a separable motion model," *Magnetic Resonance in Medicine*, vol. 82, pp. 1452–1461, Oct. 2019.

[64] D. Polak, D. N. Splitthoff, B. Clifford, W.-C. Lo, S. Y. Huang, J. Conklin, L. L. Wald, K. Setsompop, and S. Cauley, "Scout accelerated motion estimation and reduction (SAMER)," *Magnetic Resonance in Medicine*, vol. 87, pp. 163–178, Jan. 2022.

[65] D. S. Smith, S. Sengupta, S. A. Smith, and E. Brian Welch, "Trajectory optimized NUFFT: Faster non-Cartesian MRI reconstruction through prior knowledge and parallel architectures," *Magnetic Resonance in Medicine*, vol. 81, pp. 2064–2071, Mar. 2019.

[66] Z. Yang and M. Jacob, "Mean square optimal NUFFT approximation for efficient non-Cartesian MRI reconstruction," *Journal of magnetic resonance (San Diego, Calif. : 1997)*, vol. 0, pp. 126–135, May 2014.

[67] M. L. Wood, M. J. Shivji, and P. L. Stanchev, "Planar-motion correction with use of k-space data acquired in fourier MR imaging," *Journal of Magnetic Resonance Imaging*, vol. 5, pp. 57–64, Jan. 1995.

[68] T. Toffoli and J. Quick, "Three-Dimensional Rotations by Three Shears," *Graphical Models and Image Processing*, vol. 59, pp. 89–95, Mar. 1997.

[69] W. F. Eddyy, M. Fitzgerald, and D. C. Noll, "Improved image registration by using fourier interpolation," *Magnetic Resonance in Medicine*, vol. 36, pp. 923–931, Dec. 1996.

[70] "retroMoCoBox - https://github.com/dgallichan/retroMoCoBox."

[71] D. L. Collins, C. J. Holmes, T. M. Peters, and A. C. Evans, "Automatic 3-D model-based neuroanatomical segmentation," *Human Brain Mapping*, vol. 3, no. 3, pp. 190–208, 1995.

[72] "SPIRiT V0.3." https://people.eecs.berkeley.edu/~mlustig/Software.html.

[73] K. Perlin, "An image synthesizer," *ACM SIGGRAPH Computer Graphics*, vol. 19, pp. 287–296, July 1985.

[74] "Understanding Perlin Noise." https://adrianb.io/2014/08/09/perlinnoise.html.

[75] N. Seiberlich, F. A. Breuer, M. Blaimer, K. Barkauskas, P. M. Jakob, and

M. A. Griswold, "Non-Cartesian data reconstruction using GRAPPA operator gridding (GROG)," *Magnetic Resonance in Medicine*, vol. 58, pp. 1257–1265, Dec. 2007.

[76] D. Garcia, "Robust smoothing of gridded data in one and higher dimensions with missing values," *Computational Statistics & Data Analysis*, vol. 54, pp. 1167–1178, Apr. 2010.

[77] D. Garcia, "A fast all-in-one method for automated post-processing of PIV data," *Experiments in Fluids*, vol. 50, pp. 1247–1259, May 2011.

[78] "SPM - Statistical Parametric Mapping," 2019.

[79] K. Krippendorff, *Content Analysis. An Introduction to Its Methodology*. California, CA: Sage Publications, third ed., 2013.

[80] J. Eggink, "Krippendorff's Alpha," 2020.

[81] D. Bohning, "Multinomial logistic regression algorithm," *Annals of the Institute of Statistical Mathematics*, vol. 44, pp. 197–200, Mar. 1992.

[82] S. Watanabe, "A Widely Applicable Bayesian Information Criterion," *Journal of Machine Learning Research*, vol. 14, pp. 867–897, 2013.

[83] J. D. Power, K. A. Barnes, A. Z. Snyder, B. L. Schlaggar, and S. E. Petersen, "Spurious but systematic correlations in functional connectivity MRI networks arise from subject motion," p. 28, 2013.

[84] J. B. Andre, B. W. Bresnahan, M. Mossa-Basha, M. N. Hoff, C. P. Smith, Y. Anzai, and W. A. Cohen, "Toward Quantifying the Prevalence, Severity, and Cost Associated With Patient Motion During Clinical MR Examinations," *Journal of the American College of Radiology*, vol. 12, pp. 689–695, July 2015.

[85] J. M. Slipsager, S. L. Glimberg, J. Søgaard, R. R. Paulsen, H. H. Johannesen, P. C. Martens, A. Seth, L. Marner, O. M. Henriksen, O. V. Olesen, and L. Højgaard, "Quantifying the Financial Savings of Motion Correction in Brain MRI: A Model-Based Estimate of the Costs Arising From Patient Head Motion and Potential Savings From Implementation of Motion Correction," *Journal of Magnetic Resonance Imaging*, vol. 52, pp. 731–738, Sept. 2020.

[86] J. W. Peirce, "PsychoPy—Psychophysics software in Python," *Journal of Neuroscience Methods*, vol. 162, 2007.

[87] Lin Zhang, Lei Zhang, Xuanqin Mou, and D. Zhang, "FSIM: A Feature Similarity Index for Image Quality Assessment," *IEEE Transactions on Image Processing*, vol. 20, pp. 2378–2386, Aug. 2011.

[88] A. Mason, J. Rioux, S. E. Clarke, A. Costa, M. Schmidt, V. Keough, T. Huynh, and S. Beyea, "Comparison of Objective Image Quality Metrics to Expert Radiologists' Scoring of Diagnostic Quality of MR Images," *IEEE Transactions on Medical Imaging*, vol. 39, pp. 1064–1072, Apr. 2020.

[89] Z. Wang, A. Bovik, H. Sheikh, and E. Simoncelli, "Image Quality Assessment: From

Error Visibility to Structural Similarity," *IEEE Transactions on Image Processing*, vol. 13, pp. 600–612, Apr. 2004.

[90] W. Lin, G. A. Ladinsky, F. W. Wehrli, and H. K. Song, "Image metric-based correction (autofocusing) of motion artifacts in high-resolution trabecular bone imaging," *Journal of Magnetic Resonance Imaging*, vol. 26, pp. 191–197, July 2007.

[91] P.-L. Bazin, H. E. Nijsse, W. van der Zwaag, D. Gallichan, A. Alkemade, F. M. Vos, B. U. Forstmann, and M. W. Caan, "Sharpness in motion corrected quantitative imaging at 7T," *NeuroImage*, vol. 222, p. 117227, Nov. 2020.

[92] N. S. White, A. Shankaranarayanan, E. T. Han, A. Gaddipati, C. Roddey, and A. M. Dale, "Prospective Motion Correction Using Nonlinear Predictive Filtering,"

[93] S. Thesen, O. Heid, E. Mueller, and L. R. Schad, "Prospective acquisition correction for head motion with image-based tracking for real-time fMRI," *Magnetic Resonance in Medicine*, vol. 44, pp. 457–465, Sept. 2000.

[94] M. Jenkinson, P. Bannister, M. Brady, and S. Smith, "Improved Optimization for the Robust and Accurate Linear Registration and Motion Correction of Brain Images," *NeuroImage*, vol. 17, pp. 825–841, Oct. 2002.

[95] M. Jenkinson and S. Smith, "A global optimisation method for robust affine registration of brain images," *Medical Image Analysis*, vol. 5, pp. 143–156, June 2001.

[96] S. M. Smith, "Fast robust automated brain extraction," *HumanBrainMapping*, vol. 17, pp. 143–155, 2002.

[97] M. Jenkinson, M. Pechaud, and S. Smith, "BET2 - MR-Based Estimation of Brain, Skull and Scalp Surfaces,"

[98] S. M. Smith, M. Jenkinson, M. W. Woolrich, C. F. Beckmann, T. E. Behrens, H. Johansen-Berg, P. R. Bannister, M. De Luca, I. Drobnjak, D. E. Flitney, R. K. Niazy, J. Saunders, J. Vickers, Y. Zhang, N. De Stefano, J. M. Brady, and P. M. Matthews, "Advances in functional and structural MR image analysis and implementation as FSL," *NeuroImage*, vol. 23, pp. S208–S219, Jan. 2004.

[99] P. A. Yushkevich, J. Piven, H. C. Hazlett, R. G. Smith, S. Ho, J. C. Gee, and G. Gerig, "User-guided 3D active contour segmentation of anatomical structures: Significantly improved efficiency and reliability," *NeuroImage*, vol. 31, pp. 1116–1128, July 2006.

[100] S. Rusinkiewicz and M. Levoy, "Efficient variants of the ICP algorithm," in *Proceedings Third International Conference on 3-D Digital Imaging and Modeling*, (Quebec City, Que., Canada), pp. 145–152, IEEE Comput. Soc, 2001.

[101] D. C. Dean, H. Dirks, J. O'Muircheartaigh, L. Walker, B. A. Jerskey, K. Lehman, M. Han, N. Waskiewicz, and S. C. L. Deoni, "Pediatric neuroimaging using magnetic resonance imaging during non-sedated sleep," *Pediatric Radiology*, vol. 44, pp. 64–72, Jan. 2014.

[102] K. J. Layton, S. Kroboth, F. Jia, S. Littin, H. Yu, J. Leupold, J.-F. Nielsen, T. Stöcker, and M. Zaitsev, "Pulseq: A rapid and hardware-independent pulse sequence prototyping framework: Rapid Hardware-Independent Pulse Sequence Prototyping," *Magnetic Resonance in Medicine*, vol. 77, pp. 1544–1552, Apr. 2017.

[103] M. Zaitsev and M. Woletz, "Real-time prospective motion correction of arbitrary MR pulse sequences with XPACE-Pulseq.," *ISMRM*, 2021.

[104] K. Ravi, S. Geethanath, and J. Vaughan, "PyPulseq: A Python Package for MRI Pulse Sequence Design," *Journal of Open Source Software*, vol. 4, p. 1725, Oct. 2019.

[105] F. Di Giuliano, S. Minosse, E. Picchi, V. Ferrazzoli, V. Da Ros, M. Muto, C. A. Pistolese, F. Garaci, and R. Floris, "Qualitative and quantitative analysis of 3D T1 Silent imaging," *La radiologia medica*, vol. 126, pp. 1207–1215, Sept. 2021.

[106] J. M. Slipsager, A. H. Ellegaard, S. L. Glimberg, R. R. Paulsen, M. D. Tisdall, P. Wighton, A. van der Kouwe, L. Marner, O. M. Henriksen, I. Law, and O. V. Olesen, "Markerless motion tracking and correction for PET, MRI, and simultaneous PET/MRI," *PLOS ONE*, vol. 14, p. e0215524, Apr. 2019.